Title
Resolving Soft Material Crystallinity through Scanning Transmission Electron Nanodiffraction

Author
Panova, Ouliana

Publication Date
2018

Peer reviewed|Thesis/dissertation

Resolving Soft Material Crystallinity through Scanning Transmission Electron Nanodiffraction

by

Ouliana Panova

A dissertation submitted in partial satisfaction of the
requirements for the degree of
Doctor of Philosophy

in

Engineering – Materials Science Engineering

in the

Graduate Division

of the

University of California, Berkeley

Committee in charge:

Professor Andrew Minor, Chair
Professor Mark Asta
Professor Nitash Balsara

Fall 2018

Resolving Soft Material Crystallinity through Scanning Transmission Electron Nanodiffraction

Abstract

Resolving Soft Material Crystallinity through Scanning Transmission Electron Nanodiffraction

by

Ouliana Panova

Doctor of Philosophy in Engineering – Materials Science Engineering

University of California, Berkeley

Professor Andrew Minor, Chair

A method for imaging the semi-crystalline structure of organic, electrically conducting molecular thin films using scanning nanodiffraction transmission electron microscopy (4D-STEM) is developed, with a maximum achieved resolution of 5-10 nm, depending on the material analyzed. The changes in local nanocrystalline structure of the polymer thin films under study - regioregular Poly(3-hexyl-thiophene-2,5-diyl), the small molecule 7,7'-(4,4 - bis(2 - ethylhexyl) - 4H - silolo[3,2-b:4, 5-*b*'] dithiophene - 2,6 - diyl) bis(6 - fluoro - 4 - (5'- hexyl[2,2'-bithiophen] - 5 - yl)benzo[*c*][1,2,5] - thiadiazole), abbreviated as p-DTS(FBTTh$_2$)$_2$ or T1, and Poly[2,5-bis(3-tetradecylthiophen-2-yl)thieno[3,2-*b*]thiophene], abbreviated as PBTTT - with processing conditions, such as solvent addition and annealing, are characterized and visualized. The methods presented show spatially resolved features such as overlapping grains and nematic liquid crystal character that have not been directly imaged before, and help remove ambiguities in X-ray and other techniques that have been thus far used to characterize these materials.

The method is first applied to polyethylene and P3HT samples to demonstrate the viability of the electron transmission technique on soft materials and determine its limitations. A resolution of 5 nm is achieved on P3HT. The method is subsequently used to visualize the changes in crystal structure of T1 when treated with 1,8-diiodooctane (DIO), and then on PBTTT to characterize morphological changes upon annealing. It is found that for T1, while the untreated samples exhibited a liquid-crystal-like structure with crystalline orientations varying smoothly over all possible rotations, the addition of a co-solvent induces partial segmentation of the structure characterized by the emergence of sharp grain boundaries and overlapping domains with unrelated orientations. In the case of PBTTT, the crystalline character of the nematic liquid crystal phase increases upon annealing. These results demonstrate how scanning electron nanobeam diffraction can provide a new level of insight into the structure of functional organic solids, and show how structure-property relationships can be visualized in organic systems using nanoscale electron microscopy techniques previously only available for hard materials such as metals and ceramics.

To my grandfather, Nikolai Nikolaievich Vasiliev, who inspired me to go into science

"Дедушка, расскажи мне про плазму"

Contents

Contents **ii**

List of Figures **iv**

1 Introduction **1**
1.1 Electrically Conductive Polymers 1
1.2 Polymer Crystallinity 5
1.3 Characterization Techniques for Polymers and Soft Materials 8

2 Benchmarking the technique on P3HT:PS semicrystalline thin films **12**
2.1 Motivation and overview 12
2.2 Experimental Methods 12
2.3 Analysis algorithm 15
2.4 Conclusion 21

3 Effect of DIO on the structure of T1 small molecule thin films **22**
3.1 Motivation and Overview 22
3.2 Experimental Methods 23
3.3 Results 25
3.4 Conclusion 31

4 Effect of Annealing on PBTTT liquid crystal structure **32**
4.1 Motivation 32
4.2 Methods 33
4.3 Results 35
4.4 Conclusion 39

5 Conclusion **40**

Bibliography **41**

A Code **53**
A.1 Virtual Dark Field 54

A.2 Realignment of diffraction pattern centers 54
A.3 Subtraction of the amorphous background 55
A.4 Line trace plotting 58
A.5 Tiling real space with diffraction patterns 59
A.6 Extracting peak orientations from the diffraction patterns 60
A.7 Plotting of the main peak - orientation maps 65
A.8 Reformatting peak data, converting to polar coordinates 68
A.9 Tracing the line flows of the lattice 69

List of Figures

1.1 Comparison of the efficiencies of photovoltaic devices from 1976 to 2016. The organic photovoltaics (filled red markers) came rather late to the party (2001), but their efficiency has been steadily increasing. This plot is courtesy of the National Renewable Energy Laboratory, Golden, CO. 3

1.2 Polarons and solitons[49]. **A**) Illustration of the energies involved in a molecular ionization process. $E_{\mathrm{IP-v}}$ is the vertical ionization energy, E_{rel}, the relaxation energy gained in the ionized state, E_{dis}, the distortion energy to be paid in the ground state in order that the molecule adopts the equilibrium geometry of the ionized state, and $E_{\mathrm{IP-d}}$, the ionization energy of the distorted molecule. **B**) Evolution of the polypyrrole band structure upon doping: (a) low doping level, polaron formation; (b) moderate doping level, bipolaron formation; (c) high (33 mol %) doping level, formation of bipolaron bands. **C**) Schematic illustration of the geometric structure of a neutral soliton on a trans-polyacetylene chain. . . . 5

1.3 Schematic diagram of the crystallinity of a polymer[54]. **a** shows a semicrystalline configurations, where polymer chains fold on themselves and align to form areas of high order, connected by an amorphous phase; **b** shows smaller crystalline domains and **c** demonstrates a completely amorphous configuration. 6

1.4 Schematic of P3HT stacking.[62] **a** Diagram of the crystalline arrangement of the polymer, with crystallites in black and amorphous regions in gray. **b** Molecular view of the stacking of the P3HT chains in the π-π direction (green arrows). Some side chains have been omitted for clarity. 7

1.5 Overview of published results on characterization techniques applied to crystalline polymers. a) XRD spectrum of polyethylene tetraphtalate[85], with a highly crystalline sample (top) used for a reference template and a more typical, less crystalline specimen (bottom) showing less resolved peaks. b) Nanodiffraction composite of a polyethylene single crystal[86]. Many faint diffraction patterns from varied locations within the crystal were averaged to produce the final image. c) Scanning tunneling micrograph of poly(3,3"-didodecylquaterthiophene)[87], showing high resolution of the ordered chains. Field of view is 13 nm x 19 nm. d) Spatially resolved boundary map between polyethylene and nylon using scanning EELS spectra[88]. e) Cryo-EM tomography of P3HT[89], showing lamellar chain arrangement. f)HRTEM of a small molecule with Fourier analysis used to extract chain orientations and map them (right)[90]. g)AFM of P3HT films[91], showing dispersed terraces of crystalline domains. 10

2.1 The 4DSTEM experiment. (a) Convergent beam rasters across the sample (i,j) and captures a full diffraction pattern (K_x,K_y) for each probe location. (b) Molecular schematic of the P3HT monomer structure. (c) The data takes the form of a 4-dimensional n × m set where each pixel in real space (i, j) corresponds to a full diffraction pattern (K_x, K_y). 14

2.2 Schematic illustration of the algorithm developed. (a) Diagram of the effect of the beam sway as it scans the sample; the colored surface is a parabolic fit to calculated beam shifts for the P3HT sample dataset used in this study. (b) Diagram of a typical diffraction pattern obtained in 4D-STEM, with diffraction spots superimposed on a background scattered halo. Inset shows a DP from a gathered dataset. (c) Diffraction pattern after processing, with the background halo removed and the diffraction spots clearly featured. A virtual annular aperture used for virtual dark field calculations is outlined in white. Inset shows the DP from (b) after application of the algorithm. 15

2.3 Raw and minimally processed images for P3HT/PS (200 kV). (a) ADF-STEM image with oval clusters of P3HT shown by white arrows. (b) Aggregate at higher magnification displaying structure within. (c) EDS map with sulfur signal in yellow. (d) Preliminary virtual dark field image reconstructed using the entirety of the DP field of view. 17

2.4 Algorithm applied to P3HT:PS sample at 300 kV. (a) ADF-STEM image of P3HT sample, with the 4D-STEM-rastered region outlined in a white dashed square. Two VDFs of the 4DSTEM dataset (step size of 40 nm) are shown. (b) VDF image constructed from signal summed over the whole field of view of the detector. (c) VDF image constructed from halo-subtracted signal within a thin virtual annular aperture that only includes locations where diffraction peaks occur. 19

2.5 Algorithm applied to P3HT/PS sample at 200 kV. (a) Normalized VDF showing the relative intensity of the Bragg reflections, obtained from a processed dataset where the background scattered halo has been removed. (b) Map of a normalized local degree of crystallinity, as defined here by the ratio of the Bragg diffraction signal to the extracted amorphous scattered signal. Yellow spots indicate high degree of crystallinity. (c) Bragg diffraction angle map of the rastered region, with the angle map overlaid onto the ADF image. 20

3.1 Illustration of the evolution of the autocorrelation map as an artificially constructed microstructure evolves from sharp, distinct grains to a smoothly varying orientation field. The transition is done by applying a Gaussian filter with standard deviation σ; dataset size was chosen to match the size of the data gathered for T1 and T1+DIO. 26

3.2 Schematic of the 4D-STEM technique (a) and molecular structure of the T1 molecule (b). As the convergent beam rasters over the area of interest, a full diffraction pattern is acquired for each real space probe location (x, y), with a step size large enough to prevent the beam from damaging the yet unsampled neighboring positions. The molecules stack along their π-π bonds as illustrated in (c). The data structure resulting from the technique is shown in (d), with examples of diffraction patterns obtained from T1 + DIO. The π-π stacking characteristic distance of the molecules is indexed on one of the DPs. 27

3.3 Comparison of morphology between samples drop cast with DIO (a, c, e) and without DIO (b, d, f). (a,b) Background HAADF. Dotted lines show area of 4D-STEM scan. A virtual dark field of the scattered amorphous signal reconstructed from the DPs is overlaid onto the HAADF. The angle maps (c, d) show the orientation of the brightest reflection found on the DP at that location. Black arrows in c) indicate disclination discontinuities. Flow maps (e, f) show the continuity of lattice orientations in space. Scale bar is 200 nm. 29

3.4 Autocorrelation results in a) show the spatial and angular relationship between a probe location at r with an orientation θ to one Δr nanometers away with an orientation $\theta + \Delta\theta$. Overlaid slices for both samples are shown in b) for three values for Δr, clearly demonstrating the increasing divergence between the two as Δr increases. 30

4.1 Visualization of dataset A1 at different scales. a) Schematic of the 4DSTEM acquisition technique, showing the dark field reconstruction. The area outlined on the dark field view is shown in b), where real space is tiled with post-processed diffraction patterns. Swatches show areas of relatively constant orientation (A), places where the amorphous halo overtakes the signal and it becomes difficult to differentiate between diffraction from the thick carbon edge and diffraction from the thin film (B), and areas of smooth, gradual rotation (C). The extent of a full diffraction pattern is delineated in the upper left corner of each swatch for reference. 34

4.2 Virtual dark field reconstruction (a), angle orientation map (b), and like orientation visualization (c) of the as cast sample C1. Scale bar is 300 nm. 35
4.3 Orientation maps of the A1, annealed PBTTT sample. (a) Dark field reconstruction. (b) Angle orientation map. (c) Orientation line plotted for each DP, with slope matched to the angle of the diffraction spots. Scale bar is 300 nm. 36
4.4 Virtual dark field reconstruction (a) and line flow visualization (b) of the annealed sample C11. Scale bar is 300 nm. 37
4.5 Orientation maps of the A1, annealed PBTTT sample. a) The dark field reconstruction shows variation in thickness of the lacey carbon; the film and the break therein are also visible. b) Orientation map colored according to most prominent lattice orientation. c) and d) Line flow visualizations. Scale bar is 300 nm. . . . 38

Acknowledgments

I would like to extend my most sincere thanks to Andrew Minor, who has been incredibly patient with me and made me discover my love for microscopy and characterization. Thank you to Karen, who is the most patient and caring person I have ever met, for leading me through the microscope sessions and supporting me all the way. I also wish to thank Colin Ophus for his invaluable help and expertise, and Chris Takacs for the providing such interesting projects to work on. Finally, I would like to thank everyone at NCEM for making it such a wonderful place to work.

Primary funding for the work was provided by the Electron Microscopy of Soft Matter Program from the Office of Science, Office of Basic Energy Sciences, Materials Sciences and Engineering Division of the U.S. Department of Energy under Contract No. DE-AC02-05CH11231. Work at the Molecular Foundry was supported by the Office of Science, Office of Basic Energy Sciences, of the U.S. Department of Energy under Contract No. DE-AC02-05CH11231. We also thank Dr. Hongping Yan for providing materials and Dr. Mike Toney for useful discussions.

Chapter 1

Introduction

1.1 Electrically Conductive Polymers

Applicability and Relevance

Ever since the initial discovery of polyacetylene's dramatic increase in electrical conductivity when reacted with iodine in 1977[1, 2], electrically conductive polymers have been postulated as an advantageous replacement for metals and semiconductors in practically any field where electrons need to go from one place to another[3]. Initially, the transport mechanism was not well understood, but to be able to bring the unique characteristics of these materials to the field of electronics was an exciting premise that spurred large research efforts. Polymers are – in addition to many other favorable properties – transparent[4], relatively cheap and easy to manufacture, lightweight, flexible[5, 6], and non-toxic. Furthermore, while they can exhibit high electronic conductivities on their own, they can also be doped with a variety of chemical additives in order to effectively become an equivalent to n or p type semiconductors. This meant that wherever there was silicon, there could be plastic instead – a revolutionizing idea indeed.

While it has quickly become apparent that their faster degradation[7, 8, 9] and lower efficiency[10] have yet to put them in direct competition with silicon in the large-scale photovoltaic industry (ref Fig.1.1), the field has successfully branched into myriad other applications where portability and ease of integration with other materials are the prevailing criteria. In addition to the already prominent and quickly growing OLED display industry[11, 12], conductive polymers are now being developed for use in wearable textiles[13, 14], corrosion-resistant surface treatments[15], organic field-effect transistors[16, 17, 18], capacitors[19], biomedical[20, 21, 22], environmental[23, 24], and mechanical[16, 25] sensors, antistatic coatings[26, 27], electroluminescent and optoelectronic[28, 29] devices, and many more[30].

Even though somewhat efficiency-challenged, polymers and organics have assets that rigid, opaque, brittle silicon can only dream about. Thanks to their transparency to the visible spectrum and the general malleability of their absorption bands, they can be seamlessly

integrated into window panes while retaining up to 90% of their visible transmittance[31] while eliminating the need for financially and environmentally costly energy distribution setups by generating energy directly where it is needed. The biosensor field has also been making great use of their unique properties; combined with specific functionalized additives such as graphene or metal nanoparticles, conducting polymers can detect a wide variety of biologically relevant chemical species, from glucose to neurotransmitters to nucleic acids[32, 33]. Their electrical conductivity is particularly useful in drug delivery systems and surgical augmentation, as they can release entrapped molecules[34] or exert a mechanical force[35] through the application of current – thus acting as scaffolding for specialized cell growth or as self-coiling and expanding vascular stents[36]. Their ability to conduct electrons away from surfaces makes them a good contender for transparent coatings, where accumulation of static charge could damage sensitive electronics or lead to dust and particle build-up over time[26]. The metallurgy industry has also been exploiting the polymers' stability in acidic and corrosive environments, while tailoring their electronic properties to allow them to form self-healing passivation layers to protect highly oxidizable metals such as steel[37, 38]. Textile makers saw them as an opportunity to weave tactile sensors and temperature controls directly into clothing[39], as their flexibility and biocompatibility would allow them to be integrated into the fibers of the fabrics. Conducting polymers have been at the core of advancements in the sensory mechanisms of artificial skin[40, 41], and have been postulated as possible artificial emulators of muscle tissue[42, 43].

This plethora of applications is in part spurred by better, more versatile and precise synthesis methods for polymers, which allows exquisite control over molecular composition and configuration. Since there is virtually no limit to how long or complicated a polymer can be, the landscape of molecular weight, atomic composition, side chain geometry, steric configuration, monomer combination, etc. has only been partly explored. The main feature of a conducting polymer is the conjugated backbone of alternating carbon single and double bonds; the length of the side chains or the nature of the end radicals affect its conducting character only inasmuch as they prevent charge transfer from one chain to another. New configurations are being synthesized and characterized at a rapid pace, creating new and exciting pathways for exploration and improvement.

While it remains true that some of the polymer components used in organic photovoltaics are much more expensive per weight than the usual silicon, the quantity needed to produce the same effective area is considerably smaller; in some cases, the manufacturing processes also lend themselves to large-scale, continuous mass-production, with particular interest in direct and 3D [44, 45] printing and rolling techniques[46, 47]. Even if the arid expanses of Arizona are in no danger of being tiled over for now, such ease of manufacture could potentially lead OPVs to become a viable addition to everyday energy generation in urbanized areas.

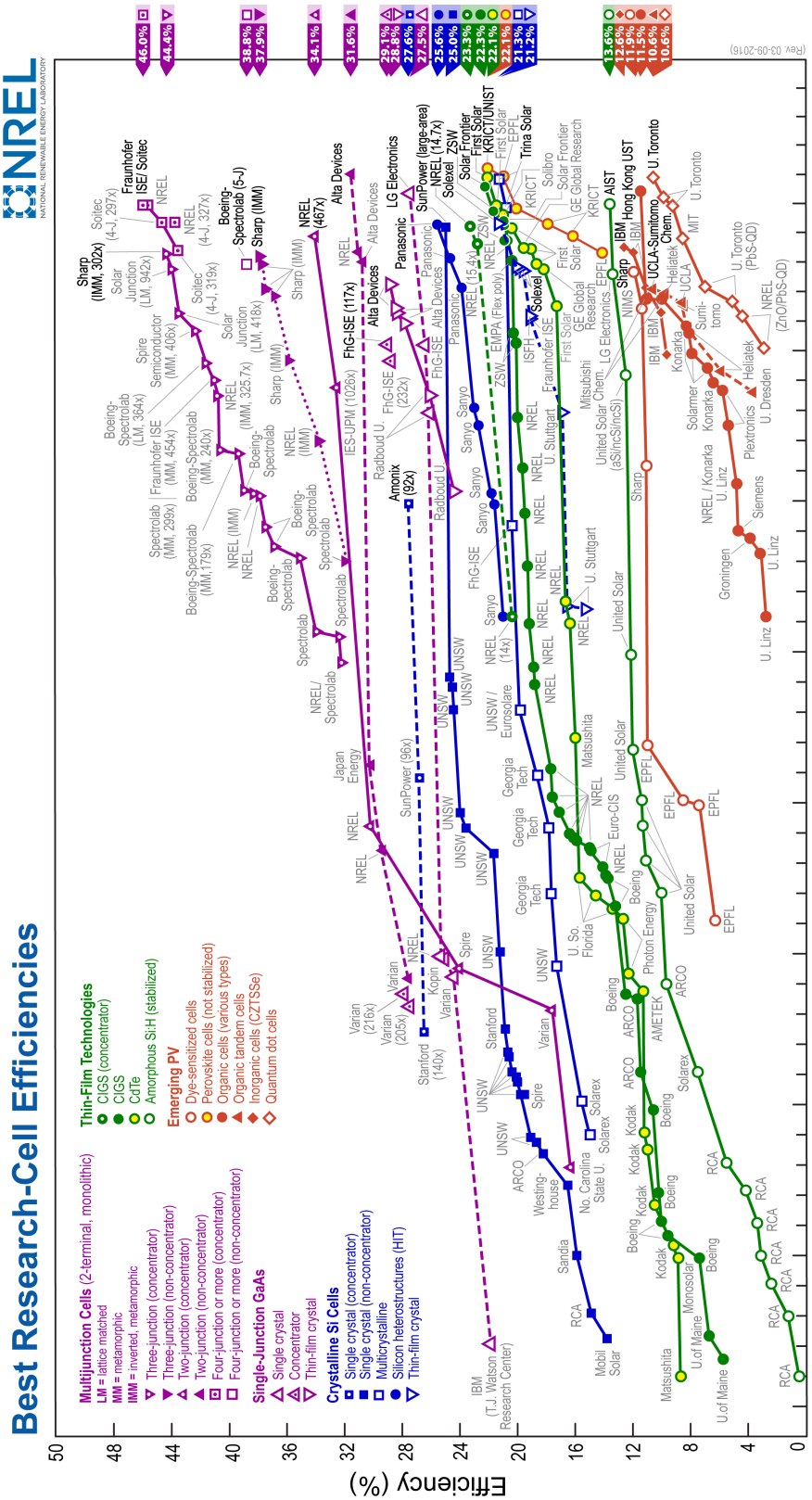

Figure 1.1: Comparison of the efficiencies of photovoltaic devices from 1976 to 2016. The organic photovoltaics (filled red markers) came rather late to the party (2001), but their efficiency has been steadily increasing. This plot is courtesy of the National Renewable Energy Laboratory, Golden, CO.

Electronic Conduction Mechanisms

Because polymeric structures are usually closed-shelled covalent structures, they do not often have extra electrons available for charge conduction. This is partially why they are generally quite inert and chemically stable. The discovery of the conducting properties of the inorganic polymer polysulfur nitride $(SN)_x$ showed that backbone structures with delocalized charge can, and do, exist[48]. The secret to polymeric electron conduction resides in the conjugation of their backbones[21]: an alternating sequence of carbon single and double bonds. Both types have σ bonding, which holds the molecule together; the double-bonds, however, also have π bonding, whose electrons are weaker and can become delocalized over the length of the chain. These π electrons are not as strongly attached to the structure and can either move somewhat freely along the chain – giving the polymer a metallic character – or react with doping species to form charge carriers. Indeed, while the principal mechanism of the delocalized π electrons moving along the backbone leads to a certain amount of conductivity, it is really the combination of a conjugated polymer to an oxidizing or reacting agent that generate the charge carriers necessary for competitive values of conductance. The addition of an oxidizing agent leads to what is – somewhat erroneously – called "p-doping", and, conversely, the addition of a reducing agent leads to "n-doping", the appellation referring to the charge of the conducting element.

The presence of a local charge on the backbone necessarily influences the conformation of its surroundings, especially if the molecule is particularly flexible or polar. The molecule that carries the charge can deform around the charge in order to fall into a more favorable, lower energy configuration (ref Fig.1.2); this coupling of a charge with a local physical distortion of the molecule is called a "polaron" and is what *really* carries current along the chain. In a lot of cases, it is more energetically favorable to carry two coupled polarons within one chain – such pairs are appropriately called "bipolarons". The distortion can come in the shape of a change in the order of alternance of the single and double bonds that compose the chain - forming a "soliton"; in those cases, the bond lengths slowly change along the length of the soliton and, as with the polaron case, the charge carrier can move along the backbone.

Since the alteration of the physical shape of the molecule is central to the mechanism of electronic conduction in polymers, it therefore follows that the arrangement of the chains would be of prime importance in the transfer of said conduction. An ordered arrangement of the chains would permit certain favorable pathways of charge transfer from molecule to molecule to occur reliably throughout the structure, or, to the contrary, suppress them. Close proximity of regularly arranged chains would make the transfer of charge to occur more frequently. Thus the periodic arrangement of the molecular chains plays a very important role in the conduction mechanisms of polymers.

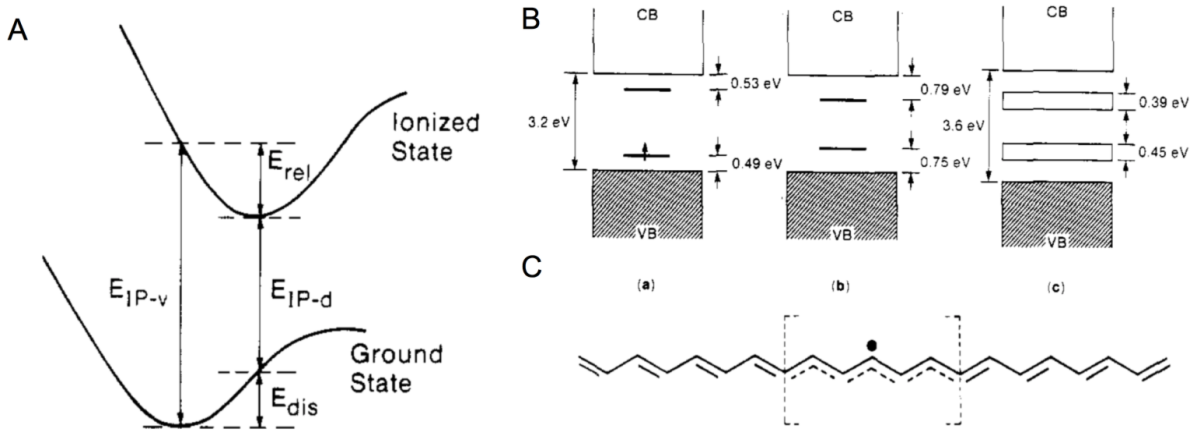

Figure 1.2: Polarons and solitons[49]. **A**) Illustration of the energies involved in a molecular ionization process. $E_{\mathrm{IP-v}}$ is the vertical ionization energy, E_{rel}, the relaxation energy gained in the ionized state, E_{dis}, the distortion energy to be paid in the ground state in order that the molecule adopts the equilibrium geometry of the ionized state, and $E_{\mathrm{IP-d}}$, the ionization energy of the distorted molecule. **B**) Evolution of the polypyrrole band structure upon doping: (a) low doping level, polaron formation; (b) moderate doping level, bipolaron formation; (c) high (33 mol %) doping level, formation of bipolaron bands. **C**) Schematic illustration of the geometric structure of a neutral soliton on a trans-polyacetylene chain.

1.2 Polymer Crystallinity

When the average person thinks of crystals, it is primarily in the context of rigid, conventionally periodic structures exhibited by mineralogical specimens. If a material scientist thinks of crystals, this understanding is usually compounded with that of the closed-packed arrangements of metallic, ionic, or covalently bonded structures; but crystalline behavior is not limited to metals and ceramics. As it is defined as nothing more than a periodic arrangement of a repeated feature, polymers and complex organic molecules too can crystallize[50]. Their long, often quite flexible chains can bend on themselves, causing the backbones to align; in some instances, this localized arrangement is energetically preferred to the amorphous, "plate of spaghetti" type of configuration, and local crystallites, or "lamellae", form, as shown in Fig.1.3. Small organic molecules also show this tendency. This packing leads to a change in a range or properties of the materials; because of the increased proximity of the chains to one another, the polymer becomes denser, and the molecules become more strongly linked to one another due to the increased number of Van der Waals interactions between them, in addition to other electronic phenomena that begin taking place when the backbones and side chains begin to mesh. This inevitably telegraphs an alteration of the macroscopic, mechanical[51], optical, and electronic properties of the polymer; highly crystalline polymers tend to be stronger, tougher[52], and more opaque than their amorphous counterparts. The

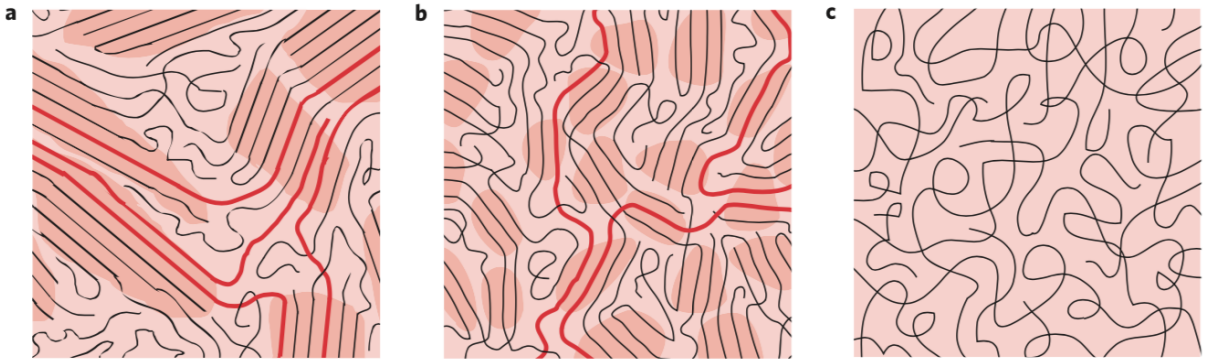

Figure 1.3: Schematic diagram of the crystallinity of a polymer[54]. **a** shows a semicrystalline configurations, where polymer chains fold on themselves and align to form areas of high order, connected by an amorphous phase; **b** shows smaller crystalline domains and **c** demonstrates a completely amorphous configuration.

effects of crystallinity on elastic properties, plastic deformation, and light absorption and transmittance can be quite drastic and have been extensively studied[53].

In the case of conducting polymers, crystallinity plays a huge role on the conductivity. While in an amorphous state charge transport between chains requires chance hopping of a charge from chain to chain, the alignment of the backbones cause the π bonds to regularly overlap – which means that the charge carriers now have an opportunity to not only move along a polymer chain, but reliably hop between them. If the packing is particularly efficient in the alignment of the π bonds, the conductivity is generally greatly improved[55]; in light of this, the control of crystallinity of conductive polymers is a crucial factor in their understanding and improvement. On a small scale, the stacking of the backbones along the π bonds, the interdigitation of the side chains, and the orientation of the molecule planes relative to one another all play a role in how charge is allowed to pass from chain to chain. These configurations have been, and are still, studied through simulation[56] and ab inito calculations, as well as diffraction and high-resolution phase imaging. The preferential self-assembly of the molecules through the stacking and alignment of their π bonds is fascinatingly complex, and much effort has been put forth to characterize them[57, 58, 59, 60]. In the case of the polymers studied here – P3HT[61], T1, and PBTTT – the backbones do crystallize in an arrangement that favors π stacking, leading to the possibility of easy chain to chain charge transfer. This implies that from a larger perspective, grain structure and the arrangement of the crystalline domains, their relative sizes and boundaries, the angles at which they lie, their preferential aspect ratios, the arrangements of the molecules within them – these all contribute greatly to the conductivity character of a polymer as well. To understand and control the crystallinity of conductive polymers could potentially truly bring about their rise above their silicon counterparts.

Of course, the extent to which crystallization occurs depends greatly on a number of

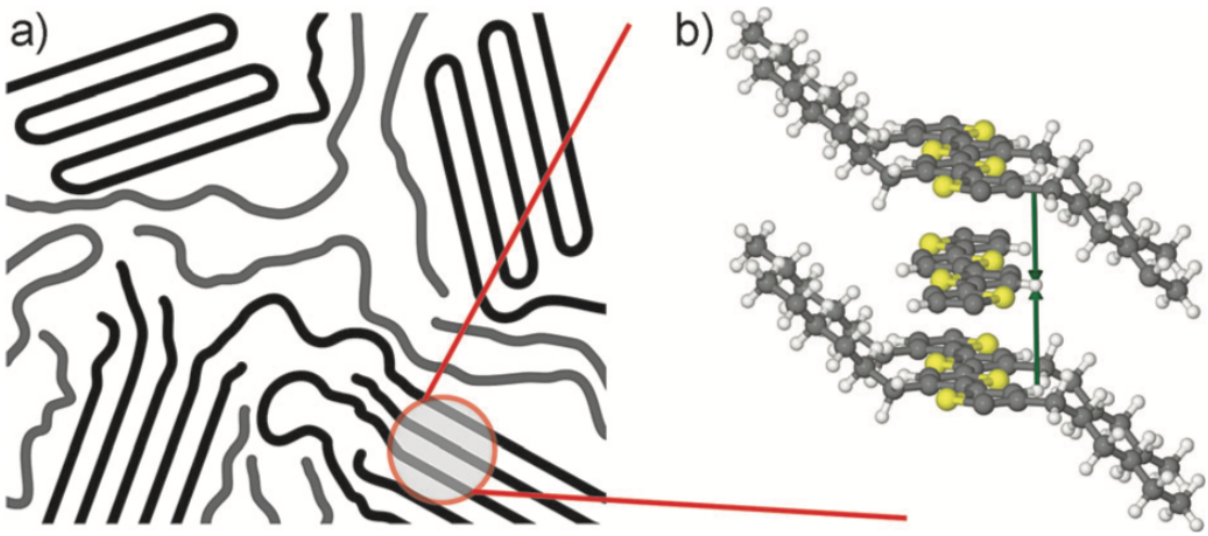

Figure 1.4: Schematic of P3HT stacking.[62] **a** Diagram of the crystalline arrangement of the polymer, with crystallites in black and amorphous regions in gray. **b** Molecular view of the stacking of the P3HT chains in the π-π direction (green arrows). Some side chains have been omitted for clarity.

factors. In the case of polymers of very high molecular weight, crystallization is hindered or rendered altogether impossible by the sheer improbability of aligning the entirety of the chain lengths to each other, and whatever crystalline domains exist find themselves surrounded by amorphous regions. The nature of the monomer units of which the molecules are composed dictate the overall flexibility and spacial arrangement or coiling of the chains; certain bonds are rigid, while others can rotate, either completely freely or at specific angles, which can lead to a variety of complicated spacial geometries – from flat and planar to spiraled, coiled, or some other bizarre configuration. The addition of certain dopants needed for conductance complicates matters further, as the are usually introduced in rather large quantities (sometimes as much as a 1:1 ratio of dopant to conducting polymer) and interact both mechanically and chemically with the chains. Steric hindrance that arises from side chain and end radical geometry can also prevent the formation of ordered structures, although in some cases the chains can fall into an interlocking pattern that actually promotes periodicity. In certain cases, the conductivity of conductive polymers has been shown to not depend on chain packing geometry as much as surface and grain boundary interactions.

The conditions under which the molecules were formed plays a major role in determining the kinetics and wetting properties of the polymers. Annealing affects the mobility of the chains and tends to coarsen the crystalline domains, allowing them to grow quite in the same way as would grains in metals, even full crystallization is never quite achievable – except in special cases where single crystals are carefully, individually grown, or if the molecules

are small enough to be able to move relatively freely when given the energy. Crystallization can also occur when the polymer is subjected to strains[63], as the primary deformation mechanism is the sliding of the chains past one another. When an uniaxial stress is applied, the chains move and preferentially align along the stress direction. Certain solvents modify the surface energies of the polymers, which leads the chains to favor certain arrangements and reject others; hydro- and oleo-phobic/phillic species are of particular importance to these mechanisms. Significant amounts of crosslinking – covalent or hydrogen bonding between chains – can prevent crystallization altogether; if the molecules are grafted to one another, the amount of energy, be it thermal or mechanical, supplied does not matter since the material cannot plastically deform unless chemical bonds are broken, at which point the polymer becomes melted or destroyed. Polymer crystallinity is thus a complex landscape of a number of variables that can be manipulated and regulated; to harness the ordering of the chains means to control the polymers' properties.

1.3 Characterization Techniques for Polymers and Soft Materials

An outstanding question in the field of semicrystalline polymer characterization has been how to directly observe the microstructure of the polymer chains, and particularly the nanoscale orientation of crystalline domains. For example, the preferential crystallization of poly(3-hexylthiopene)(P3HT) along its π–π bonds allows electrons and holes to easily move within the crystal bulk and thus has a direct effect on device efficiency. It then follows that a study of the location, size, distribution and local orientation of the crystalline domains is critical for engineering the improvement of organic photovoltaics. Polymers are usually mostly composed of light elements such as H, C, N, and O, and are held together by Van der Waals interactions. This makes their structure relatively weakly scattering (as opposed to materials containing heavy elements) and sensitive to radiation damage and environmental degradation.

General techniques such as NMR[64], and UV-vis[65], infrared [66, 67], and Raman[68, 69] spectroscopy are widely used to obtain information on the chemical composition of the polymers. Spectroscopy relies on the absorption of characteristic wavelengths by specific chemical bonds, from which the molecular structure of the polymer can be deduced. Differential scanning calorimetry[70, 71, 72] approaches the problem from a different angle by providing data on thermodynamic transitions as the material is heated or cooled, and thus can give a measure of its crystallinity; this fraction of crystalline to amorphous material can also be extracted from NMR data. X-Ray diffraction methods, such as XRD[73, 74, 75], SAXS [62, 76, 77], and WAXS[78, 79, 80, 81] have by far been the most often used methods. The crystalline arrangement of polymers allows for diffraction to occur, and characteristic spacings between the backbones, as well as between their side chains, can be extracted. While polymers very seldom exhibit large perfect crystals, the regularity of chain alignment

is enough for Bragg scattering to reliably occur, given of course that the sample is thick or crystalline enough. X-rays are relatively low-energy when compared to electrons, and therefore incur less damage to the polymers during data acquisition. Unfortunately, this method is rendered difficult by scattering from non-crystalline regions of the sample, which obscure signal, and weakly bonded molecules, which can heat up and start vibrating, further disrupting the crystallinity and making the signal difficult to interpret. This is usually palliated with a fit to a model of the polymer structure under investigation and comparison to an artificially generated Bragg scattering pattern. Because the molecular structures of the polymer chains are usually well-known, modern computational capabilities allow for the testing of many different configurations, and the empirical structure can usually be reliably fitted to a theoretical model[82]. Thus X-Ray diffraction can be used to fully characterize a single unknown polymer structure through a thorough investigations of the reflections of a carefully grown crystal, or to obtain more general information of the types of crystalline components or characteristic spacings present in a polymorphic or complex sample. In wide-angle X-ray investigations, the lattice spacing measurements can be made precisely enough to determine lattice strain [83, 84]. X-Ray methods are also used to determine the preferential orientation of polymer thin films, as the chains can crystallize into asymmetric lamellae that will lie in certain preferred orientations depending on the molecular structure, processing methods, or additives present.

All of the the aforementioned techniques, however, provide data averaged over the bulk of the sample and thus cannot construct a map of the relative position of the crystallites over a local area; these measurements provide no information on the structure at smaller scales and their variation close to boundaries, inclusions, and other artifacts. The information obtained is statistically significant as an ensemble view but not as a local map, even though certain mean quantifications can be approximated – such as average grain size from XRD peak widths, for example, or fraction crystallinity calculations based on a normalization of peak intensity to the amorphous scattered background.

There exist characterization techniques such as electron backscattered scanning diffraction (EBSD)[92] that can efficiently map the local grain structure in metals and ceramics at the nanometer scale; unfortunately, the sensitivity of polymers to electron bombardment precludes the use of these techniques for semicrystalline organic systems. Most characterization techniques that image a sample's structure directly require an electron beam to reach resolutions at the lengthscales on the order of the features of interest, the most common among them being Scanning Electron Microscopy (SEM) and Transmission Electron Microscopy (TEM). Since polymers are not conductive, SEM relied on the coating of the sample surface in a conducting film, usually gold. SEM investigates the surface features of the sample and provides structural and morphological information on the material, but does not make use of the diffracting nature of crystalline domains. TEM, on the other hand, can.

When applied to polymers, TEM becomes tricky, as beam damage can be very pronounced. Multiple studies have been performed on the effect of accelerating voltage and beam size on polymer structures[93, 94]. Cooling the samples with liquid nitrogen or helium mitigates the damage for most polymer systems[95]; in the research presented here, for ex-

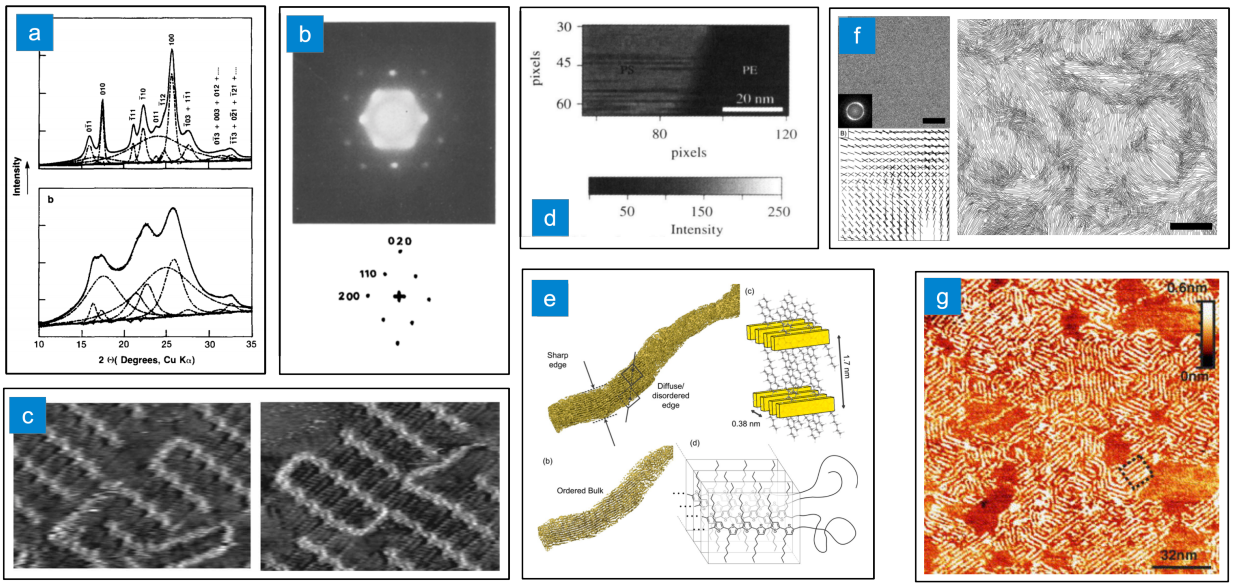

Figure 1.5: Overview of published results on characterization techniques applied to crystalline polymers. a) XRD spectrum of polyethylene tetraphtalate[85], with a highly crystalline sample (top) used for a reference template and a more typical, less crystalline specimen (bottom) showing less resolved peaks. b) Nanodiffraction composite of a polyethylene single crystal[86]. Many faint diffraction patterns from varied locations within the crystal were averaged to produce the final image. c) Scanning tunneling micrograph of poly(3,3"-didodecylquaterthiophene)[87], showing high resolution of the ordered chains. Field of view is 13 nm x 19 nm. d) Spatially resolved boundary map between polyethylene and nylon using scanning EELS spectra[88]. e) Cryo-EM tomography of P3HT[89], showing lamellar chain arrangement. f)HRTEM of a small molecule with Fourier analysis used to extract chain orientations and map them (right)[90]. g)AFM of P3HT films[91], showing dispersed terraces of crystalline domains.

ample, all samples were cooled to liquid N2 temperatures for data collection. Since polymers usually have a low melting temperature and electrical conductivity, the most common damage mechanism is melting, although cross-linking, chain twisting, or other effects can also significantly compromise film integrity. Higher accelerating voltages contribute to a better conservation of the sample's integrity as they limit the volume and time of interaction of the electrons within the polymer film, and thus prevent some of the generation of secondary electrons that proceed to travel laterally through the sample and continue to cause damage even outside of area directly under the beam. While different polymer systems respond differently to beam damage, with some considerably more robust than others (e.g. polyethylene), diffraction signal is observed to disappear within seconds even under low illumination. This issue has led us to choose high accelerating voltages (300 kV) and low illuminations

(on the order of a few $Å/s^2$) and acquire data by stepping blindly to a new area of the sample where diffraction was suspected to occur. For each polymer system, in order to gain a qualitative understanding of the timescales of the beam damage, we performed several consecutive scans of the same area before collecting data. In certain cases (polyethylene oxide, P3HT, T1), even with the most conservative parameters possible, diffraction data could only be collected once, on the first scan. For more robust, thicker, or more crystalline systems (polyethylene, PBTTT), at most two consecutive scans could be performed before complete loss of diffraction data.

Electron diffraction from polymers has nonetheless been exploited, with a notable example being the characterization of the lattice of polyethylene through electron diffraction of a large single crystal[86]. Because the diffraction signal from a single location is too weak, the full pattern was obtained by summing the patterns from many locations throughout the crystal. Sometimes the polymer film provides no contrast at all and has to be stained with heavier elements[96], which bind to the chains in specific ways and retain the characteristic crystalline structure of the material. The advent of faster and more sensitive detectors has allowed the imaging of polymers in both bright and dark field, where crystallinity could be seen and characterized.

A select few spatially resolved techniques have had success in mapping local polymer structure (ref Fig.1.5) . EELS spectra have been used in conjunction with STEM to differentiate between polymer molecules and their bonding types[88]; this resulted in the construction of a map where grains of the two different molecules could be drawn. A high-resolution TEM technique has shown local distribution of polymer structure by tracing the lattice fringe arrangement visible in bright field[90, 97]. The algorithms used in that study are expanded upon in the research presented here (ref. Chap 3-4). There, Fourier techniques have been implemented to follow the orientation of phase-contrast lattice planes visible under regular bright field illumination, and a trace map of contiguous polymer chains was drawn. AFM studies have also been used to augment the results by providing information on the surface roughness of the film[91, 98], while scanning tunneling microscopy has produced some particularly striking images of the surfaces of certain polymer thin films, showing the crystalline arrangement of the chains, their bending and side-chain interdigitation[87]. Cryo-TEM tomography localized the polymers via diffraction of the encasing ice[89], as well as direct imaging and tomography of the chains themselves. In this study it is our goal to challenge the shortcomings of bulk techniques and expand on the few locally resolved ones by using low dose scanning transmission electron microscopy to obtain spatially resolved maps of the crystalline domains through diffraction. We use a technique based directly on the diffraction data of the polymer and reconstruct all real-space images in post-processing.

Chapter 2

Benchmarking the technique on P3HT:PS semicrystalline thin films

2.1 Motivation and overview

Poly(3-hexyl-thiophene-2,5-diyl), or more commonly referred to as P3HT, is currently one of the most successful conducting polymers. Even though it is a rather recent addition to the polymer field, it and its close doping companion, [6,6]-phenyl-C61-butyric acid methyl ester (PCBM), have been *extensively* studied[99, 100] and are starting to see some serious applications in industry. The P3HT:PCBM duo has shown good relative conductivity and stability when compared to the rest of the CP cast, and is being especially groomed for large-scale photovoltaic and field-effect transistor applications. The structure of P3HT is as one would expect of a CP, with the alternating π bonds carried by the thiophene rings. The molecules stack with the flat rings lying on top of one another, and the crystal structure leads to reasonable amounts of diffraction. Its lamellar structure and lattice parameter have also been characterized[101]. In an effort to understand the crystal structure of CPs, P3HT was an ideal candidate for method testing and technique refinement.

2.2 Experimental Methods

Sample preparation

Regioregular P3HT was synthesized (93% regioregularity), purified, and characterized using the techniques described by Bhatt et al[102]. The molecular weights of P3HT and PS used in this work were 9 kg/mol and 10.8 kg/mol, respectively. P3HT and PS were dissolved separately in a solution of chlorobenzene[103, 104] with a concentration of 10 mg/mL and subsequently filtered with 0.2 mm polytetrafluoroethylene filters. A 50:50 w/w blend of P3HT and PS was made by blending equal weight of P3HT and PS solutions. Initial samples were drop-cast, but turned out too thick for proper TEM analysis. The mixed solution was

spin-coated onto a glass substrate at 3000 rpm for 60 s, resulting in a 30 nm thick film which was then deposited onto a lacey carbon-supported copper grid via lift-off in deionized water. The TEM samples were dried at room temperature in vacuum for 24 h and subsequently annealed for 1 h at 150°C in an Ar-filled glovebox.

The 4-dimensional scanning electron microscopy (4D-STEM) data was acquired using a FEI Titan TEM operating at 200 and 300 kV (Fig. 2.1a). A custom written Python script directed the STEM acquisition, which used a convergent beam with a convergence half-angle of 0.51 mrad (Fig. 2.1a) to raster over an m by n area and collect a stack of diffraction patterns (Fig. 2.1b). While the convergent probe allowed for STEM rastering, the small convergence angle ensured that the diffraction disks did not overlap in the diffraction patterns (DPs). The probe in this study was not aberration corrected. Initial low-dose low-mag STEM images (dwell time of 1 microsecond) enabled us to find the regions of interest. Annular dark-field STEM images were collected with a semi-angle of 34 mrad. The rastering was performed with a 20 and 40 nm step size and an exposure of 70 and 50 ms respectively; the time was chosen to optimize the diffracted signal given a chosen probe current. The 20 nm minimum step size was chosen because it was the smallest step size that did not result in a decrease in the Bragg scattered peak intensities. The diffraction images were captured with a Gatan Orius camera, but a more sensitive camera might be able to record similar diffraction intensities with a shorter dwell time and electron dose, effectively increasing the spatial resolution of the technique. The presence of sulfur atoms within P3HT backbone allowed us to map the sulfur K-edge via electron dispersive spectroscopy (EDS) in the TEM to confirm the presence and distribution of P3HT molecules. The stacks of DPs obtained during each scan were subsequently mined to reveal the distribution of the crystallites. Each DP in the set corresponds to a real space position (i, j) of the rastered beam; crystallite orientation parameters can be extracted by locating and indexing the Bragg diffraction spots. While a single diffraction pattern can be manually indexed, 4D-STEM can raster areas as large as 128 by 128 probe positions, resulting in 16384 individual diffraction patterns that require automated analysis routines.

Electron dose considerations

Electron beam damage in polymers is ubiquitous, and several recent review articles address this issue [105, 106]. Experimentally, we observe the damage as a rapid disappearance of diffraction spots; changes in accelerating voltage between 200 and 300 kV did not show any observable difference in diffraction persistence. Careful studies of diffraction intensity as a function of time can result in a characteristic dose, D_e, for a given material[105, 107, 106] these measurements were not carried out here. Often the term "low-dose" electron microscopy is used to describe parallel beam TEM with an electron dose on the order of 10 $e^-/Å^2$. Because this is a convergent beam technique and all the electrons are focused to a small area (about 4000 $Å^2$), the electron dose rate is high at about 8000 $e/Å^2s$. The short exposure time of 70 ms reduces the dose to about 600 $e/Å^2$, and one can decrease the dose even further by defocusing the probe over a larger area. Measurement of the probe

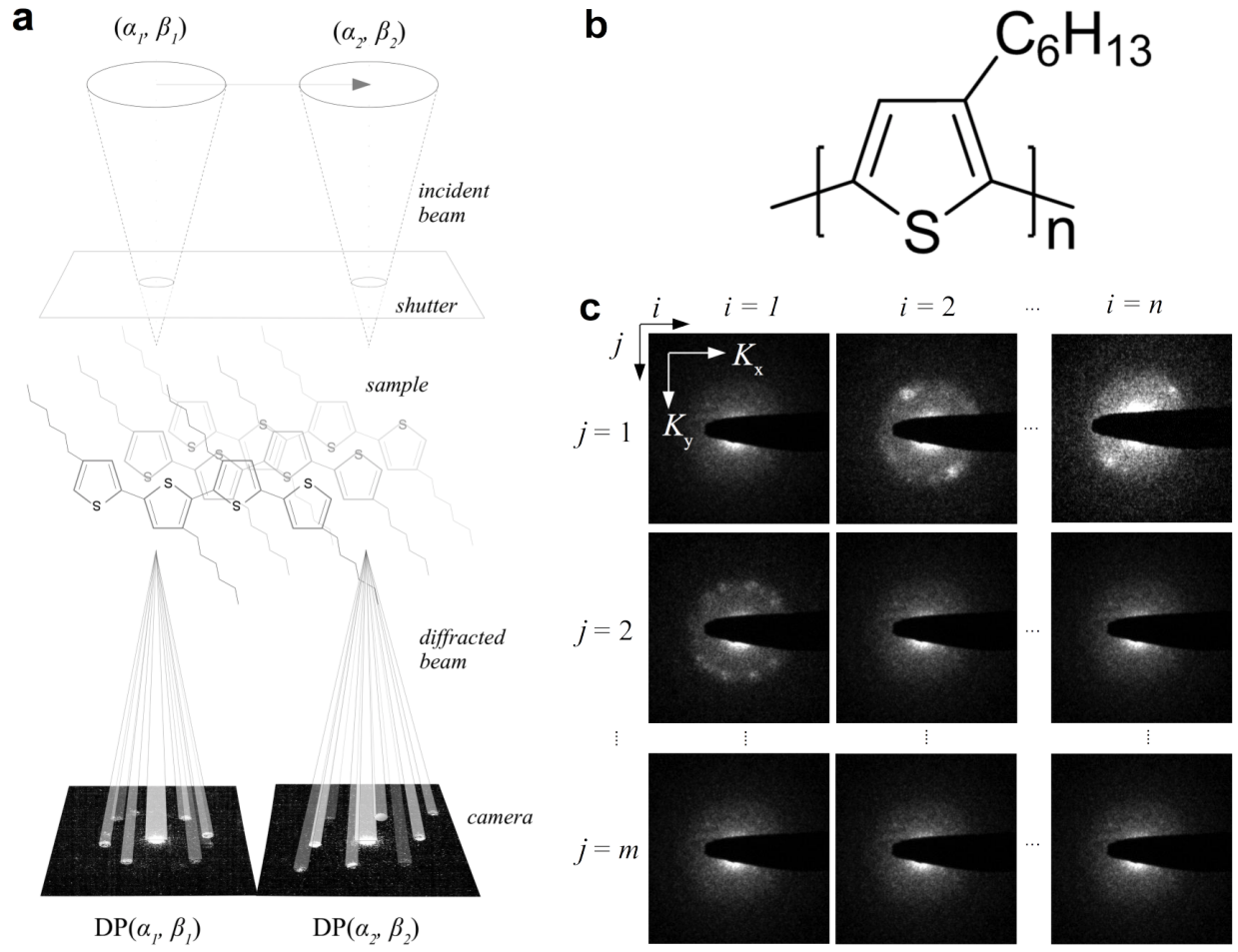

Figure 2.1: The 4DSTEM experiment. (a) Convergent beam rasters across the sample (i,j) and captures a full diffraction pattern (K_x,K_y) for each probe location. (b) Molecular schematic of the P3HT monomer structure. (c) The data takes the form of a 4-dimensional n × m set where each pixel in real space (i, j) corresponds to a full diffraction pattern (K_x, K_y).

size was done by imaging the convergent beam at high magnification onto a charge-coupled device. A profile of the probe image at 200 kV shows a shape with a full-width half-maximum (FWHM) of 7 nm and a dose of about 2000 e/Å^2 at its peak. The total beam current was measured at 5 pA, which corresponds to an average electron dose of 8000 e/Å^2 , over an area with a diameter defined by the FWHM of 7 nm. Ten nanometers from the center of the probe the dose is still on the order of 20 e/Å^2 . This data shows that not all parts of the sample receive an equivalent dose; the optimal probe shape for diffraction studies of polymers remains to be investigated. The impact of this technique is the ability to step to a

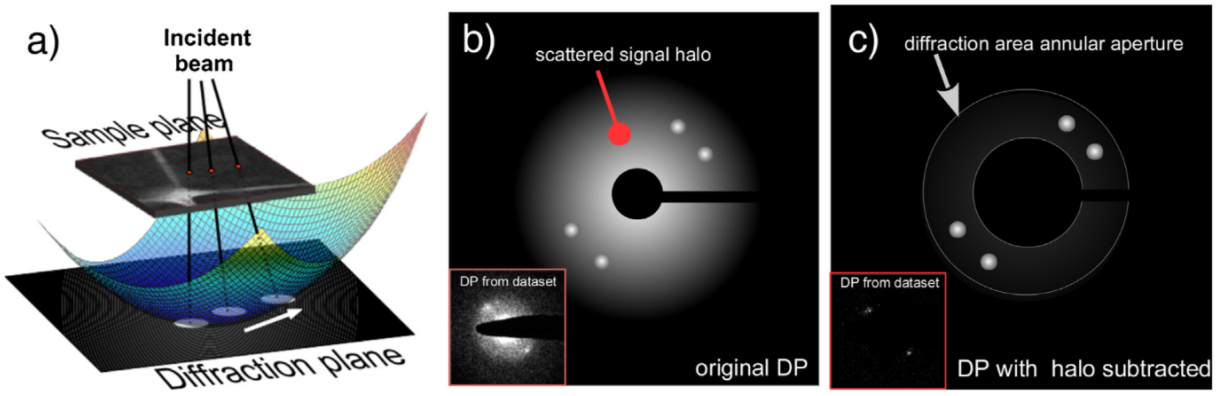

Figure 2.2: Schematic illustration of the algorithm developed. (a) Diagram of the effect of the beam sway as it scans the sample; the colored surface is a parabolic fit to calculated beam shifts for the P3HT sample dataset used in this study. (b) Diagram of a typical diffraction pattern obtained in 4D-STEM, with diffraction spots superimposed on a background scattered halo. Inset shows a DP from a gathered dataset. (c) Diffraction pattern after processing, with the background halo removed and the diffraction spots clearly featured. A virtual annular aperture used for virtual dark field calculations is outlined in white. Inset shows the DP from (b) after application of the algorithm.

new area of the sample that has not yet been exposed to electrons. The diffraction pattern is robust against changes in focus conditions so one does not need to expose an area to achieve a focus condition. Additionally, diffraction is efficient at using electrons, and contrast in a diffraction pattern is much easier to achieve than in a conventional TEM image. The short time scales used effectively eliminate errors and distortions that could be incurred by stage vibrations or sample charging. By keeping track of the history of the stage motions, one can step to a new area of the sample with the beam blocked and then acquire a dataset with the possibility of capturing an interesting area. In this work we keep track of the exposure in an effort to prevent the sample from altering its structure.

2.3 Analysis algorithm

Methods for manual and automated analysis of diffraction patterns with high signal/noise have been reported previously[108, 109, 110]; however, automated analysis of DP sets from semicrystalline polymers, such as those explored here, requires additional steps. In soft materials Bragg reflections from crystalline features have weak intensities due to the low electron dose. Additionally, they are superimposed onto a monotonically decaying background (Fig. 2.2b), which varies in intensity from one probe position to the next. We propose that this background arises from interactions between the incident beam and amorphous regions in

the sample (amorphous halo). Furthermore, the beam tilts as it rasters the sample, which causes the diffraction patterns to shift within the detector's field of view. This causes the patterns to be misaligned non-linearly with respect to one another within the dataset (Fig. 2.2a); this effect is greater at lower magnifications. The beam- stop, necessary for image sensor protection, hides the central transmitted beam and eliminates a point of reference that could have been used to align the patterns to one another.

The first step in the algorithm is to align the DPs. The true center of each diffraction pattern is found by fitting an ellipse to a subset of points taken from the amorphous halo and calculating its center of mass. The patterns are then shifted such that the calculated center matched the center point of the detector's field of view (Fig. 2.2a).

The second step is to remove the amorphous halo; a different amorphous halo is subtracted from each DP. First, the averaged intensity of the scattered amorphous background is computed using an aperture that excludes the ring where diffraction occurs, obtaining an amorphous scale factor hi,j for each probe location (i, j). The matrix $h_{i,j}$ is then normalized by a constant corresponding to the largest value of $h_{i,j}$. A reference halo image I_h (K_x , K_y) is generated by summing all of the diffraction patterns and normalizing by the number of probe positions. The intensity values of the reference halo image are then multiplied by $2h_{i,j}$ to obtain a reference halo tailored to each probe position (i, j); the factor of 2 allows for an efficient suppression of the amorphous signal. The specific background halo image is then subtracted from its respective DP. Negative pixel values resulting from the subtraction are set to zero. This effectively decouples the diffraction signal from the scattered halo surrounding it. The halo subtraction procedure is illustrated schematically in Figs. 2.2b and c; typical data before and after subtraction are shown in the insets. After the correction, all DPs exhibiting no Bragg diffraction are reduced to flat, near-zero images.

The third step is to generate virtual dark field images by summing the signal from each DP that falls within a defined aperture area. This step is equivalent to the experimental use of an objective aperture selecting given diffraction conditions[111]; in the case of soft materials, the ability to obtain all possible dark field images with a single exposure eliminates damage that would be caused by multiple exposures. Of course, virtual dark field images can also be obtained by summing the total intensity at each probe location without any processing.

Finally, the positions of the diffracted spots can be found by locating peaks of highest intensity whose centers fall within a narrow range of distances from the center, as defined by the polymer's observable Bragg reflections and achieved via a virtual annular aperture (Fig. 2.2c). Acquired diffraction frames were of three types: those with only one Bragg reflection present per frame, those with more than one Bragg reflection per frame, and those with no Bragg diffraction present. Diffraction patterns containing more than one crystal orientation occur either because the beam has sampled adjacent crystallites or because there are layers of crystalline material; the multiple orientations are twists about the axis parallel to the beam. Frames with no visible diffraction are either not aligned or not crystalline. Some DPs exhibit bright diffraction disks while others can barely be distinguished. In this study, we conservatively accepted peaks as "visible" only if their integrated signal over the

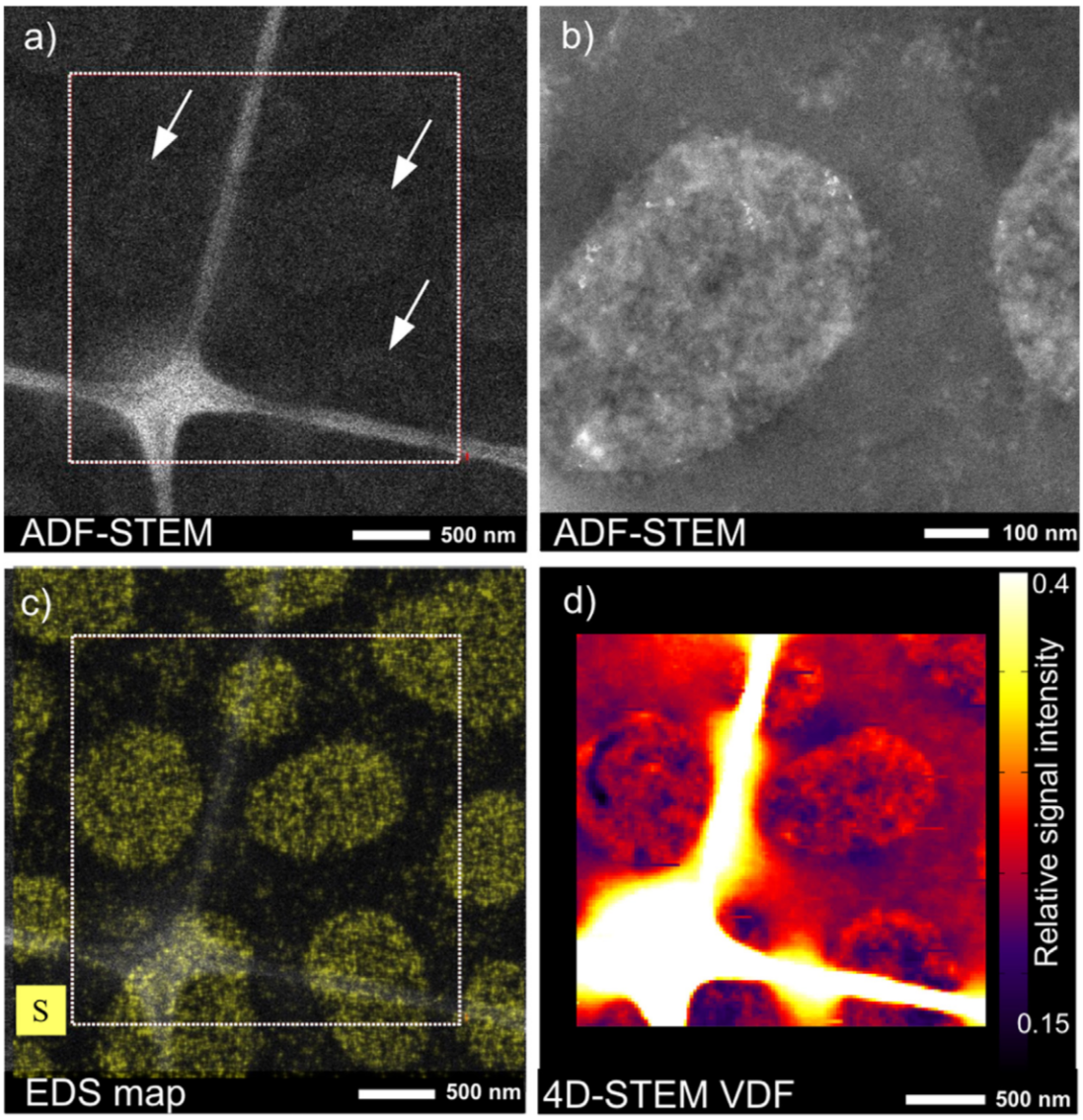

Figure 2.3: Raw and minimally processed images for P3HT/PS (200 kV). (a) ADF-STEM image with oval clusters of P3HT shown by white arrows. (b) Aggregate at higher magnification displaying structure within. (c) EDS map with sulfur signal in yellow. (d) Preliminary virtual dark field image reconstructed using the entirety of the DP field of view.

disk area was strong enough to outcompete peaks arising from background noise after halo subtraction. As the center of each DP is known, we can then easily compute the relative angle of the diffraction spots and create a Bragg diffraction angle map.

Crystallinity of P3HT:PS

Fig. 2.3a-c show images of the P3HT:PS sample captured at an accelerating voltage of 200 kV. Under annular dark field (ADF) STEM mode, large (about 200 nm) oval disks were observed (Fig. 2.3a); when surveyed at higher magnification they were shown to exhibit rough internal features (Fig. 2.3b). Sulfur EDS confirmed that these structures were mostly P3HT (Fig. 2.3c).

A virtual dark field image with an aperture that includes the whole field of view of the detector is shown in Fig. 2.3d, prior to alignment or halo subtraction. This image contains signal from both the diffracting and amorphous regions and provides a measure of the relative thickness of the sample, which shows structure that was not discernible under ADF-STEM conditions. The lacey carbon support scatters electrons more intensely than the polymer sample and thus appears saturated on the image due to the very bright background halo it generates.

The results of our analysis on the P3HT:PS sample are presented in Figs. 2.4 and 2.5. Fig. 2.4a is a ADF-STEM image of an independent P3HT:PS blend taken at 300 kV. In some experiments, the P3HT-rich oval disks appeared brighter than the background (Fig. 2.3b), while in others they appeared darker (Fig. 2.4a). The origin of this difference in contrast is presumably due to a thickness differential in the PS film surrounding the oval structures. The use of different apertures allows us to probe different aspects of the sample morphology, as exemplified in Figs. 2.4b-c. The virtual dark field image in Fig. 2.4b is constructed before subtraction of the background halo; we can see that without halo subtraction or use of a virtual aperture around the diffraction locations, the scattered amorphous signal dominates the image. When our algorithm is employed, however, the on-axis crystalline domains are immediately distinguishable (Fig. 2.4c).

An aperture-aided virtual dark field, similarly constructed to the one shown in Fig. 2.4c, is presented from a different sample in Fig. 2.5a. The virtual dark field image is normalized and locations where crystalline reflections are strongest appear in white and yellow. These results clearly show that the oval structures are not exhibiting Bragg reflections over their entire area. The Bragg reflections that do appear on the DPs are shown in Fig. 2.5c, with their scattering angle plotted in color and overlaid onto the ADF image. While a few of the crystalline reflections can be seen scattered throughout the space between the aforementioned large oval structures, most of the crystalline reflections seen are contained within those oval regions. Furthermore, clusters of adjacent pixels showing Bragg peaks with similar orientations can clearly be observed, and can span distances as large as 80 nm. The distribution of the crystallite orientations mapped within the oval clusters appears to be fairly uniform, and the crystalline features are oriented randomly with respect to one another. Reflections around 90◦ are seldom picked up by the algorithm, as they are masked by the beamstop, as illustrated in the colorwheel legend of Fig. 2.5b. Finally, we can obtain a measure for the localized degree of crystallinity by computing the ratio between the now decoupled diffracted and amorphous signals. The diffracted signal is taken to be the VDF such as the one in Figs. 2.4c and 2.5a, where only diffracted Bragg peaks appear as non-

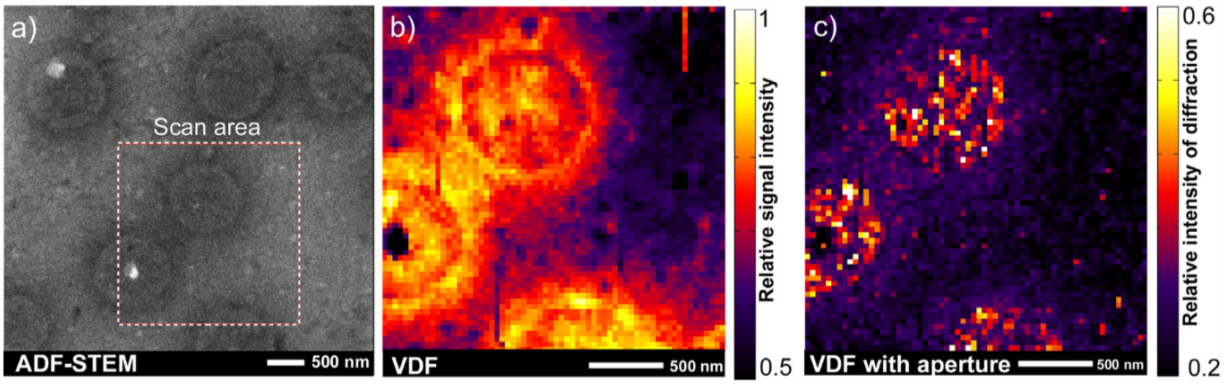

Figure 2.4: Algorithm applied to P3HT:PS sample at 300 kV. (a) ADF-STEM image of P3HT sample, with the 4D-STEM-rastered region outlined in a white dashed square. Two VDFs of the 4DSTEM dataset (step size of 40 nm) are shown. (b) VDF image constructed from signal summed over the whole field of view of the detector. (c) VDF image constructed from halo-subtracted signal within a thin virtual annular aperture that only includes locations where diffraction peaks occur.

zero features. The amorphous signal is an i by j map of the amorphous scale factors $h_{i,j}$ obtained previously. This result is shown in Fig. 2.5c and further confirms the location and distribution of P3HT crystalline features within the oval structures.

Measurements from individual diffraction patterns indicate that the P3HT polymer lamellae could be lying edge-on as well as face-on, as described by Brinkmann and Rannou[112], for a low MW semicrystalline P3HT sample. Visual measurements of the Bragg reflections observed yielded an average interplanar distance of 3.87 Å ± 0.12 Å over 41 patterns; conversely, the same measure- ment was made using the Bragg reflections found by the algorithm, which resulted in a value of 3.71 Å ± 0.29 Å over 1805 patterns. The error is larger for the algorithm due to the non-uniform illumination of the Bragg spots, which leads to error in the estimation of the true center of the peak. This measured periodicity at 3.8 Å agrees well with the 3.9 Å stacking period of successive polythiophene backbones along the b-axis of a monoclinic structure modeled by Kayunkid et al.[113] and observed by others[112, 114, 115, 116]. This reflection corresponds to the (020) reflection of the monoclinic structure proposed by Joshi et al.[114] (2008) and Brinkmann and Rannou[112], or the (020) reflection of the orthorhombic structure proposed by Tashiro et al.[116] and Prosa et al.[115]. This periodicity corresponds to the π-π bond spacing and would appear on the DP only if the crystallite is oriented edge-on, with either the a- or c-axis parallel to the beam[117]. This spacing, however, is extremely close to the (002) reflection characteristic of monomer spacing along the backbone (3.88 Å)[112] that would be exhibited by face- on oriented crystallites, to the point that we cannot distinguish between the two. Furthermore, for a film thickness of approximatively 30 nm the ratio of edge-on to face-on orientations is estimated to be about 1 according to Huang et al.[118], which means that both reflections are equally likely

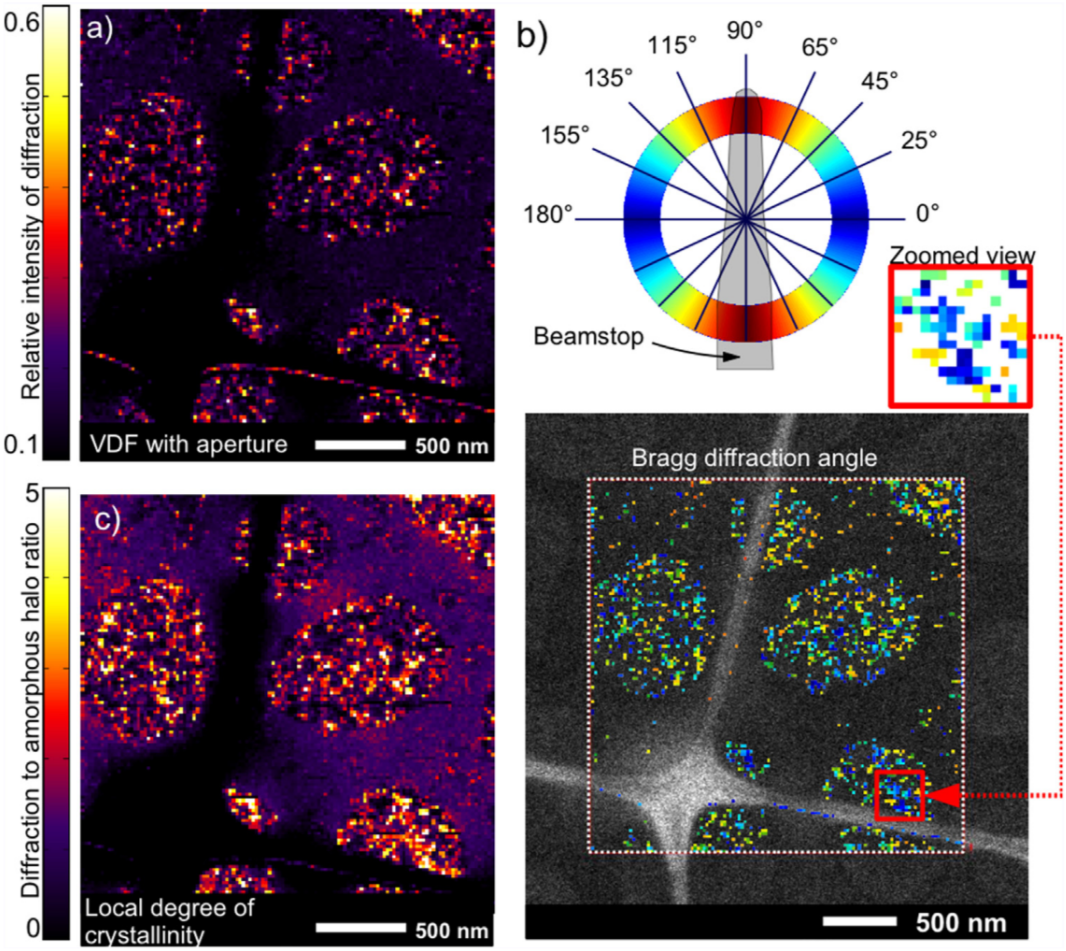

Figure 2.5: Algorithm applied to P3HT/PS sample at 200 kV. (a) Normalized VDF showing the relative intensity of the Bragg reflections, obtained from a processed dataset where the background scattered halo has been removed. (b) Map of a normalized local degree of crystallinity, as defined here by the ratio of the Bragg diffraction signal to the extracted amorphous scattered signal. Yellow spots indicate high degree of crystallinity. (c) Bragg diffraction angle map of the rastered region, with the angle map overlaid onto the ADF image.

to occur. Diffraction spots generated by longer stacking distances and thus appearing closer to the center in diffraction space while present within the signal, are completely masked by the central transmitted beam and therefore could not be extracted.

If one of the axes p of a crystallite is parallel to the electron beam, diffraction spots indicate that its orthogonal axis is randomly oriented in twists about p. The Bragg rotation map shown in Fig. 2.5c shows that crystallites can be bigger than our step size of 20 nm, with slight misalignments across adjacent probe positions. This is expected; indeed, in addition

to a low signal to noise ratio of the diffracted signal, which makes some peak locations ambiguous, polymer chains could show a propensity to bend even when in a semi-crystalline state. This would lead not only to a slight rotation of the Bragg peaks from one pattern to the next, but also to the dis- appearance of others as the lattice planes twist and bend out of axis alignment. This would indicate that the crystalline regions mapped here are only a subset of larger and/or more numerous crystalline features, which are not accessible through 4DSTEM unless the sample is tilted into the corresponding Bragg conditions. Therefore, dark areas on the virtual dark fields do not necessarily indicate amorphous regions, although those are bound to be present as well. While not investigated in this study, these ambiguous regions could be characterized with a combination of tilting experiments and better dose control.

2.4 Conclusion

We have introduced a scanning transmission electron microscopy technique to obtain spatially resolved maps of crystalline domain orientations over a field of view on the order of 1 micron with a spatial resolution of 20 nm. Corrections for beam tilt and amorphous scattering were essential for obtaining these maps. This technique was applied to a blend of P3HT and PS with containing P3HT-rich oval shaped domains. Regions on order 80 nm in length appeared to have coherently oriented crystals. Such maps may prove useful for determining pathways for electronic charge transport in P3HT-containing materials. The technique we have developed, however, is perfectly general, and can be applied to any semicrystalline polymer sample.

Chapter 3

Effect of DIO on the structure of T1 small molecule thin films

3.1 Motivation and Overview

The structure and morphology of any functional material can be directly correlated with its properties, including organic solids such as polymers and metal organic frameworks[119, 120, 121]. However, direct imaging using conventional electron microscopy methods to study structural ordering at the level of individual defects and nanoscale domains is not routine for organic solids or other soft materials in the same manner as it is for inorganic or hard materials such as metals and ceramics. This difficulty is typically due to the complex (and often hierarchical) internal structure in thin-films and the inherent sensitivity to electron beam induced damage in soft materials. Thus, new and more robust methods for systematically investigating structure are necessary. Towards this end, we demonstrate the 4D Scanning Electron Transmission Microscopy (4DSTEM) technique for the controlled, systematic, and facile investigation of nano-scale order in a hierarchical, organized soft matter system. As their electronic properties depend highly on their crystallographic geometry, organic semiconductors exemplify the need for improved understanding of the link between structural and functional properties in solid thin-films across a multitude of length-scales ideally suited for study by electron microscopy methods. The low cost, low weight, flexibility, and manufacturability of polymers and organic molecular solids make them attractive materials for applications in photovoltaics[122, 123, 124], integrated circuits[125], light-emitting devices[126], bioelectronics, and thermoelectrics, as alternatives to conventional metals and semiconductors. In well-performing organic semiconductors, the molecular structure and processing must both be extensively optimized for a particular application. Intramolecular electronic transport is typically facile along the conjugated backbone of a molecular or polymeric system, while intermolecular interactions allow charge to couple across larger scales[127, 128, 61, 129]. It follows that the geometry and configuration of the molecules relative to one another dictate the charge transfer pathways, and understanding how low-dimensional and

highly anisotropic semiconductors can form well-connected and robust morphologies remains a great challenge in the manipulation and creation of new topologies and realization of increasingly efficient charge-transport in soft materials. In this study, we have characterized the nanostructure and defects of a small molecule, 7,7'- (4,4 - bis(2 - ethylhexyl) - 4H - silolo[3,2-b:4, 5-b'] dithiophene - 2,6 - diyl) bis(6 - fluoro - 4 - (5'- hexyl[2,2'- bithiophen] - 5 - yl)benzo[c][1,2,5] - thiadiazole)[130], classically abbreviated as p-DTS(FBTTh$_2$)$_2$ in literature, and in this paper denoted as T1, under two different processing conditions using 4DSTEM. Our results demonstrate the ability to characterize the structure of soft materials with nanometer resolution using electron microscopy, and show how the arrangement of nanoscale domains and their coupling from nano-scale to mesoscale can be directly visualized for these types of materials systems.

3.2 Experimental Methods

Sample preparation and microscopy

After dissolution of the T1 molecule in chlorobenzene, a 0.4% DIO solution was added to one of the samples before both were drop-cast onto a lacey carbon Cu TEM grid. The nanodiffraction datasets were collected using a Gatan Orius CCD on a FEI TitanX microscope at 300 kV operated in STEM mode with a small convergence semi-angle of 0.48 mrad and a camera length of 380mm. The probe size was measured to be 2.0 nm at full-width half-max. Since the undiffracted central spot was needed for realignment of the diffraction patterns, and to avoid masking any diffraction spots, no beam stop was used. The spots on the diffraction patterns are large in part due to the parallel nature of the beam, and average about 24 pixels in diameter on the detector. Having large but non-overlapping spots on the diffraction pattern presents an advantage when performing template matching, as the locations of the spots can be determined quite robustly. The samples were cooled with liquid N_2 in order to mitigate beam damage to the long-range order during data collection. Because beam exposure of an area destroys its crystallinity, locations for data collection were determined semi-blindly. The sample was surveyed in STEM diffraction mode until a place with strong lattice reflection spots was found, at which point the beam was blanked. The goniometer was then moved by a few microns away from the damaged area, and the 4DSTEM acquisition launched immediately after un-blanking the beam. Diffraction patterns were obtained at an empirically determined minimum step size of 10 nm over an area of 128 by 128 pixels, with an acquisition time of 33 ms. These parameters were empirically determined to provide the best signal-to-noise ratio on the diffraction patterns. Longer exposure times led to a destruction of sample crystallinity; exposure times were also limited by the speed of the Orius camera. Shorter step sizes led the beam to prematurely damage areas that had yet to be sampled; even though the probe size at full-width half-max was smaller than the 10 nm step size, the damage incurred by the secondary electrons as they percolate laterally through the sample and cause damage ahead of the probe put a limit to how close the probe locations could be

without seeing the diffraction spots disappear.

The dose or fluence (in e/Å^2) that the sample receives can be estimated by two approaches:

1. Calculate the average fluence over the entire scanned area and

2. Calculate the fluence as if all of the beam current is spread over an area defined by the FWHM of the probe.

Using the first method, a beam current of 5 pA with a step size of 10 nm and an exposure of 33 ms translates into an average fluence of about 100 e/Å^2 for the nanobeam diffraction experiment in this work. A typical HAADF-STEM image of 50 pA, 12 μs dwell time and 2 Å pixel size corresponds to a fluence of about 1000 e/Å^2. As compared with one STEM image, the nanobeam diffraction exposes the sample to an order of magnitude less fluence. Using the second method, a beam current of 5 pA covering the area of a circle of 2 nm (FWHM of probe) with an exposure of 33 ms translates into a fluence of about $3{\cdot}10^3$ e/Å^2 as compared with the fluence of a typical HAADF-STEM image of about 500 e/Å^2.

Data processing and analysis

The 4D-STEM data collected was processed in Matlab in order to extract the diffraction spot positions at every pixel. Since the beam tilts in order to raster the sample, the projected diffraction patterns obtained from different locations are not aligned to one another on the detector and need to be realigned to a common center after acquisition. This was accomplished with sub-pixel precision using a discrete Fourier transform method[131] and the bright central transmitted beam as a reference. The strong scattered signal from amorphous elements (lacey carbon and amorphous and/or damaged parts of the film) created a relatively strong background halo at the characteristic lattice spacing of interest and thus obscured or washed out the diffraction spots. Since this effect was not uniform throughout the sample, the background had to be subtracted for each of the DPs individually, using an averaged halo image weighted according to the mean amorphous background intensity of each DP as the subtracted reference. The patterns are thresholded such that small signal areas (<10 pixels) are removed; these correspond to particularly intense noise that could provide false positives in the template matching if their curvature matches particularly well with that of the disk template, but are too small to represent a distinguishable diffraction spot. Since all of the diffraction disks are of the same size to within a pixel, each reflection is found using a phase correlation technique to locate places on the diffraction pattern, I, that match an artificially generated template of a disk of the same diameter, I_{ref}, as the average diffraction spot, using

$$P\left(K_x, K_y\right) = \mathfrak{F}^{-1}\left\{\frac{\mathfrak{F}\left\{I(K_x, K_y)\right\} \circ \mathfrak{F}\left\{I_{\mathrm{ref}}(K_x, K_y)\right\}^*}{\left|\mathfrak{F}\left\{I(K_x, K_y)\right\} \circ \mathfrak{F}\left\{I_{\mathrm{ref}}(K_x, K_y)\right\}^*\right|}\right\}, \tag{3.1}$$

where high values of $P\left(K_x, K_y\right)$ represent locations on the DP where the template and the image match well. Due to the nature of phase correlation, spots are matched to the template

preferentially based on shape, which in this case is the radius of curvature of the diffraction spot. This makes this method robust in the case of incomplete, intensity variable, and noisy diffraction spots. Since the characteristic lattice constant of interest is known, peaks are only looked for at a close distance to that radius. Lattice reflections at other characteristic lattice spacings, probably due to some small amount of contamination, were ignored as they were rare, persisted through only a few adjacent DPS, and more importantly were uncorrelated to the reflections of interest and did not match any of the lattice spacings expected from the material. For the T1 sample (no DIO addition), a single DP would exhibit several diffraction spots "smeared" along an arc, characteristic of a sampling of a continuously varying field of orientations; in that case, the peak closest to the center of mass of the "arc" was chosen for the 2D mapping.

Trace flow visualizations were made by propagating lines across the field of view. At each real space position r_1 a seed for every found orientation θ_1 is initiated and a line propagated to its adjoining pixel r_2, wherein it takes on the orientation θ_2 of the orientation closest to θ_1. The line is stopped if no close orientations are found. This method leads to an unequal line density, which necessitates a selection process that erases lines that are too close together for visualization purposes.

The autocorrelation maps $C(\Delta r, \Delta\theta)$ were computed on a 3D representation of the dataset according to the normalized expression

$$C(\Delta r, \Delta\theta) = \frac{\langle I(r,\theta) I(r+\Delta r, \theta+\Delta\theta)\rangle_{r,\theta} - \langle I(r,\theta)\rangle^2_{r,\theta}}{\langle I(r,\theta)\rangle^2_{r,\theta}} \tag{3.2}$$

At each coordinate r of real space, the θ dimension was populated by placing a Gaussian peak at all θ values where a diffraction spot was found for that location. The heights of the peaks were normalized to the intensity of their respective spot signals, and its width was set to that of a diffraction spot. The characteristic features expected are illustrated in Fig. 3.1, where the cross-correlation analysis is applied on an increasingly blurred artificial dataset. Notably, a field of discrete grains generates "echoes" where the cross-correlation looks far enough away to find grains of same orientation.

3.3 Results

The small molecule under consideration (3.2b) is a well-studied and well-performing electron donor typically used in conjunction with an acceptor molecule, such as [6,6]-phenyl-C_{70}-butyric acid methyl ester[97] (PC70BM) in bulk heterojunction materials with reported efficiencies above 10%[61, 132]. The material is known to undergo a lyotropic phase transition during the spin casting process that remains kinetically trapped in the thin film[133]. Polarization-dependent photoconductive AFM was able to map and estimate the local orientational order at a resolution of about 15 nm and complementary dark field TEM experiments confirmed the presence of a liquid crystalline phase at an even coarser resolution[97]. However, due to the intrinsic and practical limitations of both methods, little is known about the

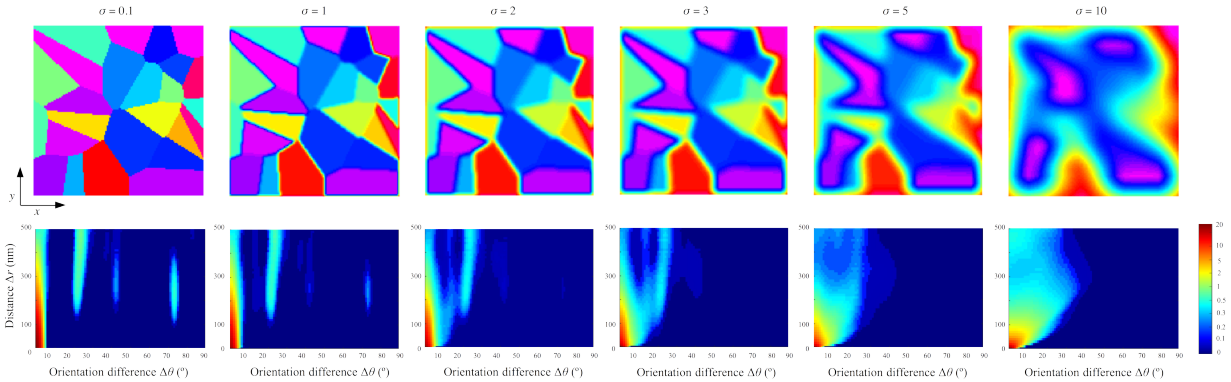

Figure 3.1: Illustration of the evolution of the autocorrelation map as an artificially constructed microstructure evolves from sharp, distinct grains to a smoothly varying orientation field. The transition is done by applying a Gaussian filter with standard deviation σ; dataset size was chosen to match the size of the data gathered for T1 and T1+DIO.

structure on the nanometer scale such as the morphology, size, and mutual arrangement of the crystalline domains. When the samples are processed using a small concentration of the co-solvent 1,8-diiodooctane (DIO), the morphology and functional properties are significantly changed. In the poly(3-hexyl-thiophene-2,5-diyl) conducting polymer system it has been observed that the addition of DIO solvent affects a number of morphological and electronic characteristics of the polymer film[134]. Samples treated with certain concentrations of DIO have shown a decreased viscosity and surface roughness under atomic force microscopy[135], and its addition appears to contribute to a more compact packing of the donor and acceptor phases and an overall more homogeneous film morphology[136]. When DIO was added to a blend of T1 and PC70BM, a maximum photocurrent efficiency (PCE) was found for 0.4% DIO; increasing the concentration degraded the PCE performance[137], as the addition of PC70BM in large quantities appears to disrupt the crystallinity of T1. Most recently Brown et al. reported that the addition of DIO to a similar donor small molecule converts the normally in-plane direction of the backbone to a to a 50:50 in-plane:out-of-plane orientation of the backbone[138]. However, the nature and extent of any morphological changes have yet to be explored at high resolution.

Two samples of the T1 molecule, one with DIO treatment (T1+DIO) and one without, were blade-coated and imaged using the 4DSTEM technique, shown schematically in 3.2a. The fragile nature of the samples' crystallinity under the electron beam presents a significant challenge, as did the relatively weak diffraction from the ordered domains. In order to reduce beam damage, the samples were cooled with liquid nitrogen and the acquisition parameters were empirically tuned to obtain the best diffraction signal possible; a step size of 10 nm was found to be the limit below which the beam started damaging the crystallinity of regions it had yet to sample, providing the spatial resolution limit for any image resulting from the data. A representative sampling of the diffraction patterns (DPs) obtained are shown in

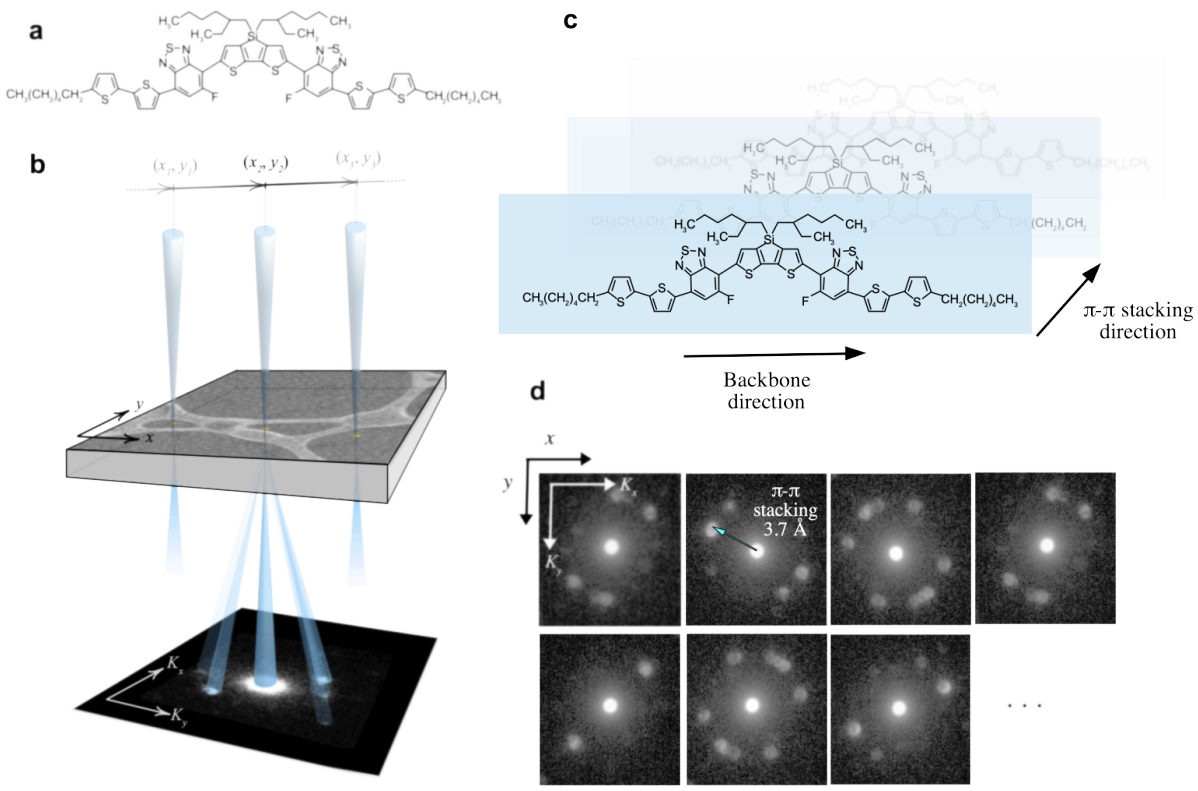

Figure 3.2: Schematic of the 4D-STEM technique (a) and molecular structure of the T1 molecule (b). As the convergent beam rasters over the area of interest, a full diffraction pattern is acquired for each real space probe location (x, y), with a step size large enough to prevent the beam from damaging the yet unsampled neighboring positions. The molecules stack along their π-π bonds as illustrated in (c). The data structure resulting from the technique is shown in (d), with examples of diffraction patterns obtained from T1 + DIO. The π-π stacking characteristic distance of the molecules is indexed on one of the DPs.

3.2c. Due to the high degree of crystallographic texture oriented for diffraction, almost every single probe location exhibited at least one diffraction spot pair corresponding to an in-plane about 3.7 Å π-π spacing of the T1 molecule. It is noteworthy that the 4DSTEM experiment is fast and straightforward making its application to other soft materials accessible.

Figure 3.3 shows how the 4DSTEM can extract previously unseen structural information about the small molecule thin film. The traditional high angle annular dark field (HAADF) images acquired during a standard capture (square images in Figures 2a and b) provide effectively no information about the film's structure. Likewise, virtual dark field reconstructions measuring the brightness of the amorphous halo (rectangular images in 3.3a and b) do not provide any information that can be directly related to the properties of the material. In contrast, the 4DSTEM technique can reveal the underlying structure of the small molecule

films by assigning every pixel of a raster scan to a specific in-plane crystal orientation or distribution of crystal orientations[139]. Mapping the angle of orientation of the brightest diffraction spot pair for each probe location reveals the impact of DIO on the morphology of the polymer. The sample left to dry without DIO exhibits a structure akin to that of liquid crystals[140], with ordered domains smoothly twisting over the whole 180° range and over length scales of about 100 nm, with some shorter-range roughness on the scale of tens of nm (Fig 3.3c). Of note are the topological defects that can be visualized (two of opposite sign are indicated with arrows). These singularities represent defect structures called disclinations, which have been extensively modeled[141, 142], and previously observed for this system[97].

By contrast, the sample treated with DIO shows a sharply segmented grain structure, with clearly defined grain boundaries and identifiable domains of closely similar orientations that extend over hundreds of nm, as seen in Figure 2d. While there is still an approximate 5 to 10° internal fluctuation in orientation within the grains due to the flexible nature of the molecule, the crystalline domains are now very clearly defined. Low-angle grain boundaries and small angular fluctuations are postulated to maintain electronic coupling between neighboring domains better than random orientations. The DPs for this sample also exhibit several distinct lattice reflections at certain probe locations that persist over dozens of real space positions, providing demonstrative evidence that distinct crystalline domains overlap through the film thickness of this sample on the sample size of the probe. While it is not possible to determine the order of the grains along the beam direction (through the thickness of the film), the line plots presented in Figure 3.3e and f, visualized using flow line methods (often seen in fluid dynamics measurements)[143], allows us to visualize the molecular chains and understand the continuity of the structure, as each lattice reflection found at (x, y) is represented by a line colored and oriented according to its lattice orientation angle θ. The lines in these drawings are oriented perpendicular to their reciprocal space reflections and align with what is believed to be the molecular long axis in real space. While the density of the lines is not indicative of the lattice spacing, their orientation and extent are a direct illustration of the local orientation of the lattice planes, also called the director field.

In the T1+DIO sample, many overlapping domains are visible. Most domains tend to be elongated along a direction close to the molecular backbone axis, which is consistent with prior bright field TEM observations of similar annealed or DIO-treated conducting polymer systems[144]. Most of the larger domains had a longer axial dimension on the order of micrometers, and a shorter axial dimension of 100 - 400 nm. Topological singularities were not observed in this sample, but small backbone rotations were observed inside some of the grains (usually $<13°$). The domains had a slight preferred orientation, but domains stacked along the beam direction did not appear to have any simple crystallographic orientation relationship.

The morphological differences are further emphasized in the autocorrelation study shown in Figure 3.4. By correlating the lattice orientations at each probe location to those of all other probe locations, a map of the probability of finding the same orientation at a distance and a misorientation is computed according to eq. 3.2, where $\langle I(r,\theta)\rangle^2_{r,\theta}$ represents

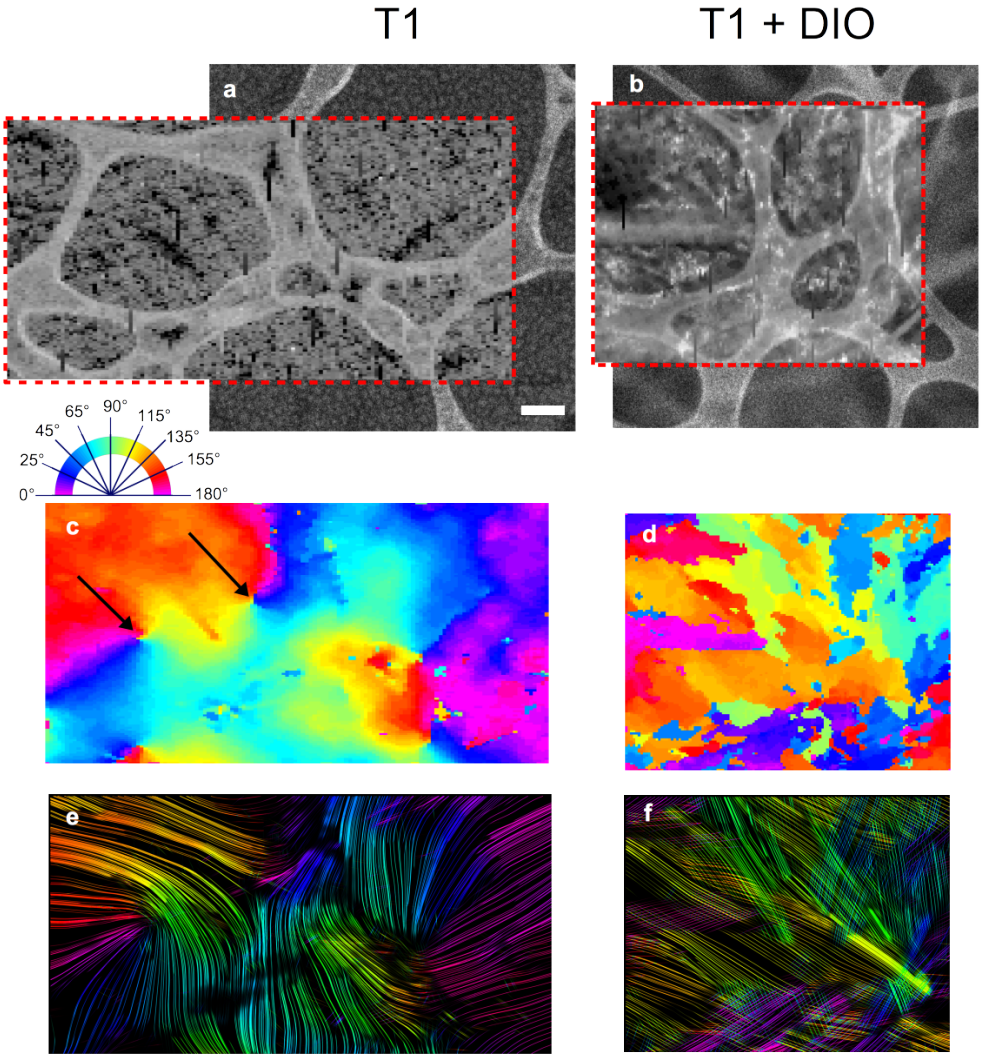

Figure 3.3: Comparison of morphology between samples drop cast with DIO (a, c, e) and without DIO (b, d, f). (a,b) Background HAADF. Dotted lines show area of 4D-STEM scan. A virtual dark field of the scattered amorphous signal reconstructed from the DPs is overlaid onto the HAADF. The angle maps (c, d) show the orientation of the brightest reflection found on the DP at that location. Black arrows in c) indicate disclination discontinuities. Flow maps (e, f) show the continuity of lattice orientations in space. Scale bar is 200 nm.

a normalization factor equivalent to a completely random distribution of lattice orientations in real space. The value of therefore indicates the correlation between probe locations, with observation probability units relative to a random distribution of orientations.

The T1 sample shows a smooth transition in both r and θ, with rotating almost linearly with distance. In contrast, the T1+DIO shows a sharp drop-off around 13°, indicating

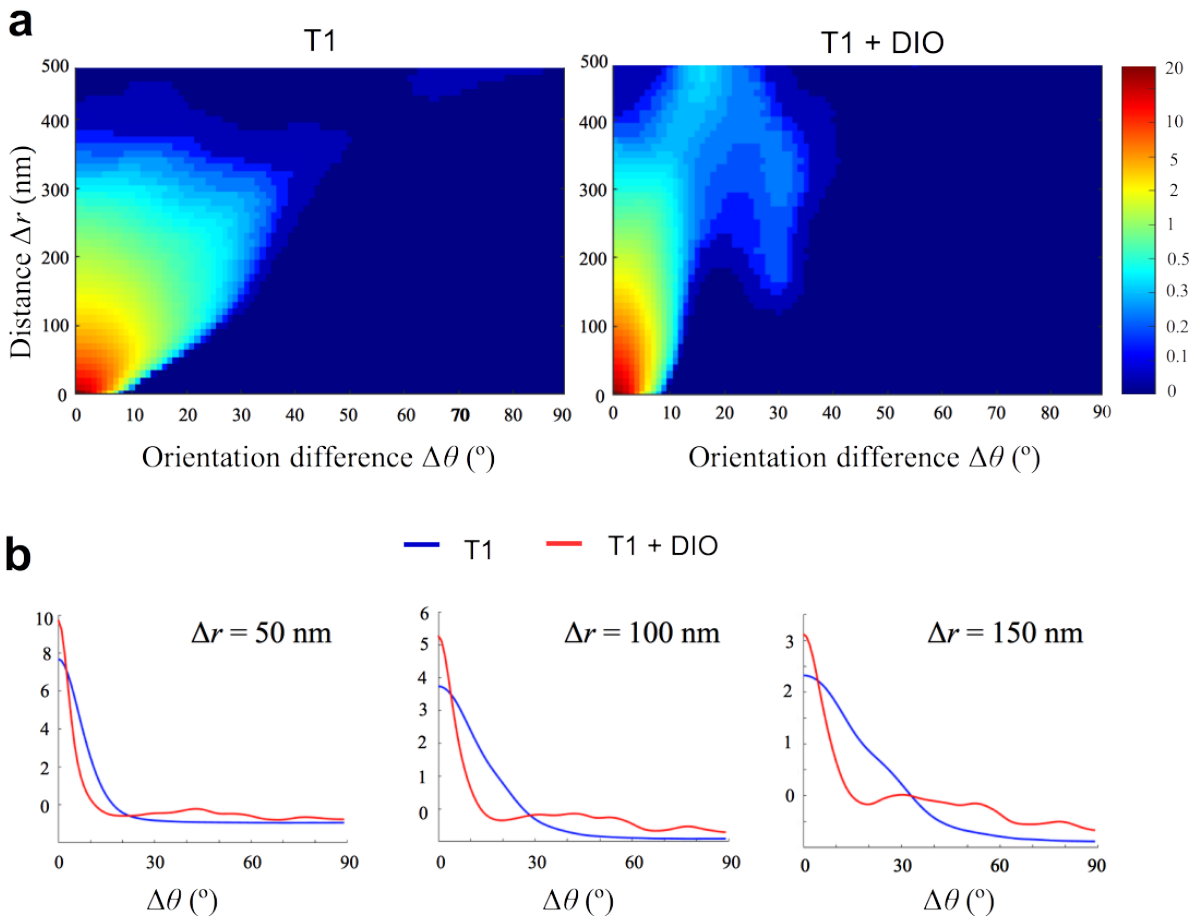

Figure 3.4: Autocorrelation results in a) show the spatial and angular relationship between a probe location at r with an orientation θ to one Δr nanometers away with an orientation $\theta + \Delta\theta$. Overlaid slices for both samples are shown in b) for three values for Δr, clearly demonstrating the increasing divergence between the two as Δr increases.

that misorientations within any single grain do not exceed that value. The secondary maximum feature seen on the T1+DIO map at approximately 30° relative orientation comes from the correlation reaching neighboring grains. There is therefore a preferred orientation of neighboring grains, tending towards smaller misorientations. The secondary maximum is not present at a distance <100 nm, indicating that overlapping grains do not have a visible relative orientation presence. However, we note that more observations are required to draw stronger conclusions about the local orientation. The difference between the two morphologies suggests that the addition of the DIO lowers the energy of the film, allowing grains to nucleate and grow - a process usually achieved through annealing[145]. The strong bends seen in the untreated sample's lattice is the result of a kinetically locked pseudo-phase, and is consistent with the observation that films without DIO dry much faster than ones with DIO[146, 147].

3.4 Conclusion

We have successfully resolved and mapped the local crystalline nanostructure of two T1 organic small molecule systems, one with and one without the solvent DIO, through a new STEM nanodiffraction technique. Exposure to DIO during casting dramatically alters the nanostructure of the resulting material, moving from a smectic liquid crystal-like, continuous, smoothly twisting film to a partially segmented, overlapping discrete grain structure. The grain boundaries and crystalline morphologies of both systems have been analyzed through automated algorithms in order to gain insight into the differences between the two structures and to relate the structure to the kinetic and energetic pathways of formation. The facile nature of the technique, as well as its ability to be applied to any semicrystalline or ordered organic materials, facilitates measurement and comparison of phase morphology in these soft materials at a spatial resolution not previously possible.

Chapter 4

Effect of Annealing on PBTTT liquid crystal structure

4.1 Motivation

The polymer Poly[2,5-bis(3-tetradecylthiophen-2-yl)thieno[3,2-*b*]thiophene][148], abbreviated as PBTTT, is a very popular organic conducting polymer. It is usually doped with Phenyl-C61-Butyric-Acid-Methyl-Ester ((60)PCBM)[149] to form an n-type semiconductor. The efficiencies of this pairing have been shown to be competitively high and its microstructure has been at the focus of a wide body of research[150, 151, 152, 153]. The polymer has a crystalline structure that has been well-characterized through computational modeling [148], atomic force microscopy[154, 155] as well as X-ray studies[156, 157, 151]. The long backbone chains are relatively straight, which allows them to align into ordered rows as their regularly spaced side chains interdigitate. This is facilitated by the flexibility of the backbones, which can accommodate a fair amount of bending and fold on themselves multiple times to create the crystalline domains. A higher crystalline character leads to better electron conductivities[154] – the backbones' π-π bonds come into alignment with one another and the electrons become better delocalized throughout the structure. With a majority of polymer systems, however, pure crystallinity is not realistically achievable, and well-defined, ordered domains are linked by amorphous regions of disordered chains. In the case of PBTTT as well as a few other molecules [158, 159, 160], a nematic liquid crystal-like phase has been observed through X-ray techniques[151], where the crystalline domains vary continuously in orientation and blend into one another. The characteristic distance of PBTTT's π-π stacking, reported to be 3.78 to 3.80 Å depending on the doping concentration and computational parameters[148], shows clear Bragg diffraction and can therefore be used to characterize the crystallinity of the polymer system – making it an ideal candidate for a higher resolution investigation of morphology through electron microscopy.

When compared to other conducting polymer systems, the intrinsic calculated electron mobility of single-crystal PBTTT is lower than that of P3HT; this result, however, is contrary

to empirical measurements when it comes to semi-crystalline films. This means that the electron transport is mitigated by mechanisms other than just electron percolation through the π-π stacks. Of particular interest is the spatial extent of and interconnection between the separate ordered domains; indeed, even if charge conduction is very efficient within a particular crystallite, transfer of charge from one crystallite to another can become a serious bottleneck and greatly impede device efficiency. This is also supported by the observation that high molecular weight polymers show better charge mobility due to the inter-domain connections provided by longer chains[161]. This is why investigations into pathways of crystal domain control is of prime relevance to improving the efficiencies of devices that use polymeric conductors.

There are two main methods by which crystallization in polymers is influenced: solvent addition and annealing. Both play on the thermodynamics and kinetics of crystallization by allowing the structure time and opportunity to evolve into the energetically preferable ordered state, or preventing it from doing so[148]. Annealing in particular is routinely used to increase device performance in many conducting polymer systems, and its effect on bulk efficiency is now well-documented [154], with marked improvements shown even by such aggressive thermal treatments as melting and re-crystallization of the material. AFM studies consistently show a smoothing of the film surface with annealing, and molecular dynamics simulations predict a better interdigitation of the side chains. We wish to build on these results by mapping the crystalline domains directly using electron nanodiffraction – showing for the first time the crystalline orientations of the ordered domains of PBTTT thin films and characterizing their morphology change with annealing.

4.2 Methods

The samples were prepared through spin-casting. Silicon substrates with 200 nm thermal oxide were cleaned by sonicating in acetone, methanol and isopropanol for 15 minutes each. The substrates were then treated with an octyltrichlorosilane self-assembled monolayer after a 20 minute UV-Ozone exposure. Films of PBTTT (Mn = 19 kDa, PDI = 1.3) were spin cast from a 2 mg/mL solution in chlorobenzene. The solution was heated to 80°C. The films were then spun at 800 rpm for 1 minute. Annealed films were heated for 2 hours at 180°C, then cooled on a steel heat sink. Spin coating and annealing were performed in a nitrogen glovebox (O2 $<$ 1ppm). Films were transferred onto ultrathin carbon/lacy carbon TEM grids (Ted Pella # 01824) via lift-off in dilute hydrogen fluoride.

4DSTEM datasets were collected on the TITAN X microscope cooled by liquid N_2. All subsequent analysis was performed in Matlab; see appendix for code details.

Several datasets were acquired of the non-annealed, as cast samples; the chosen dataset is denoted as C1. Two datasets were acquired of the annealed samples, referred to as A1 and A2. All datasets span 128x128 probe positions and were taken at 33 ms exposure time, with a 300 kV beam. The fragility of the polymer under the electron beam necessitated a

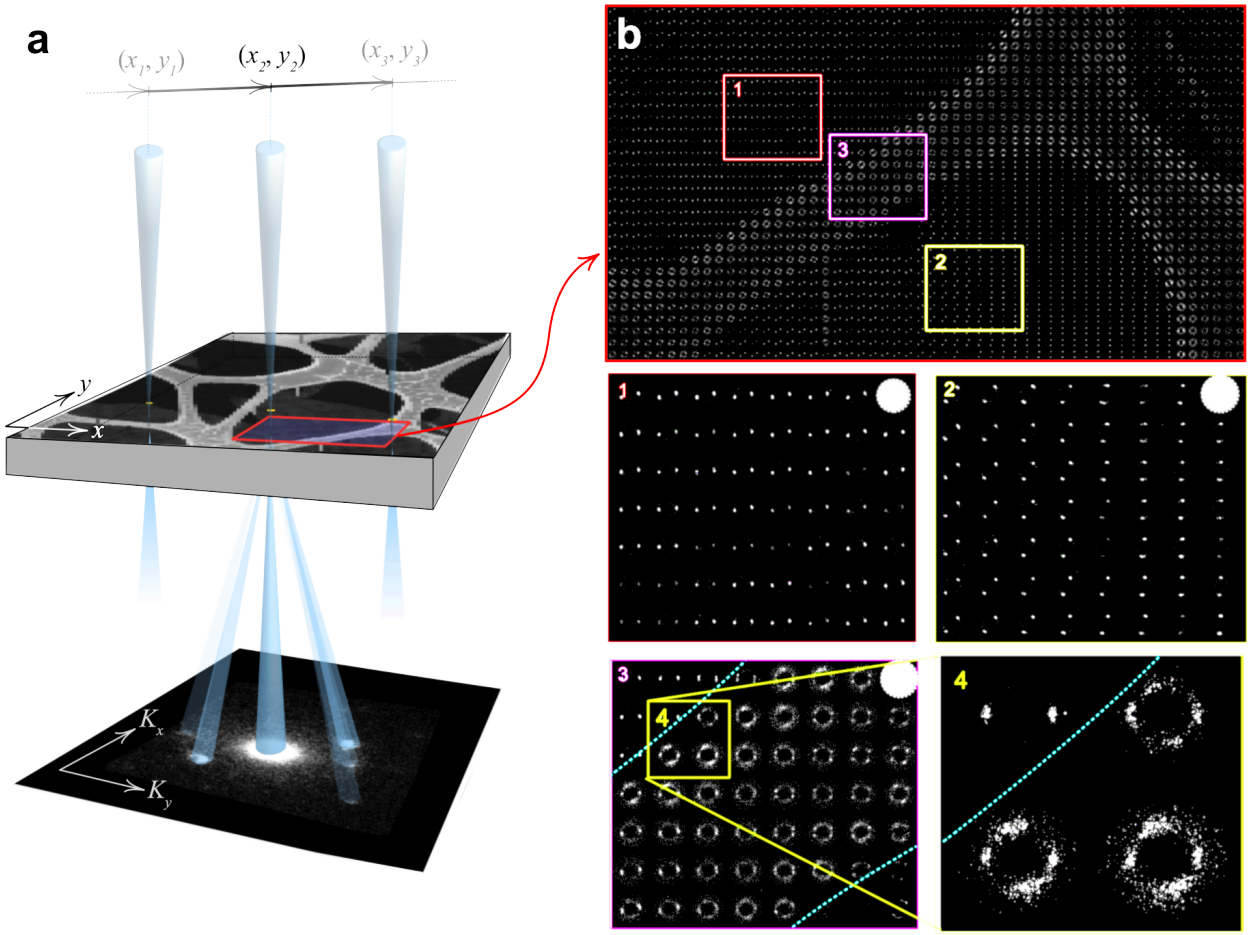

Figure 4.1: Visualization of dataset A1 at different scales. a) Schematic of the 4DSTEM acquisition technique, showing the dark field reconstruction. The area outlined on the dark field view is shown in b), where real space is tiled with post-processed diffraction patterns. Swatches show areas of relatively constant orientation (A), places where the amorphous halo overtakes the signal and it becomes difficult to differentiate between diffraction from the thick carbon edge and diffraction from the thin film (B), and areas of smooth, gradual rotation (C). The extent of a full diffraction pattern is delineated in the upper left corner of each swatch for reference.

large spot size (11) on the Titan system and short acquisition times to mitigate damage to the polymer.

The datasets acquired have been realigned to a common center and the scattered halo iteratively subtracted from each DP. The scattered signal from the amorphous lacey carbon support is very strong, and distinct diffraction spots in the thicker regions are visible.

Since the characteristic spacings for the PBTTT reflections and those of the scattered amorphous ring match, diffraction spots from regions lying on thicker regions of lacey carbon

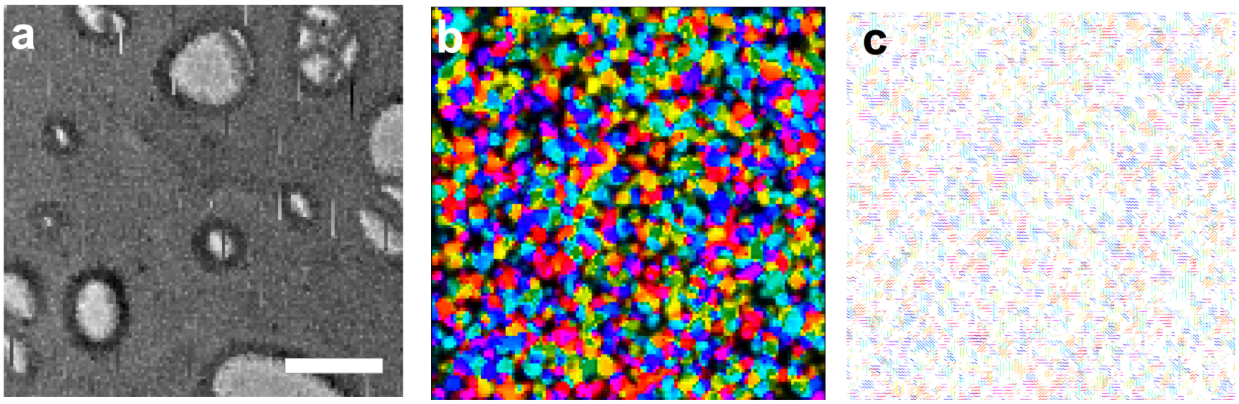

Figure 4.2: Virtual dark field reconstruction (a), angle orientation map (b), and like orientation visualization (c) of the as cast sample C1. Scale bar is 300 nm.

often find themselves obscured by the very bright scattered halo and washed away. Therefore, in order to obtain a clean dataset, the scattered halo needed to be modeled and removed.

In order to ensure that the only subtracted signal is that of the scattered amorphous background, a Gaussian is fitted to the amorphous halo. Even though its shape is not an ideal Gaussian, the area of interest – that is, in the vicinity of the PBTTT reflection radius – can be fitted to a Gaussian quite well from an average of all diffraction patterns. This synthetic 2D Gaussian becomes the halo template that is subtracted from each DP; in turn, each subtraction is weighed according to that DP's relative brightness, since the scattered halo varies greatly in intensity from pattern to pattern. This allows for a more robust finding of the relevant diffraction peaks, and is more accurate than a simple average of all DPs. A 2D Gaussian fit also allows to match the astigmatism of the dataset, which makes it a valid virtual alternative to the average DP.

The subtraction allows for a better, more accurate spot finding. The template of the "ideal diffraction peak" is an average composite of the central transmitted beam images from all DPs. Since the beam is not necessarily symmetrical, each diffraction spot – including the central one – will contain the same irregularities and aberrations, and thus locating the diffraction spots is more robust when the template is more reflective of the actual spot shape.

The diffraction spots were then found and their orientations extracted through phase correlation. Line plots were generated by seeding and propagating orientations through neighboring pixels, as long as there are orientations to be found within 5 degrees of the seed.

4.3 Results

Fig. 4.1b shows a subset of the A2 dataset plotted with each pixel in real space represented by its full diffraction pattern. Due to the large size of the dataset – each real space pixel is represented by a 512x512 pixel image – it is not practical to show the entire plot. The central

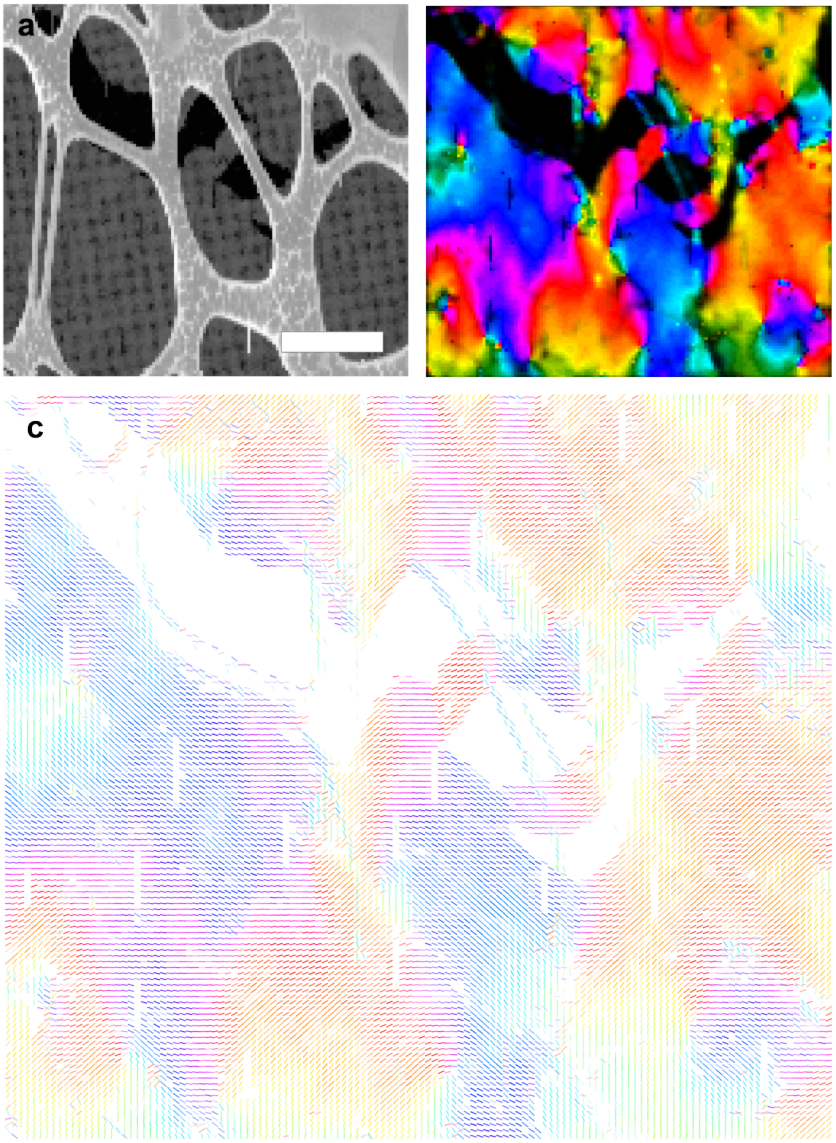

Figure 4.3: Orientation maps of the A1, annealed PBTTT sample. (a) Dark field reconstruction. (b) Angle orientation map. (c) Orientation line plotted for each DP, with slope matched to the angle of the diffraction spots. Scale bar is 300 nm.

beam having been erased and the amorphous scattered halo suppressed, the symmetrical pairs of diffraction spots become apparent on the image.

The results from the peak search and line flow trace for the as cast and annealed samples are shown in Fig. 4.2, 4.3, 4.4, and 4.5. The virtual dark field reconstruction, taken as the intensity integral over the entire diffraction pattern, is shown for all samples as a reference. The structure of the lacey carbon, as well as the extent of the film and its imperfections can

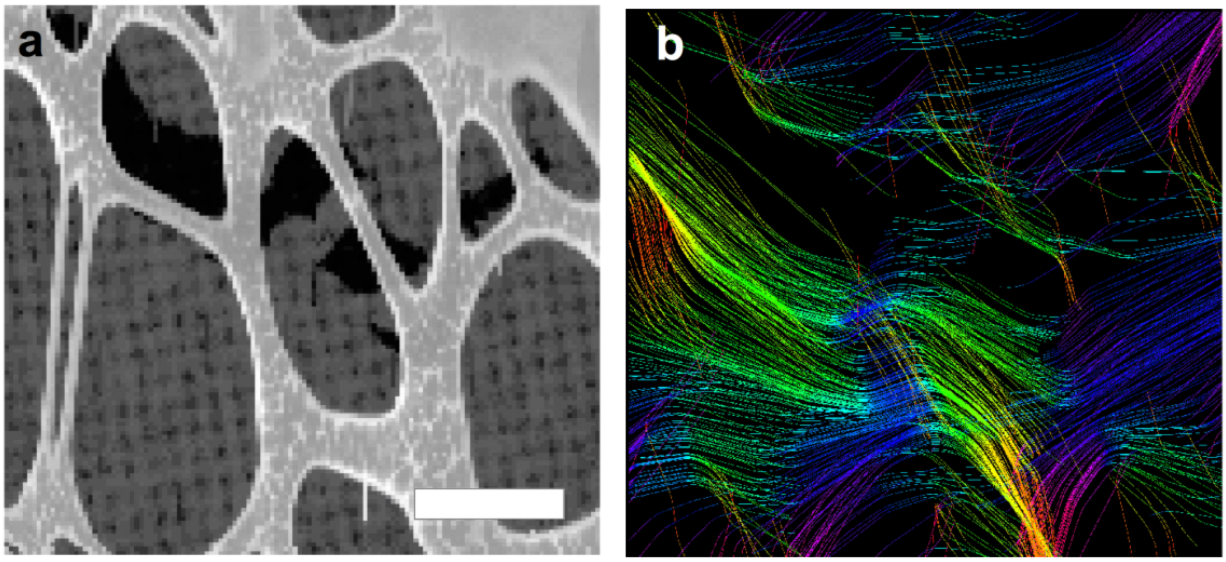

Figure 4.4: Virtual dark field reconstruction (a) and line flow visualization (b) of the annealed sample C11. Scale bar is 300 nm.

be clearly seen in all cases.

When looking at the as cast sample, the crystalline topology shows many small, discrete grains of a given orientation (Fig. 4.2b and c). The film is laying uniformly on the lacey carbon and the grain orientation or distribution is not related to its topology. The crystallites are well-dispersed and of very uniform size, from 50 to 100 nm in diameter, and overall disc-shaped; since this is a 2D projection, their extent in the z-direction is not determined. The line plot map in Fig.4.3c, where a line is plotted at each real space position with slope and color corresponding to lattice orientation at that position, shows that individual grains do overlap. In general, the diffraction spots in this sample are significantly sharper and well-defined than in the annealed case, so much so that second-order reflections are also present. In comparison, the annealed sample shows fainter, more diffuse peaks; furthermore, they tend to be "smeared" over an angular range of several degrees on any distinct diffraction pattern. This is due to the fact that at any probe position, the smooth curving of the lattice planes leads to a sampling of a wider range of Bragg reflection conditions. This result is consistent with previously published AFM data mapping the roughness of the film surface. The crystallite domains are small and do not show ordered interconnectivity; dark regions between the grains are most plausibly regions of disordered chains. In the case of the annealed samples, presented in Fig.4.3 and 4.5, the film is broken in half; locations where there is no film are colored black. Looking closely at the line trace reconstruction from Fig.4.5d, we can see that the film appeared to have broken parallel to the lattice backbones. The lattice orientations propagate across the crack and match across the divide, meaning that the film broke after annealing, once all of the orientations had settled. The film was spin-cast and

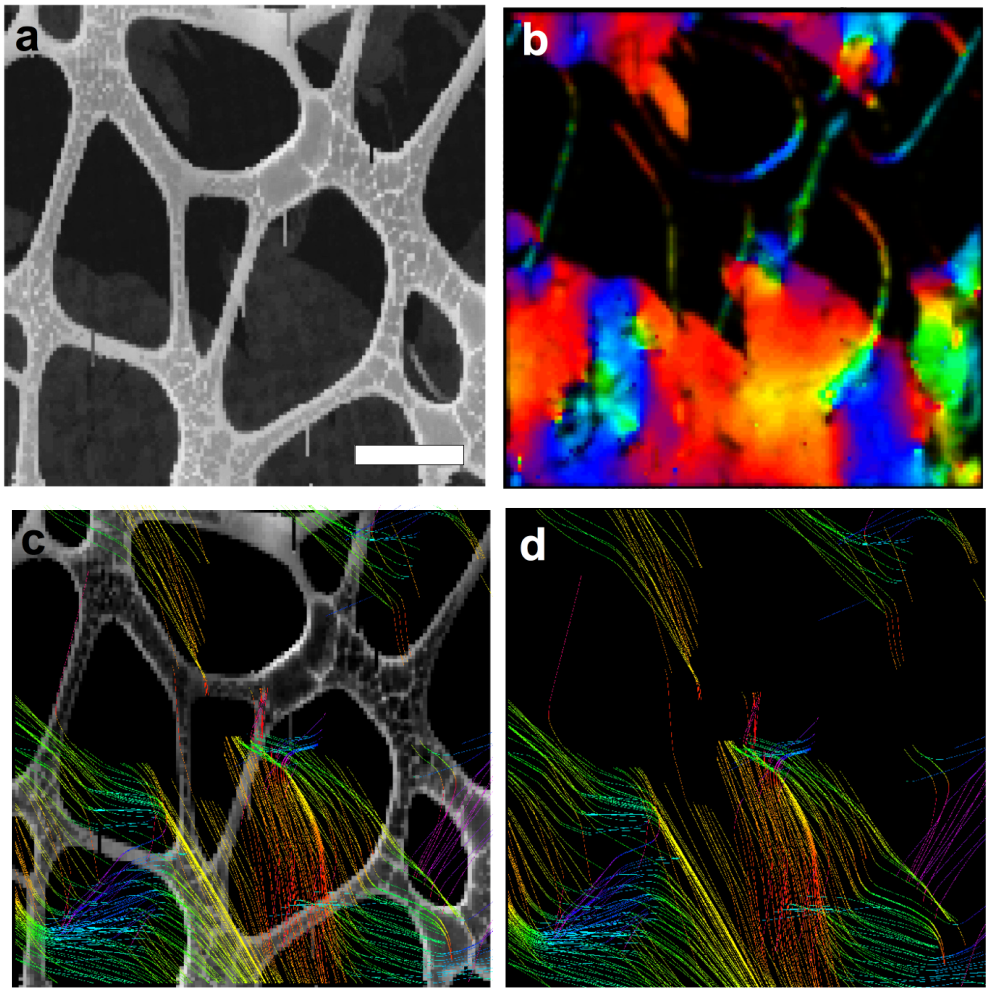

Figure 4.5: Orientation maps of the A1, annealed PBTTT sample. a) The dark field reconstruction shows variation in thickness of the lacey carbon; the film and the break therein are also visible. b) Orientation map colored according to most prominent lattice orientation. c) and d) Line flow visualizations. Scale bar is 300 nm.

annealed on a separate substrate, and then floated onto the copper/carbon grid; it therefore expected that the topology of the polymer crystallinity is not related to that of the lacey carbon.

In the case of the annealed polymer films, we observe a type of liquid-crystal crystalline topography previously seen in the case of the T1 small molecule. The orientations of the diffraction spots vary smoothly and continuously. Pairs of disinclination points, where the lattices turn a full 360° can be seen; previous studies have linked them to defects in the film.

The liquid crystal structure of the annealed sample shows connectivity across the entire film. Furthermore, there no longer seems to be any overlap of the domains through the

thickness of the film, with one contiguous layer responsible for the entirety of the diffraction signal. This result is consistent with previously published AFM data, where smoother surfaces were observed for annealed samples. The annealing process has led the domains to not only merge into one another but also grow; barring the extreme orientation changes in the vicinity of the disclinations, the rate of variation of the chain orientations is considerably lower than the size of the crystallites in the as-cast sample.

This is not the case in the as-cast sample, where the reflections have, for the most part, a distinct edge, which means that the crystallites have a unique, well-defined preferred orientation. This goes to show that the same conducting polymer, PBTTT, can exhibit extremely diverse topographies depending on processing conditions, which would in turn impact its ability to conduct charge. The smoothly varying, contiguous film exhibited by the annealed sample explains very well why annealing is so effective in increasing electronic conductance. Even though the crystallites in the as-cast sample have better orientation homogeneity within each grain, they are not effectively connected to one another and the electrons do not have any reliable pathways to transfer from one crystallite to another. In this research the polymer was not doped with (60)PCBM as it would usually be in an actual conducting device; because of the size and bulky shape of (60)PCBM molecules, the molecular arrangement of the chains would have to be quite different from what we see in the case of pure PBTTT. Nevertheless, doped PBTTT does exhibit crystallinity, and the study of pure PBTTT as it was done here provides a solid base for comparison and further investigations.

These results can be presented on large scales on the order of microns specifically thanks to the method of 4DSTEM. Detailed high-resolution imaged of the polymer have been obtained through scanning tunnelling microscopy, where the structure of the individual polymer chains has been revealed, and the overall crystal structure has been determined with X-Rays. These techniques, however, probe either the very small or the very large scale, but 4DSTEM is able to concatenate both by mapping relatively large areas on the order of a micron, but at a fine resolution on the order of tens of nanometers. Furthermore, the lineflow data plotting allows a visualization of the structure *through* the thickness of the film, providing information that AFM cannot show. This makes the technique very powerful for investigating semi-crystalline polymer structures and their properties.

4.4 Conclusion

In this research, the crystallinity of a PBTTT polymer thin film was characterized through scanning electron nanodiffraction. Annealed PBTTT films were found to exhibit a liquid-crystal type of topology where chain orientations vary smoothly over the field of view. As cast samples, on the other hand, showed small, spherical, uniformly dispersed crystalline domains of distinct orientation.

Chapter 5

Conclusion

In this study, the efficacy of transmission electron microscopy in resolving the local structure of crystalline and semi-crystalline polymer features through diffraction has been shown. While the electron beam is highly damaging to the polymer structures themselves, it is possible to adjust parameters such as operating temperature, beam size, step size, and acquisition time, in order to obtain relevant data. While some structures remain too fragile even for the most conservative settings of the aforementioned parameters, the technique has been applied to a number of promising polymer structures in the field of conducting polymers, wherein crystallinity and local microstructure play a big role in the efficiency of electronic transfer.

All of the systems under consideration are important alternatives to traditional inorganic semiconductors, all the while their internal structure and electronic pathway mechanisms are still not well-understood. Their relatively fragile nature and immense variability in form and assembly make these difficult to fully characterize. This research is thus another step in the effort to understand and map the ways electronic conduction occurs in these materials, with the ultimate goal of shaping these mechanisms and making organic conductors better applicable and more competitive.

In future work, more systems would be characterized through this technique – and this not limited to electronically conducting polymers. If the data acquisition rate and signal to noise ration can be improved, and it looks like with the development and installation of new cameras and detectors on microscopes this might soon be the case, it might be possible to image and reconstruct much larger areas or, conversely, to resolve crystallinity on much smaller scales. The behavior of the polymer chains could be mapped to better precision and accuracy, and in-situ dynamic studies can be envisaged as well. The understanding of the electronic behavior of the polymer films could then be augmented with studies on their mechanical or topological properties. Electronic pathways could be correlated with chain orientation and extent in experiments measuring the conductance of a film while being imaged under the microscope. This new way of looking at polymer crystallinity opens myriad pathways for investigation and research, and has the potential to greatly improve our understanding and manipulation efficacy of conductive polymers.

Bibliography

[1] Hideki Shirakawa et al. "Synthesis of electrically conducting organic polymers: halogen derivatives of polyacetylene,(CH) x." In: *Journal of the Chemical Society, Chemical Communications* 16 (1977), pp. 578–580.

[2] Alan J Heeger. "Semiconducting and metallic polymers: the fourth generation of polymeric materials (Nobel lecture)." In: *Angewandte Chemie International Edition* 40.14 (2001), pp. 2591–2611.

[3] Bernhard Wessling. "From conductive polymers to organic metals." In: *Chemical Innovation(USA)* 31.1 (2001), pp. 34–40.

[4] Lewis Gomez De Arco et al. "Continuous, highly flexible, and transparent graphene films by chemical vapor deposition for organic photovoltaics." In: *ACS nano* 4.5 (2010), pp. 2865–2873.

[5] Maher Al-Ibrahim et al. "Flexible large area polymer solar cells based on poly (3-hexylthiophene)/fullerene." In: *Solar Energy Materials and Solar Cells* 85.1 (2005), pp. 13–20.

[6] Tran Quang Trung and Nae-Eung Lee. "Flexible and Stretchable Physical Sensor Integrated Platforms for Wearable Human-Activity Monitoringand Personal Healthcare." In: *Advanced materials* 28.22 (2016), pp. 4338–4372.

[7] K Norrman, NB Larsen, and Frederik C Krebs. "Lifetimes of organic photovoltaics: combining chemical and physical characterisation techniques to study degradation mechanisms." In: *Solar energy materials and solar cells* 90.17 (2006), pp. 2793–2814.

[8] Frederik C Krebs et al. "Lifetimes of organic photovoltaics: photochemistry, atmosphere effects and barrier layers in ITO-MEHPPV: PCBM-aluminium devices." In: *Solar Energy Materials and Solar Cells* 86.4 (2005), pp. 499–516.

[9] Jens A Hauch et al. "Flexible organic P3HT: PCBM bulk-heterojunction modules with more than 1 year outdoor lifetime." In: *Solar Energy Materials and Solar Cells* 92.7 (2008), pp. 727–731.

[10] Martin A Green et al. "Solar cell efficiency tables (version 37)." In: *Progress in photovoltaics: research and applications* 19.1 (2011), pp. 84–92.

[11] Ching W Tang and Steven A VanSlyke. "Organic electroluminescent diodes." In: *Applied physics letters* 51.12 (1987), pp. 913–915.

[12] JH Burroughes et al. "Light-emitting diodes based on conjugated polymers." In: *nature* 347.6293 (1990), p. 539.

[13] Yixia Zhao et al. "A novel flexible sensor for respiratory monitoring based on in situ polymerization of polypyrrole and polyurethane coating." In: *RSC Advances* 7.78 (2017), pp. 49576–49585.

[14] RV Gregory, WC Kimbrell, and HH Kuhn. "Conductive textiles." In: *Synthetic Metals* 28.1-2 (1989), pp. 823–835.

[15] Toshiaki Ohtsuka. "Corrosion protection of steels by conducting polymer coating." In: *International Journal of Corrosion* 2012 (2012).

[16] Xiaohan Wu et al. "Strategies for Improving the Performance of Sensors Based on Organic Field-Effect Transistors." In: *Advanced Materials* (2018), p. 1705642.

[17] Gilles Horowitz et al. "Organic field-effect transistors." In: *Advanced materials* 10.5 (1998), pp. 365–377.

[18] Christos D Dimitrakopoulos and Patrick RL Malenfant. "Organic thin film transistors for large area electronics." In: *Advanced materials* 14.2 (2002), pp. 99–117.

[19] Hongming Zhang et al. "Aqueous dispersed conducting polyaniline nanofibers: Promising high specific capacity electrode materials for supercapacitor." In: *Journal of Power Sources* 196.23 (2011), pp. 10484–10489.

[20] Lin Xia, Zhixiang Wei, and Meixiang Wan. "Conducting polymer nanostructures and their application in biosensors." In: *Journal of colloid and interface science* 341.1 (2010), pp. 1–11.

[21] Richard Balint, Nigel J Cassidy, and Sarah H Cartmell. "Conductive polymers: towards a smart biomaterial for tissue engineering." In: *Acta biomaterialia* 10.6 (2014), pp. 2341–2353.

[22] Shruti Nambiar and John TW Yeow. "Conductive polymer-based sensors for biomedical applications." In: *Biosensors and Bioelectronics* 26.5 (2011), pp. 1825–1832.

[23] Hua Bai and Gaoquan Shi. "Gas sensors based on conducting polymers." In: *Sensors* 7.3 (2007), pp. 267–307.

[24] Jiri Janata and Mira Josowicz. "Conducting polymers in electronic chemical sensors." In: *Nature materials* 2.1 (2003), p. 19.

[25] Takao Someya et al. "Chemical and physical sensing by organic field-effect transistors and related devices." In: *Advanced Materials* 22.34 (2010), pp. 3799–3811.

[26] MEL Wouters et al. "Transparent UV curable antistatic hybrid coatings on polycarbonate prepared by the sol–gel method." In: *Progress in Organic Coatings* 51.4 (2004), pp. 312–319.

[27] F Jonas and JT Morrison. "3, 4-polyethylenedioxythiophene (PEDT): Conductive coatings technical applications and properties." In: *Synthetic Metals* 85.1-3 (1997), pp. 1397–1398.

[28] Mario Leclerc. "Optical and electrochemical transducers based on functionalized conjugated polymers." In: *Advanced Materials* 11.18 (1999), pp. 1491–1498.

[29] Ross D Jansen-van Vuuren et al. "Organic photodiodes: the future of full color detection and image sensing." In: *Advanced Materials* 28.24 (2016), pp. 4766–4802.

[30] Joel S Miller. "Conducting polymers – materials of commerce." In: *Advanced Materials* 5.9 (1993), pp. 671–676.

[31] Christopher J Traverse et al. "Emergence of highly transparent photovoltaics for distributed applications." In: *Nature Energy* 2.11 (2017), p. 849.

[32] Malenahalli Halappa Naveen, Nanjanagudu Ganesh Gurudatt, and Yoon-Bo Shim. "Applications of conducting polymer composites to electrochemical sensors: A review." In: *Applied Materials Today* 9 (2017), pp. 419–433.

[33] Peng Lin and Feng Yan. "Organic thin-film transistors for chemical and biological sensing." In: *Advanced materials* 24.1 (2012), pp. 34–51.

[34] Serge Cosnier. "Biomolecule immobilization on electrode surfaces by entrapment or attachment to electrochemically polymerized films. A review." In: *Biosensors and Bioelectronics* 14.5 (1999), pp. 443–456.

[35] TF Otero and JM Sansinena. "Bilayer dimensions and movement in artificial muscles." In: *Bioelectrochemistry and bioenergetics* 42.2 (1997), pp. 117–122.

[36] Nathalie K Guimard, Natalia Gomez, and Christine E Schmidt. "Conducting polymers in biomedical engineering." In: *Progress in polymer science* 32.8-9 (2007), pp. 876–921.

[37] Naseer Ahmad and Alan G MacDiarmid. "Inhibition of corrosion of steels with the exploitation of conducting polymers." In: *Synthetic Metals* 78.2 (1996), pp. 103–110.

[38] Geoffrey M Spinks et al. "Electroactive conducting polymers for corrosion control." In: *Journal of Solid State Electrochemistry* 6.2 (2002), pp. 85–100.

[39] Gordon G Wallace, Toni E Campbell, and Peter C Innis. "Putting function into fashion: Organic conducting polymer fibres and textiles." In: *Fibers and Polymers* 8.2 (2007), pp. 135–142.

[40] Mallory L Hammock et al. "25th anniversary article: the evolution of electronic skin (e-skin): a brief history, design considerations, and recent progress." In: *Advanced materials* 25.42 (2013), pp. 5997–6038.

[41] Xiaohan Wu et al. "Thermally Stable, Biocompatible, and Flexible Organic Field-Effect Transistors and Their Application in Temperature Sensing Arrays for Artificial Skin." In: *Advanced Functional Materials* 25.14 (2015), pp. 2138–2146.

[42] Yoseph Bar-Cohen. "Electroactive polymers as artificial muscles: A review." In: *Journal of Spacecraft and Rockets* 39.6 (2002), pp. 822–827.

[43] Mohsen Shahinpoor et al. "Ionic polymer-metal composites (IPMCs) as biomimetic sensors, actuators and artificial muscles-a review." In: *Smart materials and structures* 7.6 (1998), R15.

[44] Karthikeyan Gnanasekaran et al. "3D printing of CNT-and graphene-based conductive polymer nanocomposites by fused deposition modeling." In: *Applied Materials Today* 9 (2017), pp. 21–28.

[45] Xin Wang et al. "3D printing of polymer matrix composites: A review and prospective." In: *Composites Part B: Engineering* 110 (2017), pp. 442–458.

[46] William S Wong and Alberto Salleo. *Flexible electronics: materials and applications*. Vol. 11. Springer Science & Business Media, 2009.

[47] Al C de Leon et al. "High performance polymer nanocomposites for additive manufacturing applications." In: *Reactive and Functional Polymers* 103 (2016), pp. 141–155.

[48] MM Labes, P Love, and LF Nichols. "Polysulfur nitride-a metallic, superconducting polymer." In: *Chemical Reviews* 79.1 (1979), pp. 1–15.

[49] Jean Luc Bredas and G Bryan Street. "Polarons, bipolarons, and solitons in conducting polymers." In: *Accounts of Chemical Research* 18.10 (1985), pp. 309–315.

[50] Leo Mandelkern. *Crystallization of polymers*. Vol. 38. McGraw-Hill New York, 1964.

[51] Artur Rozanski and Andrzej Galeski. "Plastic yielding of semicrystalline polymers affected by amorphous phase." In: *International journal of plasticity* 41 (2013), pp. 14–29.

[52] ES Clark and LS Scott. "Superdrawn crystalline polymers: A new class of high-strength fiber." In: *Polymer Engineering & Science* 14.10 (1974), pp. 682–686.

[53] Andrzej Galeski. "Strength and toughness of crystalline polymer systems." In: *Progress in Polymer Science* 28.12 (2003), pp. 1643–1699.

[54] Rodrigo Noriega et al. "A general relationship between disorder, aggregation and charge transport in conjugated polymers." In: *Nature materials* 12.11 (2013), p. 1038.

[55] Jianguo Mei et al. "Siloxane-terminated solubilizing side chains: bringing conjugated polymer backbones closer and boosting hole mobilities in thin-film transistors." In: *Journal of the American Chemical Society* 133.50 (2011), pp. 20130–20133.

[56] Alessandro Troisi. "Charge dynamics through pi-stacked arrays of conjugated molecules: effect of dynamic disorder in different transport/transfer regimes." In: *Molecular Simulation* 32.9 (2006), pp. 707–716.

[57] Christian G Claessens and J Fraser Stoddart. "π–π Interactions in self-assembly." In: *Journal of Physical Organic Chemistry* 10.5 (1997), pp. 254–272.

[58] Herbert W Roesky and Marius Andruh. "The interplay of coordinative, hydrogen bonding and π–π stacking interactions in sustaining supramolecular solid-state architectures.: A study case of bis (4-pyridyl)-and bis (4-pyridyl-N-oxide) tectons." In: *Coordination chemistry reviews* 236.1-2 (2003), pp. 91–119.

[59] Hasan Karabıyık and N Ocak İskeleli. "Hydrogen-bridged chelate ring-assisted π-stacking interactions." In: *Acta Crystallographica Section B: Structural Science* 68.1 (2012), pp. 71–79.

[60] John M Warman et al. "Charge mobilities in organic semiconducting materials determined by pulse-radiolysis time-resolved microwave conductivity: π-bond-conjugated polymers versus π- π-stacked discotics." In: *Chemistry of materials* 16.23 (2004), pp. 4600–4609.

[61] Henning Sirringhaus et al. "Two-dimensional charge transport in self-organized, high-mobility conjugated polymers." In: *Nature* 401.6754 (1999), p. 685.

[62] Dmytro Dudenko et al. "A Strategy for Revealing the Packing in Semicrystalline Π-Conjugated Polymers: Crystal Structure of Bulk Poly-3-Hexyl-Thiophene (P3HT)." In: *Angewandte Chemie International Edition* 51.44 (2012), pp. 11068–11072.

[63] Yongfeng Men, Jens Rieger, and Gert Strobl. "Role of the entangled amorphous network in tensile deformation of semicrystalline polymers." In: *Physical review letters* 91.9 (2003), p. 095502.

[64] Koji Yazawa et al. "Molecular dynamics of regioregular poly (3-hexylthiophene) investigated by NMR relaxation and an interpretation of temperature dependent optical absorption." In: *The Journal of Physical Chemistry B* 114.3 (2010), pp. 1241–1248.

[65] Brenton AG Hammer et al. "Robust polythiophene nanowires cross-linked with functional fullerenes." In: *Journal of Materials Chemistry C* 2.45 (2014), pp. 9674–9682.

[66] Margaretha Åkerholm, Barbara Hinterstoisser, and Lennart Salmén. "Characterization of the crystalline structure of cellulose using static and dynamic FT-IR spectroscopy." In: *Carbohydrate research* 339.3 (2004), pp. 569–578.

[67] Michael B Clark, Cindy A Burkhardt, and Joseph A Gardella. "Surface studies of polymer blends. 4. An ESCA, IR, and DSC study of the effect of homopolymer molecular weight on crystallinity and miscibility of poly (iε-caprolactone)/poly (vinyl chloride) homopolymer blends." In: *Macromolecules* 24.3 (1991), pp. 799–805.

[68] BH Stuart. "Polymer crystallinity studied using Raman spectroscopy." In: *Vibrational spectroscopy* 10.2 (1996), pp. 79–87.

[69] GR Strobl and W Hagedorn. "Raman spectroscopic method for determining the crystallinity of polyethylene." In: *Journal of Polymer Science: Polymer Physics Edition* 16.7 (1978), pp. 1181–1193.

[70] Roddel Remy et al. "Enthalpy of fusion of poly (3-hexylthiophene) by differential scanning calorimetry." In: *Journal of Polymer Science Part B: Polymer Physics* 52.22 (2014), pp. 1469–1475.

[71] CT Mortimer. "Differential Scanning Calorimetry." In: *Thermochemistry and Its Applications to Chemical and Biochemical Systems*. Springer, 1984, pp. 47–60.

[72] Kok Ho Kent Chan et al. "Unique structural features and electrical properties of electrospun conjugated polymer poly (3-hexylthiophene)(P3HT) fibers." In: *Synthetic Metals* 160.23-24 (2010), pp. 2587–2595.

[73] Soo-Young Park et al. "The crystal structure of poly (2, 6-naphthalenebenzobisthiazole)." In: *Polymer* 46.15 (2005), pp. 5630–5636.

[74] Burak Y Kadem, Mohammed K Al-hashimi, and AK Hassan. "The effect of solution processing on the power conversion efficiency of P3HT-based organic solar cells." In: *Energy Procedia* 50 (2014), pp. 237–245.

[75] James D Watson, Francis HC Crick, et al. "Molecular structure of nucleic acids." In: *Nature* 171.4356 (1953), pp. 737–738.

[76] Jostein Mårdalen et al. "X-ray scattering from oriented poly (3-alkylthiophenes)." In: *Synthetic metals* 48.3 (1992), pp. 363–380.

[77] Kuei-Yu Kao et al. "Gelation of a solution of poly (3-hexylthiophene) greatly retards its crystallization rate in the subsequently cast film." In: *The Journal of Physical Chemistry B* 118.49 (2014), pp. 14510–14518.

[78] J Perlich et al. "Grazing incidence wide angle x-ray scattering at the wiggler beamline BW4 of HASYLAB." In: *Review of Scientific Instruments* 81.10 (2010), p. 105105.

[79] Duc T Duong et al. "The chemical and structural origin of efficient p-type doping in P3HT." In: *Organic Electronics* 14.5 (2013), pp. 1330–1336.

[80] Christian Müller et al. "Crystalline–crystalline poly (3-hexylthiophene)–polyethylene diblock copolymers: Solidification from the melt." In: *Polymer* 49.18 (2008), pp. 3973–3978.

[81] Xinli Xiao et al. "Single crystals of polythiophene with different molecular conformations obtained by tetrahydrofuran vapor annealing and controlling solvent evaporation." In: *The Journal of Physical Chemistry B* 114.22 (2010), pp. 7452–7460.

[82] Bryce Meredig, Alberto Salleo, and Richard Gee. "Ordering of poly (3-hexylthiophene) nanocrystallites on the basis of substrate surface energy." In: *ACS nano* 3.10 (2009), pp. 2881–2886.

[83] Behzad Mohammadi, Ali Akbar Yousefi, and Samad Moemen Bellah. "Effect of tensile strain rate and elongation on crystalline structure and piezoelectric properties of PVDF thin films." In: *Polymer testing* 26.1 (2007), pp. 42–50.

[84] Shugeyuki Toki, T Fujimaki, and M Okuyama. "Strain-induced crystallization of natural rubber as detected real-time by wide-angle X-ray diffraction technique." In: *Polymer* 41.14 (2000), pp. 5423–5429.

[85] NS Murthy and H Minor. "General procedure for evaluating amorphous scattering and crystallinity from X-ray diffraction scans of semicrystalline polymers." In: *Polymer* 31.6 (1990), pp. 996–1002.

[86] ES Sherman and EL Thomas. "Scanning microdiffraction of polymers." In: *Journal of Materials Science* 14.5 (1979), pp. 1109–1113.

[87] Peisi Keg et al. "Direct Observation of Alkyl Chain Interdigitation in Conjugated Polyquarterthiophene Self-Organized on Graphite Surfaces." In: *Macromolecular Rapid Communications* 29.14 (2008), pp. 1197–1202.

[88] K Siangchaew, D Arayasantiparb, and M Libera. "Measuring polymer microstructure using spatially-Resolved eels in the stem." In: *MRS Online Proceedings Library Archive* 461 (1996).

[89] Maarten JM Wirix et al. "Three-dimensional structure of P3HT assemblies in organic solvents revealed by cryo-TEM." In: *Nano letters* 14.4 (2014), pp. 2033–2038.

[90] Christopher J Takacs et al. "Remarkable order of a high-performance polymer." In: *Nano letters* 13.6 (2013), pp. 2522–2527.

[91] Renaud Payerne et al. "STM studies of poly (3-alkylthiophene) s: model systems for plastic electronics." In: *Synthetic metals* 146.3 (2004), pp. 311–315.

[92] Valerie Randle. "Recent developments in electron backscatter diffraction." In: *Advances in Imaging and Electron Physics* 151 (2008), p. 363.

[93] Suhan Kim et al. "Minimization of focused ion beam damage in nanostructured polymer thin films." In: *Ultramicroscopy* 111.3 (2011), pp. 191–199.

[94] RF Egerton. "Control of radiation damage in the TEM." In: *Ultramicroscopy* 127 (2013), pp. 100–108.

[95] DT Grubb. "Radiation damage and electron microscopy of organic polymers." In: *Journal of Materials Science* 9.10 (1974), pp. 1715–1736.

[96] John S Trent, Jeny I Scheinbeim, and Peter R Couchman. "Ruthenium tetraoxide staining of polymers for electron microscopy." In: *Macromolecules* 16.4 (1983), pp. 589–598.

[97] Christopher J Takacs et al. "Mapping orientational order in a bulk heterojunction solar cell with polarization-dependent photoconductive atomic force microscopy." In: *ACS nano* 8.8 (2014), pp. 8141–8151.

[98] Iain McCulloch et al. "Liquid-crystalline semiconducting polymers with high charge-carrier mobility." In: *Nature materials* 5.4 (2006), p. 328.

[99] Minh Trung Dang, Lionel Hirsch, and Guillaume Wantz. "P3HT: PCBM, best seller in polymer photovoltaic research." In: *Advanced Materials* 23.31 (2011), pp. 3597–3602.

[100] Christian B Nielsen and Iain McCulloch. "Recent advances in transistor performance of polythiophenes." In: *Progress in Polymer Science* 38.12 (2013), pp. 2053–2069.

[101] Martin Brinkmann and J-C Wittmann. "Orientation of Regioregular Poly (3-hexylthiophene) by Directional Solidification: A Simple Method to Reveal the Semicrystalline Structure of a Conjugated Polymer." In: *Advanced Materials* 18.7 (2006), pp. 860–863.

[102] Mahesh P Bhatt, Jacob L Thelen, and Nitash P Balsara. "Effect of Copolymer Composition on Electronic Conductivity of Electrochemically Oxidized Poly (3-hexylthiophene)-b-poly (ethylene oxide) Block Copolymers." In: *Chemistry of Materials* 27.14 (2015), pp. 5141–5148.

[103] David E Motaung, Gerald F Malgas, and Christopher J Arendse. "Comparative study: The effects of solvent on the morphology, optical and structural features of regioregular poly (3-hexylthiophene): fullerene thin films." In: *Synthetic Metals* 160.9-10 (2010), pp. 876–882.

[104] Yu Xie et al. "Solvent effect on the morphology of P3HT/PCBM films." In: *Organic Photovoltaics X*. Vol. 7416. International Society for Optics and Photonics. 2009, 74161Q.

[105] RF Egerton, S Lazar, and M Libera. "Delocalized radiation damage in polymers." In: *Micron* 43.1 (2012), pp. 2–7.

[106] Matthew R Libera and Ray F Egerton. "Advances in the transmission electron microscopy of polymers." In: *Polymer Reviews* 50.3 (2010), pp. 321–339.

[107] K Siangchaew and M Libera. "The influence of fast secondary electrons on the aromatic structure of polystyrene." In: *Philosophical Magazine A* 80.4 (2000), pp. 1001–1016.

[108] Christoph Gammer et al. "Diffraction contrast imaging using virtual apertures." In: *Ultramicroscopy* 155 (2015), pp. 1–10.

[109] Richard Henderson and Robert M Glaeser. "Quantitative analysis of image contrast in electron micrographs of beam-sensitive crystals." In: *Ultramicroscopy* 16.2 (1985), pp. 139–150.

[110] VB Ozdol et al. "Strain mapping at nanometer resolution using advanced nano-beam electron diffraction." In: *Applied Physics Letters* 106.25 (2015), p. 253107.

[111] Edward S Sherman, W Wade Adams, and Edwin L Thomas. "Dark field imaging of semicrystalline polymers by scanning transmission electron microscopy." In: *Journal of Materials Science* 16.1 (1981), pp. 1–9.

[112] Martin Brinkmann and Patrice Rannou. "Effect of molecular weight on the structure and morphology of oriented thin films of regioregular poly (3-hexylthiophene) grown by directional epitaxial solidification." In: *Advanced Functional Materials* 17.1 (2007), pp. 101–108.

[113] Navaphun Kayunkid, Sureeporn Uttiya, and Martin Brinkmann. "Structural model of regioregular poly (3-hexylthiophene) obtained by electron diffraction analysis." In: *Macromolecules* 43.11 (2010), pp. 4961–4967.

[114] S Joshi, S Grigorian, and U Pietsch. "X-ray structural and crystallinity studies of low and high molecular weight poly (3-hexylthiophene)." In: *Physica status solidi (a)* 205.3 (2008), pp. 488–496.

[115] TJ Prosa et al. "X-ray structural studies of poly (3-alkylthiophenes): an example of an inverse comb." In: *Macromolecules* 25.17 (1992), pp. 4364–4372.

[116] Kohji Tashiro et al. "Crystal structural change in poly (3-alkyl thiophene) s induced by iodine doping as studied by an organized combination of X-ray diffraction, infrared/Raman spectroscopy and computer simulation techniques." In: *Polymer* 38.12 (1997), pp. 2867–2879.

[117] R Joseph Kline, Michael D McGehee, and Michael F Toney. "Highly oriented crystals at the buried interface in polythiophene thin-film transistors." In: *Nature Materials* 5.3 (2006), p. 222.

[118] Bingyuan Huang et al. "Effect of thickness-dependent microstructure on the out-of-plane hole mobility in poly (3-hexylthiophene) films." In: *ACS applied materials & interfaces* 4.10 (2012), pp. 5204–5210.

[119] Dirk Willem Van Krevelen and Klaas Te Nijenhuis. *Properties of polymers: their correlation with chemical structure; their numerical estimation and prediction from additive group contributions*. Elsevier, 2009.

[120] Christopher E Wilmer et al. "Large-scale screening of hypothetical metal–organic frameworks." In: *Nature Chemistry* 4.2 (2012), p. 83.

[121] S Fratini et al. "A map of high-mobility molecular semiconductors." In: *Nature materials* 16.10 (2017), p. 998.

[122] Ji-Hoon Kim et al. "Optimization and Analysis of Conjugated Polymer Side Chains for High-Performance Organic Photovoltaic Cells." In: *Advanced Functional Materials* 26.10 (2016), pp. 1517–1525.

[123] Gang Li et al. "High-efficiency solution processable polymer photovoltaic cells by self-organization of polymer blends." In: *Materials For Sustainable Energy: A Collection of Peer-Reviewed Research and Review Articles from Nature Publishing Group*. World Scientific, 2011, pp. 80–84.

[124] Wenchao Zhao et al. "Fullerene-free polymer solar cells with over 11% efficiency and excellent thermal stability." In: *Advanced Materials* 28.23 (2016), pp. 4734–4739.

[125] Edsger CP Smits et al. "Bottom-up organic integrated circuits." In: *Nature* 455.7215 (2008), p. 956.

[126] Dawei Di et al. "Efficient Triplet Exciton Fusion in Molecularly Doped Polymer Light-Emitting Diodes." In: *Advanced Materials* 29.13 (2017).

[127] William R Salaneck, Richard H Friend, and Jean Luc Brédas. "Electronic structure of conjugated polymers: Consequences of electron–lattice coupling." In: *Physics Reports* 319.6 (1999), pp. 231–251.

[128] Elisabetta Collini and Gregory D Scholes. "Coherent intrachain energy migration in a conjugated polymer at room temperature." In: *science* 323.5912 (2009), pp. 369–373.

[129] Vincent Lemaur et al. "Photoinduced charge generation and recombination dynamics in model donor/acceptor pairs for organic solar cell applications: a full quantum-chemical treatment." In: *Journal of the American Chemical Society* 127.16 (2005), pp. 6077–6086.

[130] Lin Zhang et al. "Poly (3-butylthiophene) Inducing Crystallization of Small Molecule Donor for Enhanced Photovoltaic Performance." In: *The Journal of Physical Chemistry C* 119.41 (2015), pp. 23310–23318.

[131] Manuel Guizar-Sicairos, Samuel T Thurman, and James R Fienup. "Efficient subpixel image registration algorithms." In: *Optics letters* 33.2 (2008), pp. 156–158.

[132] Gilles Dennler, Markus C Scharber, and Christoph J Brabec. "Polymer-fullerene bulk-heterojunction solar cells." In: *Advanced materials* 21.13 (2009), pp. 1323–1338.

[133] Maged Abdelsamie et al. "Toward Additive-Free Small-Molecule Organic Solar Cells: Roles of the Donor Crystallization Pathway and Dynamics." In: *Advanced Materials* 27.45 (2015), pp. 7285–7292.

[134] Francesco Arca, Marius Loch, and Paolo Lugli. "Enhancing efficiency of organic bulkheterojunction solar cells by using 1, 8-diiodooctane as processing additive." In: *IEEE Journal of Photovoltaics* 4.6 (2014), pp. 1560–1565.

[135] Markus Reichenberger et al. "Watching Paint Dry: The Impact of Diiodooctane on the Kinetics of Aggregate Formation in Thin Films of Poly (3-hexylthiophene)." In: *Macromolecules* 49.17 (2016), pp. 6420–6430.

[136] Nuradhika Herath et al. "Unraveling the Fundamental Mechanisms of Solvent-Additive-Induced Optimization of Power Conversion Efficiencies in Organic Photovoltaic Devices." In: *ACS applied materials & interfaces* 8.31 (2016), pp. 20220–20229.

[137] Thomas S Van Der Poll et al. "Non-Basic High-Performance Molecules for Solution-Processed Organic Solar Cells." In: *Advanced Materials* 24.27 (2012), pp. 3646–3649.

[138] Steven J Brown et al. "Enhancing Organic Semiconductor–Surface Plasmon Polariton Coupling with Molecular Orientation." In: *Nano letters* 17.10 (2017), pp. 6151–6156.

[139] Ouliana Panova et al. "Orientation mapping of semicrystalline polymers using scanning electron nanobeam diffraction." In: *Micron* 88 (2016), pp. 30–36.

[140] Frederick C Frank. "I. Liquid crystals. On the theory of liquid crystals." In: *Discussions of the Faraday Society* 25 (1958), pp. 19–28.

[141] Robert B Meyer. "On the existence of even indexed disclinations in nematic liquid crystals." In: *Philosophical Magazine* 27.2 (1973), pp. 405–424.

[142] Alfred Saupe. "Disclinations and properties of the directorfield in nematic and cholesteric liquid crystals." In: *Molecular Crystals and Liquid Crystals* 21.3-4 (1973), pp. 211–238.

[143] Wolgang Merzkirch. *Flow visualization*. Elsevier, 2012.

[144] John A Love et al. "Film Morphology of High Efficiency Solution-Processed Small-Molecule Solar Cells." In: *Advanced Functional Materials* 23.40 (2013), pp. 5019–5026.

[145] Tiziano Agostinelli et al. "Real-Time Investigation of Crystallization and Phase-Segregation Dynamics in P3HT: PCBM Solar Cells During Thermal Annealing." In: *Advanced Functional Materials* 21.9 (2011), pp. 1701–1708.

[146] Liu Qian et al. "Effect of Crystallinity of Fullerene Derivatives on Doping Density in the Organic Bulk Heterojunction Layer in Polymer Solar Cells." In: *Chinese Physics Letters* 32.5 (2015), p. 056801.

[147] Xiaoniu Yang et al. "Crystalline Organization of a Methanofullerene as Used for Plastic Solar-Cell Applications." In: *Advanced Materials* 16.9-10 (2004), pp. 802–806.

[148] John E Northrup. "Atomic and electronic structure of polymer organic semiconductors: P3HT, PQT, and PBTTT." In: *Physical Review B* 76.24 (2007), p. 245202.

[149] Fiona C Jamieson et al. "Fullerene crystallisation as a key driver of charge separation in polymer/fullerene bulk heterojunction solar cells." In: *Chemical Science* 3.2 (2012), pp. 485–492.

[150] Tao Liu and Alessandro Troisi. "Understanding the microscopic origin of the very high charge mobility in PBTTT: tolerance of thermal disorder." In: *Advanced Functional Materials* 24.7 (2014), pp. 925–933.

[151] Torben Schuettfort et al. "Microstructure of polycrystalline PBTTT films: domain mapping and structure formation." In: *ACS nano* 6.2 (2012), pp. 1849–1864.

[152] Dominik W Gehrig et al. "The Impact of Donor–Acceptor Phase Separation on the Charge Carrier Dynamics in pBTTT: PCBM Photovoltaic Blends." In: *Macromolecular rapid communications* 36.11 (2015), pp. 1054–1060.

[153] Patrick Gemünden et al. "Effect of mesoscale ordering on the density of states of polymeric semiconductors." In: *Macromolecular rapid communications* 36.11 (2015), pp. 1047–1053.

[154] Karwan Wasman Qadir, Zubair Ahmad, and Khaulah Sulaiman. "Thermal Annealing Effect on the Optical, Electrical and Morphological Properties of the PBTTT-C12: PC71BM Blend Films." In: *Journal of Solar Energy Engineering* 137.3 (2015), p. 034503.

[155] Manish Kumar Singh, Ashish Kumar, and Rajiv Prakash. "Self-assembly of regioregular poly [2, 5-bis (3-tetradecylthiophen-2-yl) thieno [3, 2-b] thiophene], pBTTT-C14 in solvent-mixture and study of its junction behaviour." In: *Organic Electronics* 50 (2017), pp. 138–146.

[156] BA Collins et al. "Polarized X-ray scattering reveals non-crystalline orientational ordering in organic films." In: *Nature materials* 11.6 (2012), p. 536.

[157] Michael L Chabinyc et al. "X-ray scattering study of thin films of poly (2, 5-bis (3-alkylthiophen-2-yl) thieno [3, 2-b] thiophene)." In: *Journal of the American Chemical Society* 129.11 (2007), pp. 3226–3237.

[158] Xinran Zhang et al. "In-Plane Liquid Crystalline Texture of High-Performance Thienothiophene Copolymer Thin Films." In: *Advanced Functional Materials* 20.23 (2010), pp. 4098–4106.

[159] Paul S Drzaic. "Reorientation dynamics of polymer dispersed nematic liquid crystal films." In: *Liquid Crystals* 3.11 (1988), pp. 1543–1559.

[160] Mary O'Neill and Stephen M Kelly. "Ordered materials for organic electronics and photonics." In: *Advanced Materials* 23.5 (2011), pp. 566–584.

[161] RA Street, JE Northrup, and A Salleo. "Transport in polycrystalline polymer thin-film transistors." In: *Physical Review B* 71.16 (2005), p. 165202.

Appendix A

Code

A.1 Virtual Dark Field

The Virtual Dark Field (VDF) is a real space image reconstructed from a given virtual aperture. The signal at each pixel is the integrated sum over all location within the DP where the aperture is non-zero.

```
function [ VDF ] = VDF_iterative( STACK, aperture )
dimension = size(STACK);

VDF = zeros([dimension(3), 1]);

for i = 1:dimension(3)
    i
   slice = single(STACK(:, :, i));
   slice = slice.*aperture;
   k = mean(slice(:));
   VDF(i) = k;
end
end
```

A.2 Realignment of diffraction pattern centers

The beam sways as it scans the sample. The centers of the diffraction patterns therefore need to be realigned to a common center. The inputs are as follows:

- `stack_centers`: If the sways are not too drastic, then a substack can be cut out of the main dataset that only contains the center spots and used to realign the whole stack. This can be done to unburden the use of memory and accelerate the process. If that cannot be done, then this function will work just as well with this variable being the full stack.
- `STACK`: The initial dataset.
- `usfac`: Upsampling factor; integer. Images will be registered to within 1/usfac of a pixel. For example, usfac=20 means the images will be registered within 1/20 of a pixel. Default is 1.

The code uses dftregistraction[131] functions to realign the DPs.

```
function [ Greg_stack ] = dftregistration_alignment( stack_centers, STACK,
    usfac)

mask = stack_centers(:, :, 1);
dimension = size(stack_centers);
dimension2 = size(STACK);
maskfft = fft2(mask*1);

```

```
Greg_stack = zeros(dimension2);

for i = 1:dimension(3)
    slice = stack_centers(:, :, i);
    slicefft = fft2(slice);

    [output] = dftregistration(maskfft, slicefft, usfac);


    diffphase = output(2);
    row_shift = output(3);
    col_shift = output(4);

    slice_to_shift = single(STACK(:,:, i));
    slice_to_shiftfft = fft2(slice_to_shift);

    if (usfac > 0);
        [nr,nc]=size(slice_to_shiftfft);
        Nr = ifftshift([-fix(nr/2):ceil(nr/2)-1]);
        Nc = ifftshift([-fix(nc/2):ceil(nc/2)-1]);
        [Nc,Nr] = meshgrid(Nc,Nr);
        Greg = slice_to_shiftfft.*exp(1i*2*pi*(-row_shift*Nr/nr-col_shift*Nc/
    nc));
        Greg = Greg*exp(1i*diffphase);
    elseif (usfac == 0)
        Greg = slice_to_shiftfft*exp(1i*diffphase);
    end
    Greg_stack(:, :, i) = abs(ifft2(Greg));

end
end
```

A.3 Subtraction of the amorphous background

Because the diffraction spots are quite strong when accumulated over all DPs, if a simple average is used as the template halo to be subtracted certain locations will be inconsistently weighted because those locations have strong diffracted signal. Therefore, the best average to subtract is an artificially generated "halo" based on a Gaussian fit of the average signal. Unfortunately the actual signal halo is not quite Gaussian, and the central spot is so bright that it skews the fit to the halo unless it is very heavily suppressed.

```
[xx, yy] = meshgrid(linspace(1, 512, 512));
cut = 0.006;

Icut912 = mean(shiftedC912r, 3);

%Thresholding the center peak:
Icut912(Icut912>=max(Icut912(:)).*cut) = max(Icut912(:)).*cut;
```

```
[fitresult912, zfit912, fiterr912, zerr912, resnorm912, rr912] = fmgaussfit(xx,yy, Icut912);
```

Iteratively subtracting the halo:

```
function [ STACK, amorphous_map ] = Amorphous_subt_iterative( STACK, center, average, lattice_rad, realDimx, realDimy )
```

The function takes in the following inputs:

- `STACK`: Stack of DPs (initial dataset, preferentially realigned)
- `center`: The center of the diffraction pattern (either extracted previously through a realignment fitting or by eye)
- `average`: the mean of all the DPs (preferentially done after realignment, to make sure the centers all match)
- `lattice_rad`: the characteristic lattice spacing of interest (i.e. how far from the center are we expecting to find the spots), in pixels
- `realDimx and realDimy`: the dimensions of the dataset in real space, i.e. number of probe positions scanned over in x and y

```
%This function takes a slice from a stack identified by its ID number within the stack and subtracts the average amorphous halo from it.

dimension = size(STACK);
```

The bright transmitted beam at the center of each DP is masked with a small aperture, the virtual "beamstop".

```
temp_radius = lattice_rad-20;
sigmaCorr = 3;

%creation of the beamstop signal aperture
[Ya, Xa] = meshgrid(1:dimension(2), 1:dimension(1));
Ra = sqrt ( (center(1) - Xa).^2      +       (center(2) - Ya).^2 )     ;
apertureBeamstop = 60 - Ra;
apertureBeamstop(apertureBeamstop<0) = 0;
apertureBeamstop(apertureBeamstop>0) = 1;
apertureBeamstop = (apertureBeamstop==0)*1;
apertureBeamstop = Gaussian_blurr(apertureBeamstop, 2*ceil(3*sigmaCorr)+1, sigmaCorr);
apertureBeamstop = apertureBeamstop./max(apertureBeamstop(:));
```

Amorphous signal is taken to be the signal close to the center of the DP, where the halo is strong, and excluding the diffraction signal. An "aperture" is made that includes that halo signal; it will be used to reconstruct a virtual dark field and subsequently tailor-fit the amount of halo signal to be subtracted from each DP. The aperture is circular.

```
%creation of the amorphous signal aperture (taken to be close to the beamstop)
[Ya, Xa] = meshgrid(1:dimension(2), 1:dimension(1));
Ra = sqrt ( (center(1) - Xa).^2     +       (center(2) - Ya).^2 )     ;
aperture = temp_radius - Ra;
aperture(aperture<0) = 0;
aperture(aperture>0) = 1;
aperture = (aperture==0)*1;

'Starting Loop'

for i=1:dimension(3)
    i
    STACK(:, :, i) = STACK(:, :, i).*apertureBeamstop;
end

%This is the actual virtual dark field generated from the "amorphous"
%signal located within the aperture created above.
map = VDF_iterative(STACK, aperture);
map = reshape(map, [realDimx, realDimy]);
amorphous_map = map/max(map(:));
```

Each real space pixel of the amorphous VDF is replicated to be the size of the DP it is supposed to be subtracted from. Because of the large size of the datasets involved, the average is subtracted iteratively through a for-loop. This operation could be done all at once through array manipulation, but demands too much memory to do so and is therefore not viable for large files.

Because the intensity of the scattered halo is different for each DP, the subtracted Gaussian halo template is scaled by a number between 0 and 1 representative of the halo's relative intensity. This relative intensity is based off the VDF calculated previously using the generated aperture.

```
map = reshape(map, [1, 1, dimension(3)]);
map = single(map/max(map(:)));

for i=1:dimension(3)
    i
    slice = single(STACK(:, :, i));
    m = squeeze(map(:, :, i));
    slice = slice - average*m*3;
    slice = Gaussian_blurr(slice, 10, 1);
    STACK(:, :, i) = slice;
end

%Setting all values below zero to zero:
STACK(STACK<0) = 0;

end
```

A.4 Line trace plotting

The following code generates plots where a line is plotted for each orientation found at each real space pixel. The slope orientation matches the angle of orientation of the peak found.

```
function [ All_coords, Intensities ] = Line_tracing_cell( peaks, colormap )

dimension = size(peaks);
maxpeak = 15;

%Row coordinates first, columns second; num peaks; real space dims
All_coords = zeros([2, 2, maxpeak, 128, 128]);
Intensities = zeros([maxpeak, 128, 128]);

for a0 = 1:dimension(1)

        [xx, yy] = ind2sub([128, 128], a0);
        peak = peaks{a0, 2};

        if isempty(peak) == 1
%             'There is no diffraction here!'
            continue
        end

        thetas = peak(:, 3);
        intensities = peak(:, 4);

        for peakID = 1:size(peak, 1)

            theta = thetas(peakID);
            intensity = intensities(peakID);

            m = tan(theta);
            b = -yy - m.*xx;
            x = [xx - 0.5, xx+0.5];
            y = m.*x + b;

            if min(y(:)) <= -yy-0.5
                y = [-yy+0.5, -yy-0.5];
                x = (y-b)./m;
            end

            All_coords(1, :, peakID, yy, xx) = x;
            All_coords(2, :, peakID, yy, xx) = y;
            Intensities(peakID, yy, xx) = intensity;

        end

end

```

```
All_coordsx = reshape(All_coords(1, :, :, :, :), [2, 128*128*maxpeak]);
All_coordsy = reshape(All_coords(2, :, :, :, :), [2, 128*128*maxpeak]);
base_alpha = zeros([maxpeak, 128*128*maxpeak]);
base_alpha(4, :) = squeeze(reshape(Intensities, [1, 128*128*maxpeak]));

L = size(colormap, 1);

figure(3546);
clf();
hold on;
for t = 1:128*128*maxpeak
    t
plot(All_coordsx(:, t), All_coordsy(:, t));

end
axis equal off;
hold off;

% print -painters -dpdf -r600 C912Lineplot.pdf

end
```

A.5 Tiling real space with diffraction patterns

```
function [  ] = Swatch_plot( STACK )

swatchdim1 = [92  121];
swatchdim2 = [63  116];

STACK = reshape(STACK, [512  512  128  128]);

swatch = STACK(:, :, swatchdim1(1):swatchdim1(2), swatchdim2(1):swatchdim2(2))
    ;
swatch = squeeze(swatch);

dim = size(swatch)

t = permute(swatch, [1  3  2  4]);

dim = size(t);

t = reshape(t, [512*dim(2)  512*dim(4)]);

t = squeeze(t);
'done'

%cutting up the image into swatches for memory handling purposes:

```

```
%quadrant 1
% tquad = t(  1:32*512  , 1:32*512  );
t(t<20) = 0;
t(t>130) = max(t(:));
% mt = figure(576);
% clf()
% imagesc(tquad)
% axis equal off;
% caxis([0 30]);
% colormap(violetFire(256));

imwrite(t, 'E:\Data\Ouliana\Github\4DSTEM\Colin Analysis\
    C912FullTile_carbonedge', 'tif');

end
```

A.6 Extracting peak orientations from the diffraction patterns

This function takes in an angle step (10 for every 10 degrees, etc) and makes a rainbow map where the real-space image is colored according to the angle of orientation of the crystallites. This is based on the rotating virtual dark field technique. The first peak found is the center of the DP. Inputs are as follows:

- `STACK`: The stack to analyze. Realigned and with the amorphous halo subtracted.
- `nosubSTACK`: The stack to analyze, but WITHOUT the halo subtraction. Because of the way that the code has been written, the central spot has been masked away by the amorphous subtraction, but it is needed in order to locate the center of each DP. Therefore, it is input here.
- `center`: The center of the diffraction patterns.
- `lattice_rad`: The lattice parameter of interest where the spots are expected to be found, in pixels.
- `Test`: If Test=1, diagnostic plots will be shown during the algorithm run.
- `disk_template`: The optional template for a diffraction spot. If none is provided, a synthetic one will be generated.

Credit to Colin Ophus for parts of this code.

```
function [ Peaks_all ] = Rainbow_mapPC_cell( STACK, nosubSTACK, center,
    lattice_rad, Test, disk_template)

tic
```

```
dimension = size(STACK);

if length(dimension)<3
    dimension = [dimension 1];
end

corrThresh = 0.01; %peaks found on the PC image are not registered if they are below this value
sigmaCorr = 2;
mPower = 0.8;
k = fspecial('gaussian',2*ceil(3*sigmaCorr)+1,sigmaCorr);

if nargin > 4
    G2conj = conj(fft2(disk_template));
end

%NOTE: The amorphous background subtraction is set up to be based on
%"amorphous" signal close to the central beam, which means that the
%subtraction may be too harsh at times. Adjustment of the multiplication
%constant of the average to be subtracted may have to be adjusted.
% subSTACK(subSTACK<=0) = 0;
% This is all performed by the Amorphous_subt_iterative.m code


Peaks_all = cell(dimension(3),1);

[column, row] = meshgrid(1:dimension(2), 1:dimension(1));

aesthetic_aperture_rad = 15; % This is the radius of the expected diffraction spot.
masking_aperture_rad = aesthetic_aperture_rad*2; %When looking for peaks on the DP, the peaks found will be masked with an aperture of this radius.

%Creating the aperture mask that masks away the remnants of the central beam
%(may not be subsequently used for large datasets):
Ra = sqrt((center(1) - row).^2 + (center(2)-column).^2);
central_masked = (lattice_rad/1.4) - Ra + 0.5;
aperture = central_masked;
aperture(aperture>0) = 0;
aperture(aperture<0) = 1;
aperture = (aperture~=0)*1;

%Also adding in an aperture for the "outer rims" - reflections at a lattice spacing higher than the innermost spot (which is the one we are after)
aperture(central_masked < -masking_aperture_rad*2) = 0;

aperture = Gaussian_blurr(aperture, 20, 5);
aperture = aperture./max(aperture(:));
'aperture computed'

```

```
%PC aperture: This aperture is for the Phase Correlation plot. We want the
    spot centers to be found only within a small slice within a few pixels of
    the centerline of the aperture "band" where diffraction occurs.
PCcentral_masked = (lattice_rad) - Ra + 0.5;
PCaperture = PCcentral_masked;
PCaperture(PCaperture>6) = 0;
PCaperture(PCaperture<0) = 1;
PCaperture = (PCaperture~=0)*1;

PCaperture(PCcentral_masked < -6) = 0;

PCaperture = Gaussian_blurr(PCaperture, 20, 5);
PCaperture = PCaperture./max(PCaperture(:));
'PCaperture computed'

if Test == 1
    figure(90);
    clf();
    imagesc(PCaperture);
    title('PC aperture');
    axis equal off;
end

'Starting loop'
for ID = 1:dimension(3)

    ID
    I = STACK(:, :, ID);
    nosubI = nosubSTACK(:, :, ID);

    I = single(I);
    nosubI = single(nosubI);

    if Test == 1
        figure(495);
        clf();
        imagesc(I);
        title('The original image');
        axis equal off;
        drawnow();

    end;

    I = aperture.*I;

      if nargin > 5
          nosubm = fft2(nosubI) .* G2conj;
          m = fft2(I) .* G2conj;
          PC = ifft2((abs(m).^mPower) .* exp(1i*angle(m)),'symmetric');
          nosubPC = ifft2((abs(nosubm).^mPower) .* exp(1i*angle(nosubm)),'
```

```
    symmetric');
98          if sigmaCorr > 0
99              PC = conv2(PC,k,'same');
100             nosubPC = conv2(nosubPC,k,'same');
101         end
102
103     else
104         PC = Phase_corellation(I, aesthetic_aperture_rad);
105     end
106
107  if Test == 1
108
109      figure(478);
110      clf();
111      imagesc(PC);
112      title('Phase Correlation')
113      axis equal off;
114      drawnow();
115
116  end
117
118  PCg = PC.*PCaperture;
119  PCg = Gaussian_blurr(PCg, aesthetic_aperture_rad, 1);
120  nosubPCg = Gaussian_blurr(nosubPC, aesthetic_aperture_rad, 1);
121
122  if Test == 1
123      figure(47);
124      clf();
125      imagesc(PCg);
126      title('Phase Correlation')
127      axis equal off;
128      drawnow();
129  end
130
131  %Finding maxima on the correlation plot
132  p =   PCg > circshift(PCg,[-1 -1]) ...
133      & PCg > circshift(PCg,[ 0 -1]) ...
134      & PCg > circshift(PCg,[ 1 -1]) ...
135      & PCg > circshift(PCg,[-1  0]) ...
136      & PCg > circshift(PCg,[ 1  0]) ...
137      & PCg > circshift(PCg,[-1  1]) ...
138      & PCg > circshift(PCg,[ 0  1]) ...
139      & PCg > circshift(PCg,[ 1  1]) ...
140      & PCg > corrThresh;
141
142  nosubp =   nosubPCg > circshift(nosubPCg,[-1 -1]) ...
143      & nosubPCg > circshift(nosubPCg,[ 0 -1]) ...
144      & nosubPCg > circshift(nosubPCg,[ 1 -1]) ...
145      & nosubPCg > circshift(nosubPCg,[-1  0]) ...
146      & nosubPCg > circshift(nosubPCg,[ 1  0]) ...
```

```
147         & nosubPCg > circshift(nosubPCg,[-1  1]) ...
148         & nosubPCg > circshift(nosubPCg,[ 0  1]) ...
149         & nosubPCg > circshift(nosubPCg,[ 1  1]) ...
150         & nosubPCg > corrThresh;
151
152
153     %Locations of the peaks:
154     [xp,yp] = find(p);
155
156     nosubPCgpeeaks = nosubPCg.*nosubp;
157     [nosubxp, nosubyp] = find(nosubPCgpeeaks == max(nosubPCgpeeaks(:)));
158
159     Ip = PC(sub2ind(dimension(1:2),xp,yp));
160     nosubIp = nosubPC(sub2ind(dimension(1:2),nosubxp,nosubyp));
161     xp = vertcat(nosubxp(1), xp);
162     yp = vertcat(nosubyp(1), yp);
163     Ip = vertcat(nosubIp(1), Ip);
164     peakData = sortrows([xp yp Ip ones(numel(xp),1)*ID],-3);
165
166     if size(peakData,1) > 1
167
168         % Delete peaks too close together
169         del = false(size(peakData,1),1);
170         for a1 = 1:size(peakData,1)
171             if del(a1) == false
172                 d2 =  (peakData(:,1)-peakData(a1,1)).^2 ...
173                     + (peakData(:,2)-peakData(a1,2)).^2;
174                 sub = d2 < aesthetic_aperture_rad.^2;
175                 sub(1:a1) = false;
176                 del(sub) = true;
177             end
178         end
179         peakData(del,:) = [];
180     end
181
182     Peaks_all{ID,1} = peakData;
183
184
185     if Test == 1
186     peakData = Peaks_all{ID,1};
187     figure(55)
188     clf();
189     Ip = STACK(:,:,ID);
190     imagesc(Ip.*aperture)
191     % imagesc(Icorr)
192     t = linspace(0,2*pi,180+1);
193     ct = cos(t);
194     st = sin(t);
195     hold on
196     for a0 = 1:size(peakData,1)
```

```
197
198         line(peakData(a0,2)+st*aesthetic_aperture_rad,...
199             peakData(a0,1)+ct*aesthetic_aperture_rad,...
200             'linewidth',1,'color','g')
201     drawnow();
202     end
203     hold off
204     axis equal off
205     set(gca,'position',[0 0 1 1])
206
207     end
208 end
209 toc
210 end
```

A.7 Plotting of the main peak - orientation maps

Credit to Colin Ophus for the great majority of this code.

```
1  function [Irgb,imageOrient,imageOrientInterp,imageMask,mask] = ...
2      measureDisks05(peakDataAll, mycmap)
3
4  % Generate orientation map of primary peak
5
6  sigmaInterp = 1;
7
8  %rRange is the lattice spacing range. The phase correlation is already
       constrained pretty severely in this direction, so this is not a very
       important metric since there is already an aperture earlier in the
       algorithm that constrains it.
9  rRange = [8 278];  % OP
10
11 Nout = [1 1]*128; %Size in real space
12 maskRange = [0 10];
13 maxThetaShift = 10*pi/180; %OP
14
15 thetaPlotSign = -1;
16 thetaPlotRotate = pi*0.35; %OP
17 imageShift = [0 0]; %OP
18
19 N = size(peakDataAll);
20 sig = zeros(N(1),2);
21
22 for a0 = 1:N(1)
23     p = peakDataAll{a0,2};
24     if size(p,1) > 0
25
26         %How many peaks fall within the proper lattice spacing?
27         sub = p(:,5) > rRange(1) & p(:,5) < rRange(2);
```

```
28
29          if sum(sub) == 1
30              % single peak case
31              sig(a0,1) = mod(p(sub,6),pi);
32
33          elseif sum(sub) > 1
34
35              % Multi peak case
36
37              %Only taking the peaks that fall within our lattice spacing
38              %range via boolean slicing:
39              pSub = p(sub,:);
40
41              %Extracting the orientation of only the first, most bright
42              %peak, aka the CENTER:
43              theta0 = pSub(1,6);
44
45
46              thetaAll = pSub(:,6) - theta0;
47              thetaAll = mod(thetaAll + pi/2, pi) - pi/2;
48              % thetaMean = mean(thetaAll) + theta0;
49              % sig(a0,1) = mod(thetaMean,pi);
50
51              subTheta = abs(thetaAll) < maxThetaShift;
52              thetaMean = mean(thetaAll(subTheta)) + theta0;
53
54              sig(a0,1) = mod(thetaMean,pi);
55
56          end
57          sig(a0,2) = sum(p(sub,3));
58
59      end
60  end
61
62  imageOrient = mod( ...
63      thetaPlotSign * reshape(sig(:,1),Nout) ...
64      + thetaPlotRotate, pi);
65  imageMask = reshape(sig(:,2),Nout);
66
67  %Circshifting to account for the two rows at the top that the camera
68  %capture for some reason puts at the top:
69  imageOrient = circshift(imageOrient,imageShift);
70  imageMask = circshift(imageMask,imageShift);
71
72  % Apply trigonometric interpolation:
73  ct = cos(2*imageOrient);
74  st = sin(2*imageOrient);
75
76  k = fspecial('gaussian',...
77      max(2*ceil(3*sigmaInterp)+1,11),...
```

```
78      sigmaInterp);
79  ct = conv2(ct .* imageMask,k,'same');
80  st = conv2(st .* imageMask,k,'same');
81
82
83  ct = ct ./ imageMask;
84  st = st ./ imageMask;
85  imageOrientInterp = mod(0.5*atan2(st,ct),pi);
86
87
88  % Mask
89  imageMaskInterp = conv2(imageMask,k,'same');
90
91  mask = (imageMaskInterp - maskRange(1)) ...
92      / (maskRange(2) - maskRange(1));
93
94  mask = min(max(mask,0),1);
95
96  mask = sin(mask*pi/2).^2;
97
98  if nargin > 1
99      Irgb_simple = imageOrientInterp;
100     rad2deg(Irgb_simple);
101     figure(468)
102     clf();
103     imagesc(Irgb_simple);
104     colormap(mycmap);
105     axis equal off;
106     colorbar
107 end
108
109 cmap = jetLoop;
110 Irgb = ind2rgb(round(255* ...
111     mod((imageOrientInterp + 0) / pi,1))+1,cmap);
112 Irgb = rgb2hsv(Irgb);
113 Irgb(:,:,3) = Irgb(:,:,3) .* mask;
114 Irgb = hsv2rgb(Irgb);
115
116 figure(311)
117 clf
118 imagesc(Irgb)
119 colorbar();
120 axis off equal
121
122 figure(32)
123 clf
124 imagesc(mask)
125 colormap(gray(256))
126 axis off equal
127 colorbar
```

```
128
129 figure(49652)
130 clf()
131 imagesc(imageOrient)
132 axis equal off;
133 colormap(violetFire(256));
134
135 end
```

A.8 Reformatting peak data, converting to polar coordinates

Credit to Colin Ophus for the great majority of this code.

```
1  function [peakDataAll] = measureDisks02(peakDataAll)
2  % add second column to peakDataAll: polar coordinates,
3  % add third column to peakDataAll:  bright field and dark field images
4
5  N = size(peakDataAll);
6
7  for a0 = 1:N(1)
8
9      p = peakDataAll{a0,1};
10
11     if size(p,1) < 1
12         a0
13         disp('empty!')
14         peakDataAll{a0,2} = peakDataAll{a0-1,2};
15         continue
16     end
17
18     if size(p,1) > 1
19         %subtracting the center coordinate:
20         x = p(2:end,1) - p(1,1);
21         y = p(2:end,2) - p(1,2);
22         int = p(2:end,3);
23         ind = p(2:end,4);
24         %r is the distance from the center of the spot:
25         r = sqrt(x.^2 + y.^2);
26         %t is the angle in RADIANS
27         t = atan2(y,x);
28
29         peakDataAll{a0,2} = [x y int ind r t];
30         dfSum = sum(int);
31     else
32         dfSum = 0;
33     end
34
```

```
35      bf = p(1,3);
36      peakDataAll{a0,3} = [bf dfSum];
37
38  end
39  end
```

A.9 Tracing the line flows of the lattice

The following functions generate the line flow maps that pick positions in real space and follow their diffraction peak orientation throughout the image. The line is propagated throughout the image as long as there is a neighboring peak found within a certain number of degrees.

Credit to Colin Ophus for the great majority of this code.

```
1
2  function [cubeOrient,thetaBins,cubeOrientInit] = ...
3      traceFlow11(peakDataAll,mask)
4
5  % Full 3D tracing of the orientation maps
6
7  flag_transpose = 0;
8  shiftImage = [0 -2]; %for the two rows on the bottom that for some reason
       always end up wrapped to the top
9  shiftImage = [0 0]; %For PBTTT, this is already done beforehand
10
11 N = [1 1]*128; %Size of the real space image
12 sigma = 2/2;
13
14 %Blending factors of the cube orient kernel:
15 sigmaTheta = 2 * pi / 180; %in radians (rad = deg*pi/180)
16 sigmaTheta = 10 * pi / 180;
17 thetaRotateplanes = -9*pi/180 + pi/2;  % extra pi/2 to convert peak
       orientations to lattice planes. This 9 degrees rotation factor is inherent
       to the microscope (TITAN X).
18
19
20 %C912 lattice parameter range:
21 rRange = [109 129]; %Range of lattice spacing where peaks are to be found (in
       pixels) = radius of the diffraction
22 %Nout = round([128*1.94 128]);  %If there was drift realignment, readjust this
       final dimension
23
24 Nout = [128 128]; %PBTTT11 %OP
25
26 %Coarseness of the angle range:
27 dTheta = 1*pi/180;
28 thetaBins = 0:dTheta:(2*pi-dTheta/2);
29 Ntheta = length(thetaBins);
30
```

```
% Main loop
cubeOrientInit = zeros(N(1),N(2),Ntheta);
comp = 0;
for a0 = 1:size(peakDataAll,1)
    [xInd,yInd] = ind2sub(N,a0);

    p = peakDataAll{a0,2};


    if ~isempty(p)
        sub = (p(:,5) > rRange(1)) ...
            & (p(:,5) < rRange(2));


        theta = p(sub,6) + thetaRotateplanes;
        int = p(sub,3);

        thetaInds = mod(round(theta / dTheta),Ntheta) + 1;
        cubeOrientInit(xInd,yInd,thetaInds) = int;

        thetaInds = mod(round((theta + pi) / dTheta),Ntheta) + 1;
        cubeOrientInit(xInd,yInd,thetaInds) = int;

    end

    if mod(a0,100) == 0
        comp = a0 / size(peakDataAll,1);
        progressbar(comp,2);
    end
end
if comp < 1
    progressbar(1,2);
end


figure(45);
clf()
imagesc(sum(cubeOrientInit, 3));
axis equal off;


% Apply image transformation
for a0 = 1:Ntheta
    if flag_transpose == 1
        cubeOrientInit(:,:,a0) = cubeOrientInit(:,:,a0)';
    end
    cubeOrientInit(:,:,a0) = circshift(cubeOrientInit(:,:,a0),shiftImage);
end

% apply mask
```

```
k = fspecial('gaussian',max(7,2*ceil(3*sigma)+1),sigma);
mask = double(mask);

% figure(4555);
% clf();
% imagesc(sum(cubeOrientInit, 3));
% axis equal off;

%=========================
%%Smoothing over x and y, "blending" the thetas into each other; if you don't want to do that it's quite fine too:
% for a0 = 1:Ntheta
%     cubeOrientInit(:,:,a0) = ...
%         conv2(cubeOrientInit(:,:,a0) .* mask,k,'same') ...
%         ./ conv2(mask,k,'same');
% end
%=========================


% Smoothing over theta
s = sigmaTheta / dTheta;
r = max(3,ceil(3*s));
k = fspecial('gaussian',2*r+1,s);
k = k(:,r+1);
k = k / sum(k(:));
for a0 = 1:N(1)
    for a1 = 1:N(2)
        sig = cubeOrientInit(a0,a1,:);
        sig = convolve2(sig(:),k,'wrap');
        cubeOrientInit(a0,a1,:) = sig;
    end
end

% Output after correcting drift
cubeOrient = zeros(Nout(1),Nout(2),Ntheta);

for a0 = 1:Ntheta
    cubeOrient(:,:,a0) = imresize(...
        cubeOrientInit(:,:,a0),...
        Nout,'bilinear');
end

figure(9898)
clf();
plot(squeeze(cubeOrient(94, 94, :)));
end
```

```

function [flowLines3D] = traceFlow12(cubeOrient,thetaBins, carbonmask)

```

```
4
5 %For TC22/TC4
6
7 % minWeightInit = 0.1; %CO
8 minWeightInit = 1e-4 * 0; %OP
9
10 stepsMax = 4e3;%2e3;
11 % stepSize = 0.25*1;
12 stepSize = 0.5*1;
13
14
15 maxAngleChange = pi/2;%15*pi/180;
16
17 %For PBTTT11
18 % minWeightInit = 0.1; %CO
19 minWeightInit = 1e-4 * 0; %OP
20
21
22 minWeightInit = 1e-4; %OP C912
23
24 stepsMax = 4e3;%2e3;
25 % stepSize = 0.25*1;
26 stepSize = 0.5;
27 stepSize = 0.1;
28
29 maxAngleChange = pi;%15*pi/180;
30 maxAngleChange = 5*pi/180; %C912;
31 maxAngleChange = 15*pi/180; %C912;
32
33 sigmaWeight = 1;
34 sigmaTheta = 1*2.5;  % In bins
35 sigmaThetaInit = 2;  % In bins
36
37 %==========================
38
39 N = size(cubeOrient);
40 % thetaRotateplanes = -9*pi/180;
41 flag_plot_result = 1 * 1;
42 flag_use_orientation_image = 0;
43
44 skip = 4*1;%5*2;
45 % skip = 1; %OP
46 xx = floor(skip/2):skip:N(1);
47 yy = floor(skip/2):skip:N(2);
48 [yya,xxa] = meshgrid(yy,xx);
49 xySeeds = [xxa(:) yya(:)];
50
51 % xySeeds = [58 75];
52 % xySeeds = [101 79];
53 % xySeeds = [79 101] + [2 0];
```

```
54
55 % Move theta by offset - doesn't work
56 % thetaBins = thetaBins + thetaRotateplanes;
57
58 % Coordinates
59 x0 = 1:N(1);
60 y0 = 1:N(2);
61 % [ya,xa] = meshgrid(y0,x0);
62
63 % Weighting kernel
64 v = -ceil(2*sigmaWeight):ceil(2*sigmaWeight);
65 % v = -2:2;
66 vt = -ceil(2*sigmaTheta):ceil(2*sigmaTheta);
67 [yy,xx,zz] = meshgrid(v,v,vt);
68 k =    exp(-xx.^2 / (2*sigmaWeight^2)) ...
69     .* exp(-yy.^2 / (2*sigmaWeight^2)) ...
70     .* exp(-zz.^2 / (2*sigmaTheta^2));
71 k = k / sum(k(:));
72 % term1 = -1/(2*sigmaWeight^2);
73
74 r = ceil(3*sigmaThetaInit);
75 kInit = fspecial('gaussian',...
76     2*r+1,sigmaThetaInit);
77 kInit = kInit(:,r+1);
78 kInit = kInit / sum(kInit);
79 %
80 % figure(234)
81 % clf;
82 % imagesc(kInit)
83 % axis equal
84
85 % Bookkeeping
86 numSeeds = size(xySeeds,1);
87 flowLines3D = cell(1,1);
88 flowCount = 1;
89 deltaTheta = thetaBins(2) - thetaBins(1);
90 Ntheta = length(thetaBins);
91 % shiftThetaBins = thetaBins(:) * 1e-6;
92 thetaTile = repmat(reshape(thetaBins,...
93     [1 1 N(3)]),[length(v) length(v)]);
94
95 % Generate flow lines
96 for a0 = 1:numSeeds
97 % for a0 = 1:150
98     a0
99     xyInit = xySeeds(a0,:);
100
101    if carbonmask(round(xyInit(1)),round(xyInit(2))) == 1
102        continue
103    end
```

```
104
105     % Get initial theta seeds
106     %thetaSig is just the line of angles from the cube, with a peak at
107     %angle locations where the orientation has been found.
108     thetaSig = squeeze( ...
109         cubeOrient(round(xyInit(1)),round(xyInit(2)),:));
110
111     rad2deg(thetaSig);
112
113     %Convolving with a smoothing kernel (WARNING: kInit has nothing to do with
        k):
114     thetaSig = convolve2(thetaSig,kInit,'wrap');
115
116     %p is equal to 1 where there is a peak and 0 everywhere else. Basically
117     %a peak finding filter.
118     %The size of p is [360 1] (or other, depending on the coarseness of the
        thetabins.
119     p =   thetaSig > circshift(thetaSig,[-1 0]) ...
120         & thetaSig > circshift(thetaSig,[ 1 0]);
121
122     %Since we do not want to find both of the opposing peaks that are
123     %really one reflection (reflected spot across the center beam), we
124     %earse one half of the field of view. We only look at peaks in the 0 to
125     %180 degree range (because both peaks are equally strong and inevitably
126     %found by the algorithm, we do not miss any, really).
127     p((Ntheta/2+1):end) = false;
128
129     %thetaInit are the angle(s) at which there are peaks.
130     thetaInit = thetaBins(p);
131
132     % Refine initial angles, get initial intensties
133     del = false(length(thetaInit),1);
134
135     %xInds and yInds are coordinates some x and y away from the seed
136     %location under consideration. looks like [... x-2 x-1 x x+1 x+2 ...]
137     xInds = round(xyInit(1)) + v;
138     yInds = round(xyInit(2)) + v;
139
140     %Just in case we are at an edge where the coordinates go out of bounds,
141     %we delete any coordinates from xInds and yInds that are smaller than 1
142     %or larger than the total dimention of the real space image.
143     xKeep = xInds >= 1 & xInds <= N(1);
144     yKeep = yInds >= 1 & yInds <= N(2);
145
146     %At the onset, simply a vector array with the same number of zeros as
        there
147     %are peaks.
148     intInit = zeros(length(thetaInit),1);
149
150     %Stepping over each angle peak:
```

```
151     for a1 = 1:length(thetaInit)
152         for a2 = 1:5
153 
154             %vt is the same as v, but for thetas. Looks like
155             %[... -5 -4 -3 -2 -1 0 1 2 3 4 5 ...]
156 
157             %In the case that the step size between the thetabins is not 1
158             %degree
159             %(which makes everything easier - but maybe it's 0.5 degrees or
160             %another arbitrary amount), the thetaInit will not *really* be
161             %in units of theta but in units of 2theta or 3theta or whatever
162             %the step size multiplier is. In order to get the actual value
163             %of the peak in the proper [0 180] degree scale, we need to
164             %divide the peak location within thetaBins by the theta step.
165             %This is what is happening here.
166 
167             %reminder: mod is the REMAINDER after division.
168             tInds = mod(round(thetaInit(a1) / deltaTheta) + vt, Ntheta) + 1;
169 
170             %k is our 3Dkernel: v by v by vt; basically x.y.theta.
171             %The slicing with xKeep and yKeep is so that we are not falling
172             %off the edges.
173             signal3D = k(xKeep,yKeep,:) ...
174                 .* cubeOrient( ...
175                 xInds(xKeep),yInds(yKeep),tInds);
176 
177 
178             intInit(a1) = sum(signal3D(:));
179             if intInit(a1) > minWeightInit
180                 theta3D = thetaTile(xKeep,yKeep,tInds);
181 
182                 thetaInit(a1) = sum(signal3D(:).*theta3D(:)) ...
183                     / sum(signal3D(:));
184             else
185                 del(a1) = true;
186             end
187 
188         end
189     end
190     thetaInit(del) = [];
191     intInit(del) = [];
192 
193     for a1 = 1:length(thetaInit)
194         theta = thetaInit(a1);
195         xyI = [xyInit intInit(a1)];
196         xyAll1 = xyI;
197         count = 1;
198         while count <= stepsMax
199 
200             % Update position
```

```
201             xyI(1:2) = xyI(1:2) + [cos(theta) sin(theta)] * stepSize;
202
203             % Update orientation
204             xInds = round(xyI(1)) + v;
205             yInds = round(xyI(2)) + v;
206             tInds = mod(round(theta / deltaTheta) + vt,Ntheta) + 1;
207             xKeep = xInds >= 1 & xInds <= N(1);
208             yKeep = yInds >= 1 & yInds <= N(2);
209
210             signal3D = k(xKeep,yKeep,:) ...
211                 .* cubeOrient( ...
212                 xInds(xKeep),yInds(yKeep),tInds);
213             theta3D = thetaTile(xKeep,yKeep,tInds);
214             thetaNew = sum(signal3D(:).*theta3D(:)) ...
215                 / sum(signal3D(:));
216             xyI(3) = sum(signal3D(:));
217
218             % Verify angle change is small enough, and intensity is high
    enough
219             if (abs(mod(thetaNew - theta + pi,2*pi) - pi) ...
220                     < maxAngleChange)
221
222                 theta = thetaNew;
223                 % Verify point still inside boundaries
224                 if xyI(1) < 1 ...
225                         || xyI(2) < 1 ...
226                         || xyI(1) > N(1) ...
227                         || xyI(2) > N(2)
228                     count = stepsMax + 1;
229                 else
230
231                     % Iterate
232                     count = count + 1;
233                     xyAll1(count,:) = xyI;
234
235                 end
236             else
237                 count = stepsMax + 1;
238             end
239         end
240
241         % Move in the opposite direction
242         theta = thetaInit(a1) + pi;
243         xyI = [xyInit  intInit(a1)];
244         xyAll2 = xyI;
245         count = 1;
246         while count <= stepsMax
247
248             % Update position
249             xyI(1:2) = xyI(1:2) + [cos(theta) sin(theta)] * stepSize;
```

```
250
251             % Update orientation
252             xInds = round(xyI(1)) + v;
253             yInds = round(xyI(2)) + v;
254             tInds = mod(round(theta / deltaTheta) + vt,Ntheta) + 1;
255             xKeep = xInds >= 1 & xInds <= N(1);
256             yKeep = yInds >= 1 & yInds <= N(2);
257
258             signal3D = k(xKeep,yKeep,:) ...
259                 .* cubeOrient( ...
260                 xInds(xKeep),yInds(yKeep),tInds);
261             theta3D = thetaTile(xKeep,yKeep,tInds);
262             thetaNew = sum(signal3D(:).*theta3D(:)) ...
263                 / sum(signal3D(:));
264             xyI(3) = sum(signal3D(:));
265             % Verify angle change is small enough
266             if (abs(mod(thetaNew - theta + pi,2*pi) - pi) ...
267                     < maxAngleChange)
268
269                 theta = thetaNew;
270
271                 % Verify point still inside boundaries
272                 if xyI(1) < 1 ...
273                         || xyI(2) < 1 ...
274                         || xyI(1) > N(1) ...
275                         || xyI(2) > N(2)
276                     count = stepsMax + 1;
277                 else
278                     % Iterate
279                     count = count + 1;
280                     xyAll2(count,:) = xyI;
281                 end
282             else
283                 count = stepsMax + 1;
284             end
285         end
286
287         % Output trace
288         xyUnion = [flipud(xyAll1(2:end,:)); xyAll2];
289         if size(xyUnion,1) > 1
290             flowLines3D{flowCount,1} = xyUnion;
291             flowCount = flowCount + 1;
292         end
293     end
294
295
296     comp = a0 / numSeeds;
297     progressbar(comp,2);
298 end
299
```

```
if flag_plot_result == true
    figure(56)
    clf

%This is just plotting the figure:

        if flag_use_orientation_image == true
            [~,tInds] = max(cubeOrient(:,:,1:(N(3)/2)),[],3);
            imageOrient = thetaBins(tInds);
            imagesc(imageOrient/pi,...
                'xdata',y0,'ydata',x0)

        else

            I = sum(cubeOrient,3);
            k = fspecial('gaussian',7,1);
            I = conv2(I,k,'same') ...
                ./  conv2(ones(size(I)),k,'same');
            imagesc(I / max(I(:)),...
            'xdata',y0,'ydata',x0)
        end

    hold on
    size(flowLines3D)
    for a0 = 1:size(flowLines3D,1)

        xyAll = flowLines3D{a0,1};
        plot(xyAll(:,2),xyAll(:,1),...
            'linewidth',1,'color','k')
    end
    hold off
    axis equal off
    if flag_use_orientation_image == true
        colormap(jetLoop(256) *1 + 0);
        caxis([0 1])
    else
        colormap(gray(256))
        caxis([-1 1])
    end
    set(gca,'position',[0 0 1 1])
end
end
```

```
function [Irgb] = traceFlow16(flowLines)
tic

N = [128 128]; %size of output array


% Dataset PBTTT11
```

```
dxyOut = 0.01; %this is the important parameter that determines the thickness
    and sparcity of the lines. In general, smaller = lots of thin lines,
    bigger = a few thick lines
Nout = round(N(1:2) / dxyOut);
scaleLines = 2;
sigmaImage = 1;
scaleImageColour = 0.00000000020;
intAvgMin = 0.000025;
intRange = [0.0  2];
windowSmooth = 11;

inds = 1:size(flowLines,1);

% initialize arrays
Idx = zeros(Nout);
Idy = zeros(Nout);
Icount = zeros(Nout);


% Main loop
comp = 0;
for a0 = 1:1:size(flowLines,1)
    ind = inds(a0);
    xyI = flowLines{ind,1};
    if mean(xyI(:,3)) > intAvgMin

        % Intensity
        xyI(:,3) = smooth(xyI(:,3),windowSmooth,'moving');
        xyI(:,3) = (xyI(:,3) - intRange(1)) / (intRange(2) - intRange(1));
        xyI(:,3) = min(max(xyI(:,3),0),1);
        if scaleLines > 1
            xyI = imresize(xyI,...
                [round(scaleLines*size(xyI,1)) 3],...
                'bilinear');
            xyI(:,3) = xyI(:,3) / scaleLines;
        end

        % direction
        dxy = circshift(xyI(:,1:2),[-1 0]) ...
            - circshift(xyI(:,1:2),[1 0]);
        dxy(1,:) = dxy(2,:);
        dxy(end,:) = dxy(end-1,:);


        % coordinates
        x = xyI(:,1) / dxyOut;
        y = xyI(:,2) / dxyOut;
        x = min(max(x,1),Nout(1)-1);
        y = min(max(y,1),Nout(2)-1);
        xF = floor(x);
```

```
56          yF = floor(y);
57          dx = x - xF;
58          dy = y - yF;
59
60          xyInds = [ ...
61              xF yF;
62              xF+1 yF;
63              xF yF+1;
64              xF+1 yF+1;
65              ];
66          weights = [ ...
67              (1-dx).*(1-dy);
68              dx.*(1-dy);
69              (1-dx).*dy;
70              dx.*dy;
71              ];
72
73
74          Idx = Idx + accumarray(xyInds,...
75              weights.*repmat(dxy(:,1).*xyI(:,3),[4 1]),Nout);
76          Idy = Idy + accumarray(xyInds,...
77              weights.*repmat(dxy(:,2).*xyI(:,3),[4 1]),Nout);
78          Icount = Icount + accumarray(xyInds,...
79              weights.*repmat(xyI(:,3),[4 1]),Nout);
80
81      end
82
83      comp = a0 / size(flowLines,1);
84      progressbar(comp,2);
85  end
86  if comp < 1
87      progressbar(1,2);
88  end
89
90  % KDE
91  k = fspecial('gaussian',2*ceil(4*sigmaImage)+1,sigmaImage);
92  Inorm = 1./ conv2(ones(Nout),k,'same');
93  Idx = conv2(Idx,k,'same') .* Inorm;
94  Idy = conv2(Idy,k,'same') .* Inorm;
95  Icount = conv2(Icount,k,'same') .* Inorm;
96
97
98  % Make RGB image
99  Irgb = ones(Nout(1),Nout(2),3);
100 Ih = mod(atan2(Idy,Idx)/pi,1);
101 Iv = min(Icount / scaleImageColour,1);
102 Irgb(:,:,1) = Ih;
103 Irgb(:,:,3) = Iv;
104 Irgb = hsv2rgb(Irgb);
105
```

```
106 figure(112)
107 clf
108 imagesc(Irgb)
109 axis equal off
110 colormap(gray(256))
111 set(gca,'position',[0 0 1 1])
112 toc
113 end
```